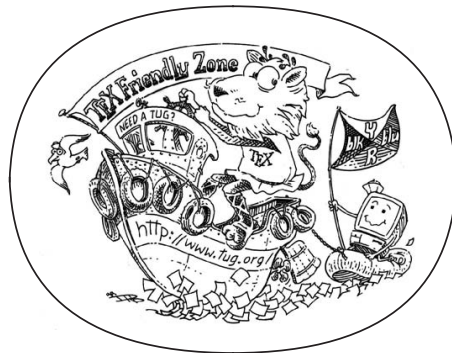


SPATIAL PATTERNS OF DROPLETS IN TURBULENT CLOUDS

KATARZYNA KARPIŃSKA



Ph.D. thesis

Atmospheric Physics Department
Faculty of Physics
University of Warsaw

2018 – version 1.0

Katarzyna Karpińska: *Spatial patterns of droplets in turbulent clouds*, Ph.D. thesis, © 2018

SUPERVISOR:

prof. dr hab. Szymon Malinowski

LOCATION:

Warszawa

Ohana means family.
Family means nobody gets left behind, or forgotten.
— Lilo & Stitch

Dedicated to the loving memory of Rudolf Miede.

1939 – 2005

ABSTRACT

Short summary of the contents... a great guide by Kent Beck how to write good abstracts can be found here:

<https://plg.uwaterloo.ca/~migod/research/beck00PSLA.html>

PUBLICATIONS

Some ideas and figures have appeared previously in the following publications:

Put your publications from the thesis here. The packages `multibib` or `bibtopic` etc. can be used to handle multiple different bibliographies in your document.

*Curiosity killed the cat,
but satisfaction brought it back.*

— English proverb

ACKNOWLEDGEMENTS

Put your acknowledgements here.

Podziekowania itp.

Inne:

CONTENTS

0.1 Organization of the thesis	1
I INTRODUCTION	
1 INTRODUCTION	5
1.1 Research problem exploration - literature review	5
1.1.1 Turbulence	5
1.1.2 Single particle motion in the flow	15
1.1.3 Particle motion in turbulent environment	18
1.1.4 Vortex structures versus cloud droplet clustering	21
1.2 Research problem statement	23
2 METHODS	25
2.1 Vortex model	25
2.2 Dynamical systems formalism	28
2.3 Numerical simulations	32
2.3.1 Single particle trajectory	32
2.3.2 Multiple particles in vortex domain	33
2.4 Cloud voids observation	35
2.4.1 Atmospheric turbulence measurements	36
2.4.2 Lasersheet photography technique	36
2.4.3 Experimental particle imaging vs. numerical simulations	38
2.5 Cloud-like conditions	39
II RESULTS	
3 CHARACTERISTICS OF SINGLE PARTICLE MOTION IN A BURGERS VORTEX	43
3.1 Motion along the vortex axis	45
3.2 Motion in the plane perpendicular to vortex axis	49
3.2.1 Without gravity (vertical vortex)	51
3.2.2 With gravity (inclined vortex)	62
3.3 Time scales of single particle motion	72
3.4 Summary	73
4 CLOUD VOIDS - INTERPRETATION AND EXPLANATION	75
4.1 Cloud voids experiment results	75
4.2 Cloud void creation conditions	78
4.2.1 Polydisperse droplet trajectories	79
4.2.2 Void size estimation	83
4.2.3 Timescales of motion	83
4.3 Summary	85
5 CLOUD VOIDS SIMULATIONS	87
5.1 Numerical simulation results	87
5.2 Mie scattering influence	87

5.3 Preferential concentration statistics	87
6 SUMMARY AND DISCUSSION	89
BIBLIOGRAPHY	91

LIST OF FIGURES

Figure 1	Turbulent eddy size ranges and transfer of energy diagram (from Saeedipour et al. [104]).	8
Figure 2	Power spectral density (PSD) and 2nd order structure functions (D_2) of velocity fluctuations of the three components u , v , w (blue, green, red) composites for all ascents/descents in single measurement flight (TO10) of POST campaign. Individual plots are shifted with respect to each other by factors of 10 for comparison, as indicated. Dashed lines show $-5/3$ slope for PSD or $2/3$ slope for D_2 fitted in a range of frequencies from 0.3 Hz to 5 Hz, in order to avoid instrumental artifacts at higher frequencies. Each column heading corresponds to Sc cloud top sublayer of different properties: FT- free troposphere, TISL - turbulent inversion sublayer, CTMSL - cloud top mixing sublayer, CTL - cloud top layer.	10
Figure 3	Perspective views of 3D contour surfaces of dissipation (red) and enstrophy (cyan) based on: (A-C) three instantaneous snapshots from the $8,192^3$ simulation at $R_\lambda \approx 1,300$, contrasted with data from (D) $2,048^3$ simulation at $R_\lambda \approx 400$. The contour thresholds used were 300 for data at $R_\lambda \approx 1,300$ and 70 for data at $R_\lambda \approx 400$. The subcubes are 51^3 in extent in A-C and 31^3 in D. Reprinted from Yeung P K, Zhai X M, and Sreenivasan Katepalli R [136].	12
Figure 4	Dissipation rate of the kinetic energy estimated from the structure function method ϵ_{SF} , zero crossings of successively filtered signals ϵ_{NCF} and zero crossings of signals with recovered part of the spectrum ϵ_{NCR} as a function of ϵ_{PSD} (from the power spectra method). Each point represents an estimate from a single horizontal segment of flight in the atmospheric boundary layer. (a) POST flight TO10 (b) POST flight TO 13. Reprinted from Wacławczyk et al. [125]. Description of estimation methods available in the source paper.	14

Figure 5	Straining of vorticity in Burgers vortex. δ is vortex core size (from Davidson [39]).	26
Figure 6	Burgers vortex dimensionless velocity components in cylindrical coordinates. u_φ does not depend on any parameter. The rest is plotted for an arbitrarily chosen strain parameter $A = 0.001$. r_s is defined in the text.	27
Figure 7	Trajectories in linearized neighborhoods of several 2-dimensional equilibria: (a) saddle (hyperbolic), (b) stable node (attracting), (c) center (elliptic), (d) stable spiral (from Cvitanović et al. [37]).	30
Figure 8	Trajectories in linearized neighborhoods of 3-dimensional equilibria: (a) saddle, (b) saddle-focus.	31
Figure 9	Hopf bifurcation depicted in a plane. α is bifurcation parameter, its critical value is $\alpha_{cr} = 0$. The figure comes from [66].	31
Figure 10	A scheme of numerical simulation's vortex model domain. D is cylinder radius, Z is its half-length, δ is vortex core size, θ is gravity alignment angle, \vec{g} is gravity direction.	34
Figure 11	Upper part of the figure presents an image of UFS observatory on the slope of Zugspitze. Lower part shows the arrangement of instruments at the UFS roof.	35
Figure 12	Relative intensity of scattered light (on radial axis, in logarithmic scale) on scattering angle and sphere radius according to Mie scattering theory.	37
Figure 13	Image of mountain-top cloud particles, illuminated by a laser sheet light (Nd:YAG laser, 532 nm, 45 W), taken at 8:24 AM on 27th of August 2011 by Markus Neumann. Exposure time: 1/3200 s, focal length: 200 mm, f/2.8.	38
Figure 14	Stokes number St and settling parameter S_v space. Each point is based on a 1 s average of cloud data. The CARRIBA data represent typical conditions for clean (red) and slightly more polluted (yellow) cases and provide a reference for typical trade wind cumuli (see [115] for more details). Reprinted from [113].	40
Figure 15	Equilibrium position z_b versus vortex core size δ and particle radius R for $\theta = \pi/2$. Plot variables' ranges correspond to cloud-like conditions.	46

Figure 16	Characteristic time of the motion along vortex axis τ_z (green line, right y-axis) versus vortex core size δ and its relative error (left y-axis, bar chart) versus δ and particle radius R . Colorscale indicates dependence on R . Plot variables' ranges correspond to cloud-like conditions.	48
Figure 17	Logarithmic factor $\log L$ (in τ_{ex}) vs. z_0^* - ratio of initial position and equilibrium position. Line color is scaled by Z^* values which refer to different ratios of vortex half-length and equilibrium position.	50
Figure 18	Particle stable periodic orbit radius r_{orb}^+ square (left y-axis) and orbit nondimensional angular momentum (right y-axis) with respect to parameter $\sqrt{St/A}$. Dashed lines represent asymptotic relations.	52
Figure 19	Particle stable orbit radius r_{orb} dependence on particle radius R and vortex strain parameter A for cloud-like parameter ranges and vortex core size $\delta = 0.5$ cm. Black line represents critical parameter value as for stable orbit existence. 54	
Figure 20	Particle stable orbit angular velocity ω_{orb} dependence on particle radius R and vortex core radius δ for cloud-like parameter ranges. Parameter domain above the line corresponding to an arbitrary A value is the domain in which stable periodic orbit exists.	55
Figure 21	Tracking of a particle while docking on axis, for $\sigma = 10^{-4}$. Line color corresponds to St/A value, line color intensity to different St and A representations. Upper panel- radial coordinate, middle panel - radial velocity, lower panel - angular velocity. Plots are magnified for better visibility.	56
Figure 22	Tracking of a particle while docking in orbit, for $\sigma = 10^{-4}$. Line color corresponds to St/A value, line color intensity to different St and A representations. Upper panel- radial coordinate, middle panel - radial velocity, lower panel - angular velocity.	57

Figure 23	Same as in Fig. 21, but X-axis is scaled separately for each trajectory by a docking time. On Y-axes, the radial velocity is scaled by the fluid velocity at the starting point $u_r(r_s)$, angular velocity is scaled by the fluid angular velocity at the final position σ , so $u_\varphi(\sigma)/\sigma$	58
Figure 24	Same as in Fig. 22, but X-axis is scaled separately for each trajectory by docking time. On Y-axes, radial position is scaled by circular orbit radius, radial velocity is scaled by the opposite of fluid velocity at the starting point $-u_r(\sigma)$, angular velocity is scaled by the particle angular velocity at the circular orbit ω_{orb}^+	59
Figure 25	Angular velocity of a particle while docking at the axis (top) and in-orbit (bottom). X-axis is scaled separately for each trajectory by a docking time. On Y-axis, angular velocity is scaled by the fluid angular velocity at particle position. Line color corresponds to St/A value, line color intensity to different St and A representations.	60
Figure 26	61
Figure 27	Nondimensional docking time calculated numerically with respect to St and A for arbitrary variable ranges with $\sigma = 10^{-5}$. Line of local maxima corresponds to $St = St_{\text{cr}}(A)$ and shows the stability border: particles to the left undergo in-orbit docking, particles to the right - axis docking.	63
Figure 28	Dimensional docking time as presented in Fig. 27 in the case $R = 13 \mu\text{m}$	63
Figure 29	Equilibrium curve plots for different A values. A_{cr} , r_s , r_i are defined in the text body. Gray dashed line shows an equilibrium curve which is an asymptotic limit of $A \rightarrow 0+$	65
Figure 30	Plot of the function $\phi(r_0^+)$ determining equilibrium point stability (a) and its square radius $\sqrt{\phi(r_0^+)}$ (b) with respect to equilibrium point radial position.	66

Figure 31	Equilibrium point r_0^+ position versus A . Line colors refer to various S_v parameters, continuous line - to stable point, dashed line - to unstable. The colored regions in the background mark various stability subdomains: light gray - a stable node, light green - a saddle, light red - a focus. Crosses show example of unstable foci in the light red region for the case of $St = 0.5$	68
Figure 32	Particle trajectory plots for various sets of (A, S_v, St) parameters. In each figure 25 particles are initialised at regular grid with zero velocity. Line colors vary in order to improve clarity. Scattered points represent equilibrium points position, their shape refer to their dynamical type: \times - a saddle, \circ - a focus (filled means stable), \square - stable node. "a" and "b" types present the same (A, S_v) sets, but with different St determining stability of the focus ("a" - stable, "b" - unstable).	69
Figure 33	Maximal strain parameter A_{\max} with respect to vortex core size δ and particle radius R , for an arbitrary alignment angle $\theta = \pi/4$	71
Figure 34	Maximal strain parameter A_{\max} with respect to particle radius R for a few vortex core sizes δ , drawn for a bundle of alignment angles. A_{cr} value is shown with a dashed line.	72
Figure 35	Histograms of droplet size counts measured with a PDI probe at the UFS on 27th and 29th of August 2011.	76
Figure 36	Droplet size probability distributions calculated for the data obtained with a PDI probe at the UFS on 27th and 29th of August 2011.	77

Figure 37	Examples of cloud voids observed at the UFS station with various camera-laser configurations. Images taken on 27 August (panel a) were chosen to estimate cloud void sizes. The ones recorded on 29 August evening (panel b) show the difference between inhomogeneities produced by cloud voids and those resulting from the mixing with clear air at the cloud edge. Other images from 29 August (panel c) suggest that the voids can be quite frequent in the sample volume. Bright spots and lines are due to presence of larger precipitation particles. 10 cm long segment is shown to represent spatial scale assumed in the void size calculation. For more details, see the movies attached in the supplementary materials.	79
Figure 38	Example close-ups of variously shaped cloud voids observed at the UFS station with different camera-laser configurations. 5 cm long section is placed in each image to represent spatial scale assumed in the void size calculation.	80
Figure 39	Approximated size range of particles $[R_1, R_2]$ that has a limit cycle solution, represented by color scale, with respect to vortex parameters (first and second row), R_s (third row), as defined in the text body and the interval between R_2 and R_s (fourth row), obtained numerically. Colorscale is common for R_1 , R_2 and R_s , separate for $R_2 - R_s$. Three alignment angle values selected are represented in columns. Vortex parameters domain corresponds to cloud-like conditions.	81
Figure 40	Numerical calculation of approximated size range of particles $[R_<, R_>]$ (first and second row) that create a cloud void, as well as interval between them ΔR (third row) in relation with vortex parameters. Colorscale is common for $R_>$ and ΔR . Three alignment angle values selected are represented in columns. Vortex parameters domain corresponds to cloud-like conditions. . .	82

Figure 41 Contour plot of stable periodic orbit radius for droplets of radii $R = 3, 13, 23 \mu\text{m}$ for cloud-like parameter ranges of δ and A . Overlapping (blue on a top, then pink and green) coloured surfaces match parameter domains in which stable periodic 2D orbit exist for droplet radius given by its colour. Dashed lines are contour plots for r_{orb} equal to 0.5 cm, 2 cm, 5 cm. Black points represent simulation parameters sets (filled later, referred to in ???). 84

LIST OF TABLES

Table 1	Cloud and turbulence basic data collected in different experiments: at UFS on Zugspitze mountain in Cu and Sc, during POST campaign in Sc, in CARRIBA campaign in Cu.	40
Table 3	Initial ($t^+ = 0$) and final ($t^+ = t_{\text{doc}}^+$) particle state in numerical simulations of docking processes. σ is an arbitrary small parameter.	55
Table 4	Burgers vortex non-dimensional numbers	64
Table 5	Existence and position of equilibrium points with respect to A and S_v parameters. A_{cr} , r_s , r_{\min}^+ , $S_{v \min}$, $S_{v \max}$ are defined in the text body.	65
Table 6	Stability conditions of particle equilibrium points present in the Burgers vortex with respect to vortex strain parameter A and dimensionless radial position r^+ . A_{cr} , $\varphi(r^+)$, r_s , r_i , r_{\min}^+ and r_{\max}^+ are defined in the text body.	67
Table 7	Single particle motion scenarios with respect to A and S_v parameters. Numbers refer to Fig.32	70
Table 8	Summary of single particle motion timescales	72
Table 9	Properties of turbulence and cloud droplets during 30-minutes long observation periods. Values of dimensionless parameters are calculated with the use of mean radius.	78

LISTINGS

ACRONYMS

DRY Don't Repeat Yourself

API Application Programming Interface

UML Unified Modeling Language

0.1 ORGANIZATION OF THE THESIS

The thesis content is organized into two main parts: introductory and resultant. Each part is preceded by an opening description. **Part i** is an introductory part and contains two chapters. **Chapter 1** provides necessary background by exploring literature of turbulence structure, particle-turbulence interaction and cloud droplet clustering and states the research problem of the thesis. **Chapter 2** in this part treats about research methods applied, both numerical and experimental. **Part ii** covers the main findings of the thesis presented in three chapters and summarised in the fourth. **Chapter 3** provides a detail analysis of single particle 3D motion in the chosen vortex model. **Chapter 4** describes experimental observations of cloud "voids" and applies the chosen model for polydisperse particles in order to explain them. In **Chapter 5** spatial patterns of droplets obtained in numerical simulations are evaluated. In **Chapter 6** the results are summarised and discussed, it presents final conclusions and suggestions for future work. The thesis closes with bibliography.

Part I

INTRODUCTION

Turbulent multiphase flows are present in numerous natural systems. They are a matter of current studies in many fields, including atmospheric physics, oceanography, astrophysics and technology. Such flows are characterized by a large complexity, due to the nonlinear nature and mutual couplings between different physical phenomena, i.e. flow dynamics, phase transitions, heat transfer, phase-to-phase interactions etc. One of such turbulent multiphase systems is an atmospheric cloud. Its complexity should encourage in-depth research, because according to latest IPCC report [25] "Clouds and aerosols continue to contribute the largest uncertainty to estimates and interpretations of the Earth's changing energy budget." However the cloud research has been progressing very slowly. One of the reasons for this is the poor understanding of the basics of turbulence phenomenon itself, including its multi-scale nature and the couplings between the many scales. Phenomena occurring in a cloud on a millimetre scale can be of great importance for a whole cloud system of hundreds of meters in size [23]. Therefore, it is perfectly justified to study very simplistic models operating even only on a small part of the cloud. The research presented in this thesis is motivated by such simplistic approach. Methods used in the following thesis neglect many effects connected to large scale dynamics in the atmosphere, as well as thermodynamic, radiative and chemical effects. These simplifications enable us to treat the cloud as a model set of polydisperse, heavy, inertial, sedimenting particles interacting with an incompressible, turbulent air flow. The work is aimed at studying spatial patterns of cloud droplets formed due to a presence of a single vortex model - a substitute of a turbulent flow. This way one of the mechanisms of interaction between particles and turbulence, particle clustering, is examined. The problems stated in the thesis are universal and fit into the current research on the general interaction between particles and flow in multiphase turbulent flows. The following introductory chapter states the research questions and hypotheses as well as put them into the perspective of recent advances in the topics of turbulence structure, atmospheric turbulence, particle clustering and its role in cloud evolution.

1

INTRODUCTION

1.1 RESEARCH PROBLEM EXPLORATION - LITERATURE REVIEW

1.1.1 *Turbulence*

Finally, there is a physical problem that is common to many fields, that is very old, and that has not been solved. It is not the problem of finding new fundamental particles, but something left over from a long time ago—over a hundred years. Nobody in physics has really been able to analyze it mathematically satisfactorily in spite of its importance to the sister sciences. It is the analysis of circulating or turbulent fluids.

— Richard Feynmann[22]

Richard Feynmann said these words more then 50 years ago and his message seems to be still valid. Fluid turbulence has attracted the attention of physicists, mathematicians, and engineers for over one hundred years. Phenomenon of turbulence present in nature is mostly associated with the observational aspects, which play far more important role due to the unsatisfactory state of "theory": a theory based on first principles simply does not exist. There is no consensus about physical definition of "turbulent motion" or agreement on mathematical "turbulence problem" to be solved. However unlike other complicated physical phenomena it is easy to observe at least some of the numerous manifestations of turbulence. Major qualitative universal features of turbulent flow, that form the "essence" of turbulence, are listed below.

1. Spatio-temporal apparent randomness (chaoticity).
2. Extremely wide range of strongly and non-locally interacting degrees of freedom ($\sim 10^{18} - 10^{29}$ in atmospheric flows [90]), hence its extreme complexity enforcing statistical description.
3. Chaotic nature (manifest itself by loss of predictability of turbulent flows), which at the same time posses statistically stable

properties.

4. Three dimensional and highly dissipative behaviour, thereby time irreversible and rotational. First two are probably the most specific and important attributes of turbulence.
5. Highly diffusive - turbulent flows exhibit strongly enhanced transport processes of momentum, energy and passive objects when compared to laminar flows.
6. Strongly nonlinear, non-integrable, nonlocal, non-Gaussian.

The true turbulence theory should predict and explain universal properties listed above. The best we have so far is the set of equations developed almost 200 years ago, that describe fluid motion - Navier Stokes equations (NSE). Most probably it contains all of turbulence. The problem is that we do not know global solution of these equations, and the knowledge of specific solutions does not lead to understanding the dynamics or structure of turbulent processes as a whole.

*Navier Stokes
equations*

The Navier Stokes equation is a deterministic, nonlinear partial differential field equation. It can be presented in two ways that are used to describe the fluid motion. One is called Lagrangian, where one follows fluid particles along their trajectories. The other is called Eulerian, in which the observation of the system is made in a fixed frame as the fluid goes by. In Eulerian formulation the NSE are as follows:

$$\underbrace{\frac{\partial \vec{u}}{\partial t} + \underbrace{\vec{u} \cdot \nabla \vec{u}}_{(2)}}_{(1)} = -\frac{1}{\rho} \nabla p + \underbrace{\nu \nabla^2 \vec{u}}_{(3)} + \vec{f} \quad (1)$$

where \vec{u} - fluid velocity, ρ - fluid density, p - fluid static pressure, ν - kinematic viscosity, \vec{f} - external forces.

Term (1) of NSE in this form is a standard partial time derivative. Term (2) represents advection of a fluid element. Those terms together create what is called the material derivative: $\frac{D}{Dt}$. Term (3) expresses pressure gradient and term (4) represents viscous forces.

Dimensionless version of the NSE brings to life dimensionless quantity that is very important in fluid mechanics - the so-called Reynolds number Re . It estimates the ratio of inertial forces (given by term (2) in 1) to viscous forces (given by term (4) in 1) within a fluid parcel. It can be presented with the use of characteristic scales of the fluid flow: U - velocity scale and L - length scale:

$$Re = \frac{UL}{\nu} \quad (2)$$

Reynolds number

The primary physical interpretation of the Reynolds number is that for small Re the flow is dominated by laminar motion and for large Re the flow is mostly turbulent [100]. The exact transition between these two regimes (at so called *critical Reynolds number* Re_{cr}) is specific for a geometry of the flow and has been a subject of separate, extensive studies. A quick estimation of the Re number for a cumulus cloud, in which $L \sim 1$ km, $U \sim 1$ m/s, $\nu \sim 10^{-5}$ m²/s, leads to $Re \sim 10^8$ and the conclusion that the airflow in the cloud is extremely turbulent, since typical Re_{cr} lays in in the range $10^2 - 10^6$.

critical Reynolds number

Though NSE have a limited kinetic foundation, it is commonly believed to be *adequate* i.e. its solutions corresponds to real fluid flows at all accessible Re , including turbulent flows. Unfortunately it is impossible to solve NSE analytically subject to most realistic initial and boundary conditions. For large Re the essence of the problem lies in the nonlinearity of the advection term (2) in Eq.1.

1.1.1.1 Phenomenology of turbulence

Because a field theoretical solution of the Navier Stokes equation is elusive, the fruitful approach comes from asking questions concerning the physics of the processes. The problem is to identify, interpret and explain major fundamental physical mechanisms that result in the universal properties of turbulence. The first such comprehensive attempt to explain these mechanisms is phenomenological theory of cascade [101] enriched and quantified by Kolmogorov hypotheses [64]. In the following, the foundations of these theories are outlined and the basic concepts commonly used in turbulence research are explained (description in this paragraph inspired by Pope [96] and Tsinober [121]).

Cascade concept postulates that in the flows of large Re kinetic energy enters the turbulence through a production mechanism at the largest scales of the flow. This energy is then transferred by inviscid processes to smaller and smaller scales, until, at the smallest scales, the energy is dissipated by viscous action. This concept defines a rate of turbulent kinetic energy (TKE) dissipation ϵ . The turbulent cascade scales emerge in the form of *eddies* - moderately coherent structures of turbulent motion localized in the region of size constrained by the arbitrary scale.

*TKE dissipation rate
eddy*

Kolmogorov hypotheses state that for every turbulent flow, at sufficiently high Reynolds number, there exist scales l_0 , l_{EI} , η such that:

- small-scale turbulent motions $l \ll l_0$ are statistically isotropic
- the statistics of the small-scale motions $l \ll l_{EI}$ have a universal form that is uniquely determined by ν and ϵ
- the statistics of the motions of scale l in the range $\eta \ll l \ll l_0$ have a universal form that is uniquely determined by ϵ , independent of ν

local isotropy hypothesis

1st similarity hypothesis

2nd similarity hypothesis

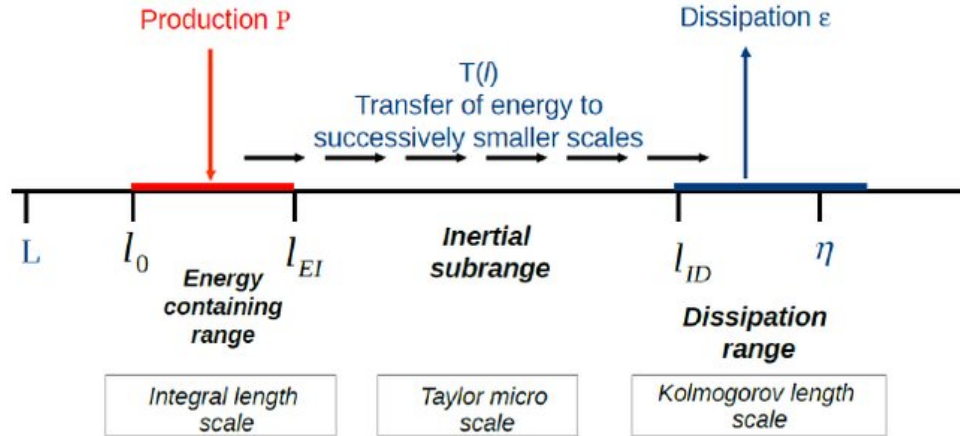


Figure 1: Turbulent eddy size ranges and transfer of energy diagram (from Saeedipour et al. [104]).

energy containing range
inertial range
dissipation range
Kolmogorov scales

Taylor microscale

Those hypotheses lead to a paradigmatic decomposition of the multiscale turbulence phenomenon to a few eddy size ranges illustrated schematically in the Fig. 1. The scales are ordered as follows: $L > l_0 > l_{EI} > \lambda > l_{ID} > \epsilon$. L is the flow scale. l_0 is the scale of the smallest anisotropic eddies affected by the boundary conditions of the flow and l_0 is comparable to L . l_{EI} demarcates between anisotropic eddies and smaller isotropic eddies of universal character. The range $[l_0, l_{EI}]$ is called *energy containing range* and have bulk of the energy production. *Inertial range* $[l_{EI}, l_{ID}]$, which is the name of the subrange described by 2nd similarity hypothesis, is governed only by inertial effects, viscous effects being negligible. The smallest scales, so called *dissipation range*, are described by 1st similarity hypothesis. Based on scaling argument, out of its only parameters ϵ and ν , Kolmogorov formed unique length, velocity and time scales for this range, which are now called Kolmogorov scales:

$$\eta \equiv (\nu^3 / \epsilon)^{1/4} \sim Re^{-3/4} l_0 \quad (3)$$

$$u_\eta \equiv (\epsilon \nu)^{1/4} \sim Re^{-1/4} u_0 \quad (4)$$

$$\tau_\eta \equiv (\nu / \epsilon)^{1/2} \sim Re^{-1/2} \tau_0 \quad (5)$$

Reynolds number based on Kolmogorov scales is equal to one: $\frac{\eta u_\eta}{\nu} = 1$. It is easy to see that the larger the Re based on the flow scales, the greater is the span of scales in turbulent fluid.

A well-defined quantity that is also often used in turbulence research (especially numerical simulations) is the *Taylor microscale* λ . It does not have a clear physical interpretation, but it is the intermediate length scale at which fluid viscosity significantly affects the dynamics of turbulent eddies in the flow. In Kolmogorov turbulence:

$$\lambda = \sqrt{15 \nu / \epsilon} u' \quad (6)$$

where \bar{u}' is turbulence intensity - a root mean square of velocity fluctuations. Reynolds number built on this scale is called *Taylor microscale Reynolds number* Re_λ .

Probably most important and commonly used conclusions from Kolmogorov's theory concern inertial range. Firstly there is the so-called " $-5/3$ law". In the Fourier space formulation, this law concerns energy spectrum function $E(\kappa)$, which describes energy spectrum for the fluid velocity Fourier modes of wavenumber κ (here κ is a module of a wavevector). It states that in the inertial range the energy spectrum is a universal function of κ and ϵ and is a power-law spectrum:

$$E(\kappa) = C\epsilon^{2/3}\kappa^{-5/3}. \quad (7)$$

-5/3 law

The constant C is called Komogorov universal constant and experimental data support the value $C \approx 1.5$. Recent extensive DNS for example point to $C \approx 1.64$ Gotoh, Fukayama, and Nakano [50]. This law is often used in the structure function formulation as well. By the definition *2nd order structure function* is a covariance of velocity difference between two points separated by \vec{r} : $\vec{x} + \vec{r}$ and \vec{x} :

$$D_{ij}(\vec{r}, t) = \langle (u_i(\vec{x} + \vec{r}, t) - u_i(\vec{x}, t)) (u_j(\vec{x} + \vec{r}, t) - u_j(\vec{x}, t)) \rangle \quad (8)$$

In locally isotropic turbulence $D_{ij}(\vec{r}, t)$ is determined by a single scalar function, the longitudinal structure function $D_{LL}(r, t)$. And, according to similarity hypothesis, for large r/η there is:

$$D_{LL}(r, t) = C_2(\epsilon r)^{2/3}, \quad (9)$$

in the inertial range, where C_2 is a universal constant. $C_2 = \frac{72}{55}C \approx 2$. So that the energy spectrum " $-5/3$ law" corresponds to the " $2/3$ law" in the structure function formalism.

Figure 2 is a part of Fig. 5 and 6 in Jen-La Plante et al. [59], a paper co-authored by the thesis author. It presents examples of power spectral density (PSD) and structure functions calculated for one dimensional velocity data collected in the Stratocumulus (Sc) cloud top during TO10 flight of POST campaign. PSD refers to the spectral energy distribution, that would be found per unit time, since the total energy of such a signal over all time would generally be infinite. Sc cloud top was split into several layers on the basis of turbulence, moisture and temperature field properties. Starting from the upper end of the Sc top, FT is free troposphere, TISL - turbulent inversion sublayer, CTMSL - cloud top mixing sublayer and CTL is the cloud top layer.

The second theoretical model often used in data analysis is the "Taylor hypothesis" or "frozen-flow hypothesis" for inertial range. It says, that in the case of statistically stationary flow with turbulence intensity small compared to mean velocity, we can approximate spatial

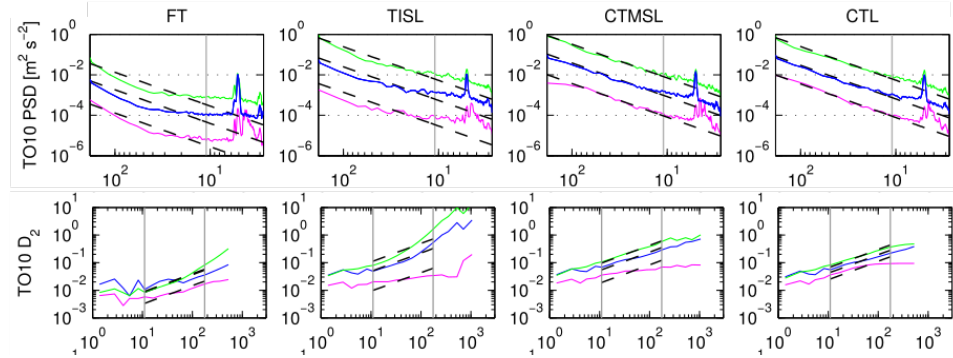


Figure 2: Power spectral density (PSD) and 2nd order structure functions (D_2) of velocity fluctuations of the three components u , v , w (blue, green, red) composites for all ascents/descents in single measurement flight (TO10) of POST campaign. Individual plots are shifted with respect to each other by factors of 10 for comparison, as indicated. Dashed lines show $-5/3$ slope for PSD or $2/3$ slope for D_2 fitted in a range of frequencies from 0.3 Hz to 5 Hz, in order to avoid instrumental artifacts at higher frequencies. Each column heading corresponds to Sc cloud top sublayer of different properties: FT- free troposphere, TISL - turbulent inversion sublayer, CTMSL - cloud top mixing sublayer, CTL - cloud top layer.

correlations by temporal correlations. Both the " $-5/3$ law" and Tylor hypothesis are commonly used to estimate ϵ from experimental data. This task is still however a matter of vivid discussion in cloud turbulence research [125, 138].

Kolmogorov's phenomenological theory is the only tool developed so well that it can characterize turbulent flow in many diverse applications. It even constitutes the language of many different turbulence descriptions. Despite being a good approximation of turbulence phenomenon, experimental premises indicate that a large part of its basic assumptions is flawed and many mechanisms are not captured. There is evidence that anisotropy in large scales causes anisotropy of small scales and that there is coupling between large and small scales [128]. The notion of "hierarchy" in turbulence is also being revised. Another important issue, not described by Kolmogorov's theory or its extensions, is the phenomenon of intermittency in small scales, inseparably connected with the notion of "structure" of turbulence. Intermittency and structure are the subject of the next paragraph.

1.1.1.2 Structure of turbulence

It is mostly agreed that turbulence posseses structure. It is agreed as well that some aspects of this structure are intimately related to *intermittency*. These topics have been addressed and detailed in the books by Arkady Tsinober [121, 122]. I summarised below some of the most important points.

Small-scale (or internal) intermittency is defined twofold: geometri-

cally and statistically, and these aspects are not independent. The geometric definition refers to some examined quantity x . This quantity is intermittent when for any small value x_0 , the volume of fluid in which $x > x_0$, decreases with increasing Re . In colloquial terms, when Re increases, our examined value of x is more and more "spiky" in its domain. Statistically a variable x with zero mean is intermittent if its probability distribution is such that extremely small and extremely large excursions are much more likely than in normally distributed variable (Gaussian).

Various experiments have shown that Lagrangian statistics in turbulent flows display Gaussianly distributed velocity values and non-Gaussianly distributed velocity differences or accelerations. Measured energy dissipation rate and vorticity are intermittent as well. Structures most probably responsible for the tails observed in the dissipative scales (sometimes referred to as *extreme events*) are predominantly in the form of vortex tubes and strain sheets. Earlier studies pointed that *vortex tubes* or "worms", are severely intermittent, coherent, elongated and long-lasting structures characteristic of high Reynolds number turbulent flows [84]. [79] show that these structures concentrate into clusters of the size in inertial range of scales. This implies the presence of large-scale organization of the small-scale intermittent structures. Review of the structures identification methods and the search results obtained in diverse turbulence generation setups was conducted in Wallace [126]. Some of most recent studies confirm the fact, that intense enstrophy-dominated regions are organized in small-scale vortex structures [124] and that these structures are strongly correlated with each other in space [137]. There are premises that such structures are present in inertial range as well [85]. The remaining question is if the structure changes when Re is increased. The old belief was that the only change produced by increasing the Reynolds number is the extension of the inertial range, with no other structural changes. Massive computations of last decade proof otherwise and provide new data about inertial range structures' features, in Reynolds numbers higher than ever. In Yeung P K, Zhai X M, and Sreenivasan Katepalli R [136] for example authors show that at $Re_\lambda = 1300$ (to that date it was the highest Re directly obtained numerically) with increasing Re , the extreme events assume a form that is not characteristic of similar events at moderate Re . Events as large as 105 times the mean value were obtained, albeit rarely. They appeared chunky in character, unlike elongated vortex tubes, and generally short-lived (see Fig.3). Extreme magnitudes of energy dissipation rate and enstrophy occurred essentially simultaneously in space and remained nearly colocated during their evolution. When imagining the structures in turbulent flow it is important to remember that "every part of the turbulent field just like the whole possesses structure." and the coherent structures mentioned above are not just simple ob-

vortex tubes

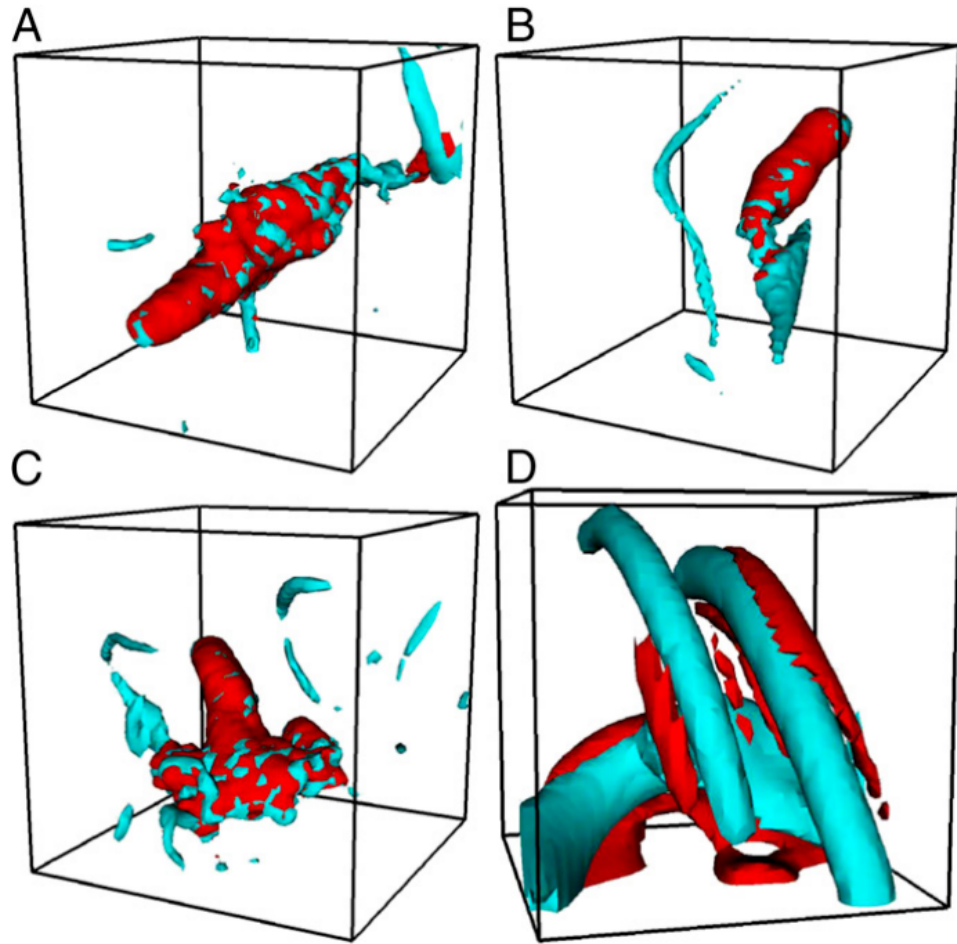


Figure 3: Perspective views of 3D contour surfaces of dissipation (red) and enstrophy (cyan) based on: (A-C) three instantaneous snapshots from the $8,192^3$ simulation at $R_\lambda \approx 1,300$, contrasted with data from (D) $2,048^3$ simulation at $R_\lambda \approx 400$. The contour thresholds used were 300 for data at $R_\lambda \approx 1,300$ and 70 for data at $R_\lambda \approx 400$. The subcubes are 51^3 in extent in A-C and 31^3 in D. Reprinted from Yeung P K, Zhai X M, and Sreenivasan Katepalli R [136].

ject embedded in the structureless background that can be "taken out of it".

The reports mentioned above, as well as other studies, mean that we do not really know what to expect in turbulence with even higher Re . The values achieved in the laboratory and simulations, although becoming higher and higher, are still far from those found in atmospheric turbulence. This is one of the reasons why we are not sure whether the results of the intermittency and structure research can be applied to the atmosphere. Therefore, the next paragraph is devoted to peculiarities of atmospheric turbulence.

1.1.1.3 Atmospheric turbulence

Turbulence in atmosphere, especially in clouds, influence many important processes: it governs entrainment and mixing, impacts cloud droplet evolution and interacts with large-scale cloud dynamics [23]. In-situ measurements of cloud-related turbulence are scarce and there are several reasons for that. Obviously it is not possible to have any control over the meteorological conditions. Observations made with research aircrafts are one-dimensional, prone to aerodynamic errors and of relatively low resolution due to large true airspeed. Measurements at mountain research stations are biased by orographic boundary conditions. Experimental equipment used must be resistant to hard meteorological conditions and large speeds/vibrations etc. Last but not least, field campaigns in atmospheric research are much more expensive than laboratory experiments. Despite these discouraging factors, the effort put into atmospheric turbulence measurement should pay off: after all, at our fingertips we have turbulence with the highest Re on Earth and a huge range of scales spanned between the smallest and largest eddies of turbulence, from parts of millimeters to kilometers. Little experimental evidence and complementary Direct Numerical Simulation (DNS) studies focused on atmospheric turbulence are summarised below.

Turbulence in the atmosphere is hard to analyse because of the presence of large scale anisotropies, inhomogeneity of turbulence field and nonstationary effects due to stratification, presence of liquid water and water vapor, aerosols of all kinds, sun heating, Coriolis force etc [133]. Part of my own research concentrated on some of these factors. On the basis of relatively large data set collected in the Physics of the Stratocumulus Top (POST) campaign by in-flight measurements, we tried to characterize turbulence and passive scalars properties in marine boundary layer clouds [59, 72]. The investigation revealed complex structure of Sc cloud and its surrounding, showing turbulence inhomogeneity at the range of scales reaching depth of inertial range. The transport of energy and momentum between these inhomogeneous spatial regions, called layers (TISL, CTMSL and CTL mentioned earlier in the text), is nonuniform, as well as the scaling behaviour of temperature and so called *liquid water content* (LWC, mass of the water in a cloud in a specified amount of dry air). But what is most distinctive in the results is strong anisotropy of turbulent motions at many scales [1]. Vertical fluctuations seem to be damped by static stability and horizontal fluctuations to be enhanced by large scale shear. This topic needs to be addressed more carefully, especially since some studies indicate that large scale anisotropy can be transmitted to small scales and be related with small-scale intermittency [129] or can totally change turbulence structure by appearing as large-scale intermittency[118]. The paradox however is that in all the turbulent studies in order to calculate turbulence properties such

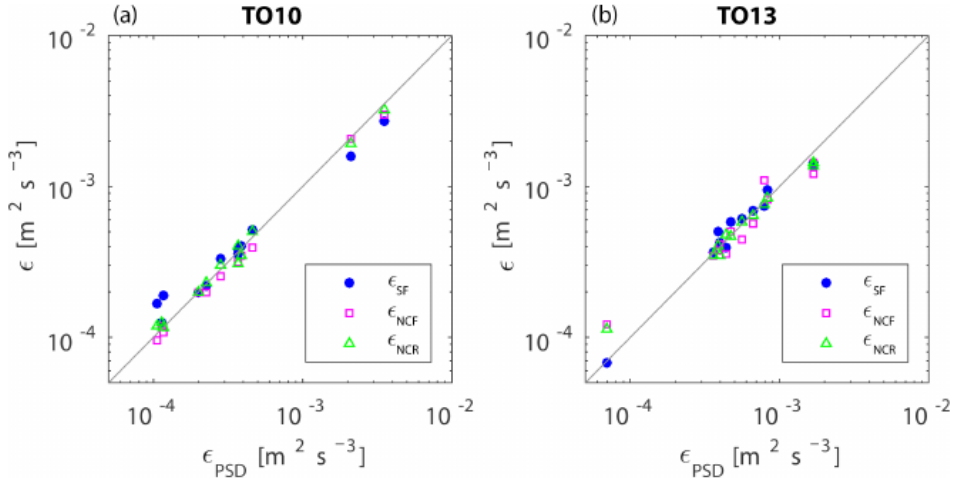


Figure 4: Dissipation rate of the kinetic energy estimated from the structure function method ϵ_{SF} , zero crossings of successively filtered signals ϵ_{NCF} and zero crossings of signals with recovered part of the spectrum ϵ_{NCR} as a function of ϵ_{PSD} (from the power spectra method). Each point represents an estimate from a single horizontal segment of flight in the atmospheric boundary layer. (a) POST flight TO10 (b) POST flight TO 13. Reprinted from Wacławczyk et al. [125]. Description of estimation methods available in the source paper.

as TKE, ϵ , η , assumptions of isotropy, homogeneity and stationarity of small scales of turbulence are taken. What is particularly interesting, is that dissipation range is usually still not resolved in the in-situ atmospheric measurements, but ϵ estimation attracts particular attention. Its value is smaller by a few orders of magnitude then typically observed in the laboratory [59, 114]. Some effort is put into improving ϵ estimation by accounting for low-resolution of the measurements (see Fig. 4 from Wacławczyk et al. [125]) or stratification and shear influence [138].

In conclusion, turbulence in the atmosphere, especially in the clouds, has properties that differ from turbulence created in the laboratory conditions. The language used to describe atmospheric turbulence is based on assumptions that are not fulfilled. Therefore, there is a need for research on its basic aspects, its structure and dynamics. This thesis by dealing with a simplistic model of cloud droplets moving in turbulence and trying to understand unique experimental evidence, offers a small contribution to the understanding of these basics. Next paragraph focuses on the great challenge which is efficient description of particle motion in the specific flow.

1.1.2 Single particle motion in the flow

In order to study the dynamics of particles advected by turbulent flow, one needs to have a simple formulation of the equations of motion of the advected particles. The problem is that particles of particular interest, namely cloud droplets, are finite-size, which means they are actually extended objects with their own boundaries. The rigorous way to analyse their dynamics would involve solving the Navier–Stokes equation for moving boundaries. The partial differential equations resulting from this approach are very difficult to solve and analyse. In many approximate derivations, the common concept that arises from the mathematical development is that of undisturbed fluid velocity, i.e. the velocity that the fluid would have had at the absence of the particle. In this way the flow is separated into the flow field as it would have been without particles, and the disturbance field. Widely used and very popular is the approximate differential equation for the motion of small spherical particle in the flow that was written down by Maxey and Riley in 1983 [77]:

*Maxey-Riley
equation*

$$\vec{v} = \dot{\vec{r}}, \quad (10)$$

$$m_p \dot{\vec{v}} = \underbrace{m_f \frac{D\vec{u}}{Dt}}_{(1)} - \underbrace{\frac{1}{2} m_f \left[\dot{\vec{v}} - \frac{D}{Dt} \left(\vec{u} + \frac{1}{10} R^2 \nabla^2 \vec{u} \right) \right]}_{(2)} - \underbrace{6\pi\mu R \vec{q}(t)}_{(3)} + \underbrace{(m_p - m_f) \vec{g}}_{(4)} - \underbrace{6\pi\mu R^2 \int_0^t d\tau \frac{d\vec{q}(\tau)}{d\tau} (\pi\nu(t-\tau))^{-\frac{1}{2}}}_{(5)} \quad (11)$$

where:

$\vec{r}(t)$ - position of the particle at time t ,

$\vec{v}(t)$ - velocity of the particle,

$\vec{u}(r(t), t)$ - undisturbed fluid velocity at the location of the particle,

$\vec{q}(t) = \vec{v}(t) - \vec{u}(\vec{r}(t), t) - R^2 \nabla^2 \vec{u}(\vec{r}(t), t)/6$ - particle-fluid velocity difference with correcting factor,

R - particle radius,

m_p - particle mass,

m_f - mass of the fluid displaced by the particle,

ρ_f - fluid density,

μ - fluid dynamic viscosity,

ν - fluid kinematic viscosity,

\vec{g} - gravitational acceleration,

and the derivatives:

$$\frac{D}{Dt} = \frac{\partial}{\partial t} + \vec{u} \cdot \nabla - \text{the material derivative (along fluid path),}$$

$$\frac{d}{dt} = \frac{\partial}{\partial t} + \vec{v} \cdot \nabla - \text{total derivative along particle trajectory.}$$

The *Maxey-Riley equation* (M-R) consist of a few terms which has the following physical interpretation.

- (1) - force exerted on the particle by the undisturbed fluid element in position $\vec{r}(t)$ at time t .
- (2) - *added-mass effect*, accounts for the fact that when the particle accelerates relative to the fluid, it displaces a certain amount of fluid with it.
- (3) - Stokes viscous drag.
- (4) - buoyancy force.
- (5) - Basset history term, arises from the fact, that the vorticity diffuses away from the particle due to viscosity.

The terms involving the factor $R^2 \nabla^2 \vec{u}$ (in (2), (3), (5)) are the *Faxén corrections*, and they account for the spatial variation of the flow field on particle surface. Simulations have shown however [2] that the Faxén correction becomes significant only for particles with diameter of several times the dissipative (Kolmogorov) length scale of the flow (unlike cloud droplets). M-R equation is generally valid for small particles, so $R < \eta$, at low particle Reynolds numbers Re_p . This Reynolds number is calculated by using the relative velocity between particle and neighbouring fluid as the velocity scale:

$$Re_p = R |\vec{v} - \vec{u}| / \nu. \quad (12)$$

This implies that for M-R eq. to be a valid approximation, the initial velocity difference between particle and fluid must be small. Another condition is that the shear Reynolds number $Re_\zeta = R^2 \zeta / \nu \ll 1$, where Γ is the typical velocity gradient in the flow, must be small. The M-R equation can be simplified with the adoption of appropriate assumptions. We call a particle:

*small, heavy,
inertial, sedimenting
particle*

- *heavy* when its density is significantly larger than fluid density $\rho_f \ll \rho_p$,
- *small* when its radius is significantly smaller than smallest fluid spatial scale $R \ll l_f$,
- *sedimenting* when its subject to gravity force
- *inertial* when its response time τ_p (to be defined) is larger than smallest fluid time scale $\tau_p > \tau_f$

When the particle follow these assumptions then the M-R eq. is of the form:

$$\vec{v} = \dot{\vec{r}}, \quad (13)$$

$$\dot{\vec{v}} = \tau_p^{-1} (\vec{u}(\vec{r}, t) - \vec{v}(t)) + \vec{g} - (5)/m_p \quad (14)$$

where $\tau_p = 2\rho_p R^2 / 9\mu$ is the particle inertial response time and (5) stands for the Basset history term. In this thesis droplet trajectories are calculated with the use of the approximated M-R equation- Eq.14 without history term (5):

$$\vec{v} = \dot{\vec{r}}, \quad \dot{\vec{v}} = \tau_p^{-1} (\vec{u}(\vec{r}, t) - \vec{v}(t)) + \vec{g} \quad (15)$$

The history term is omitted in this thesis due to its huge cost in numerical simulations. In the next section I discuss the applicability of certain M-R equation terms for cloud droplets in the vortex model.(?? czy na pewno dyskutuje gdziezies ???)

The other important class of particles are so called *tracers*: their density is equal to fluid density and they follow the flow exactly, unlike the inertial particles, which detach from the flow. The main difference between dynamics of tracer and inertial particles is that volume in phase space of tracers is conserved, whereas that of inertial particles shrinks. Tracers serve as benchmark particles in clustering studies.

tracers

Particle motion research require the use of some nondimensional numbers, which describe ratio of forces working on a particle. These are Stokes number *St*, sedimentation parameter *Sv* and Froude number *Fr*. *St* characterizes the inertia of the particle, while it is the ratio of the particle response time to fluid characteristic timescale.

Stokes number

$$St \equiv \tau_p/\tau_f$$

Sv is nondimensional settling velocity (the ratio of terminal velocity v_g to the fluid characteristic velocity v_f).

sedimentaion parameter

$$Sv \equiv v_g/v_f$$

The ratio of Stokes number to the sedimentation parameter is Froude number *Fr*. It expresses the same time the ratio of particle response time τ_p to the residence time of the particle in a Kolmogorov eddy.

Froude number

$$Fr \equiv St/Sv$$

Fr is considered a measure of the influence of gravitational force on the droplet motion. In the limit of a large Froude number, gravity is seen as negligible.

Thus equipped with the tools of single particle motion description, one may proceed to the complex issue of particle motion in turbulent flow.

1.1.3 Particle motion in turbulent environment

Many efforts were made to understand the dynamics of multiphase turbulent flows. Despite that few definite conclusions can be drawn. The development of Lagrangian techniques ("following" a particle motion in the fluid) in recent years has shed some new light on the relation between particle motion and fluid motion. However we are still far from creating a thorough theory describing how (and why) particles behave in turbulent flow. The dynamics and kinematics of fluid tracers themselves are in fact the subject of current discussion [6, 19, 43, 110, 120]. In case of inertial, heavy particles there are more questions than answers. Just to start, no comprehensive investigation of the consequences of all simplifications usually made in inertial particle motion studies has been made yet [26]. Some studies try to answer what is the accuracy of Stokes drag model (term (3) in Eq. ??) when comes to particle relative velocities (see Dou et al. [44] or Saw et al. [106] concerning water droplets in the air) or if Basset-history force, hydrodynamic interactions or turbulence small-scale anisotropy play any important role. Others consider the impact of Reynolds number as well as gravity[56, 57]. The issues raised above may substantially affect validity of the results regarding particle statistics in turbulence such as spatial distribution, collision probability, condensational growth or sedimentation velocity [34]. These statistics are especially important in cloud physics, as they determine rain formation process and cloud radiative properties. Better understanding how turbulence influences them by interaction with cloud droplets would lead to more precise characterization of cloud evolution[23]. Until now there has been a lot of theoretical and numerical research done but there is no agreement what are the key turbulent processes in this evolution (for reviews see Devenish et al. [42], Grabowski and Wang [51], Pumir and Wilkinson [97], Saito and Gotoh [105], Shaw [112], and Vaillancourt and Yau [123]). There are however some suggestions that the key processes are connected to the facts that even slight change of local droplet concentration (clustering, see next paragraph) or violent local turbulent events may influence cloud droplet growth significantly [3, 10, 65]. Experimental studies in the atmosphere [30, 48, 61, 63, 67, 75, 94, 111] and in the laboratory [58, 130] for long time have been inconclusive about the occurrence of clustering of cloud droplets on small-scales. Recently Larsen et al. [68] have finally revealed that there is statistically significant and unambiguous evidence of weak clustering on scales between about 1 and 5 mm (around 1m and 5m) for polydisperse set of cloud droplets larger than $10\mu\text{m}$ in weakly turbulent clouds. This thesis focuses on the turbulence influence on droplet spatial distribution (clustering) in the context of cloud evolution. Next paragraph introduces this problem broadly.

clustering

Clustering is the central term when talking about statistical change

in spatial distribution. It occurs when particle distribution deviates from random distribution, in our case due to the interaction of inertial particles with turbulent flow. There have been numerous studies on particle clustering motivated by industrial, geophysical or astrophysical applications. Most of the numerical and theoretical research focus on monodisperse and non-sedimenting particles in homogeneous, isotropic turbulence (HIT), and numerical simulations are conducted in Taylor microscale Reynolds number Re_λ which is a few order of magnitudes smaller than in the atmosphere. Thus application of such research to cloud droplet clustering is limited without further experimental investigation of polydispersity or gravity impact, matter of Re_λ increase or turbulence anisotropy/inhomogeneity influence. However, in order to properly address the complex problem, I will first review what has been achieved in a reduced problem.

Monodisperse, heavy inertial and non-sedimenting particle clustering in HIT in theory may be divided into three regimes: small-scale clustering, preferential sampling and short-time clustering due to caustics (or sling effect) - this division and review is available in Gustavsson and Mehlig [52]. *Small-scale clustering* occurs on scales smaller than correlation length of the flow which in realistic turbulence is spatial Kolmogorov scale η representing the size of dissipative eddies. Small-scale clustering demonstrates self-similarity (clustering properties are independent of scale) and is often described with statistical and dynamical methods developed for multifractals [9, 11, 12, 27, 46]. Yet analytical calculations concerning small-scales are possible only for substantially simplified statistical models of turbulence. The hope is that the only experimental work treating about dissipation-scale clustering, that was conducted by 1D measurements on polydisperse particles in low Re , large ϵ turbulence, is in qualitative agreement with the theory [108].

small-scale clustering

Preferential sampling or preferential concentration appears at inertial scales of turbulence when particles sample only regions of the flow that posses specific features. Most frequently cited approach to preferential concentration, generated for particles in small St expansion, is a so called "Maxey centrifuge" mechanism [76]. It claims that small heavy particles gather in straining regions of the flow and are centrifuged out of vortical regions. This concept was further developed in many numerical and theoretical studies (see for example CENCINI et al. [32] and Sigurgeirsson and Stuart [116]) and confirmed experimentally (for latest see Bhatnagar et al. [17]). Alternative description formulated on the basis of DNS simulation results is *sweep-stick mechanism* [36, 49], which states that particles stick to regions of low fluid acceleration as they are swept through the flow. There were some other theoretical and numerical views using statistical methods proposed as well, see for example Bec et al. [9], Falkovich G., Fouxon A., and Stepanov M. G. [45], and Hartlep, Cuzzi, and Weston [54].

Preferential concentration/sampling

sweep-stick mechanism

local Stokes number

Bragg, Ireland, and Collins [28] claim that actually physical mechanisms of clustering at dissipative and inertial scales in HIT are the same and they provide the fundamental explanation for this fact. The key parameter used in their analysis is the *local Stokes number* St_l defined for an arbitrary spatial scale $\eta \ll l \ll L$. It expresses the ratio of particle response time to $\tau_l = \langle \epsilon \rangle^{-1/3} l^{2/3}$ - the eddy of size l turnover time. For any separation $l \ll L$, the clustering mechanism for $St_l \ll 1$ is related to preferential sampling of the fluid velocity gradient tensor $\nabla \vec{u}$ coarse-grained at scale $\approx l$, which is associated with centrifuging out of eddies at that scale. They point as well the that this mechanism is in close relationship to sweep stick mechanism in the inertial range. For $St_l \geq O(1)$ a non-local mechanism contributes to the clustering process. One can take a lesson that when dealing with clustering, it is important to define the nondimensional parameters suited to the model used.

The other, quite new approach to clustering analysis puts in the center of attention the concept of coherent clusters of particles: their formation time, size, the local concentration in the cluster as well as their dependence on Re_λ , St , Sv , Fr . Baker et al. [8] and Momenifar and Bragg [80] on the basis of DNS analysis claim that particles in the cluster exhibit significantly higher degree of spatial organization and local accumulation, that their sedimentation velocity is higher than outside the cluster and that clusters align themselves with the local vorticity vector. Most of the experiments concerning preferential concentration focus on cluster and void analysis as well, using the technique of Voronoi triangulation [71, 81, 83, 87, 117]. Some of the research described here lead to the suggestions that turbulence intermittency and cluster/void formation are linked.

Clustering by *caustics* is the least known mechanism of the most complicated structure. The mathematical definition is that they are singularities in particle dynamics i.e. particles of totally different velocities meet in the same space point (see review in Gustavsson and Mehlig [52]). More picturesque formulation of the same mechanism is the sling effect: particle is expelled out of the vortex as if it was shot with a sling. They were observed in numerical simulations [4, 16, 47, 73]. Very recent works of Deepu, Ravichandran, and Govindarajan [40] and Ravichandran and Govindarajan [98] connect them directly to strong enhancement in particle collision probability.

Recent development in massive numerical computations made it possible to take into account other forces acting on the particle like computationally demanding Basset history force [88] or hydrodynamical interaction [82, 135] (so called "two-way coupling") and check if they impact clustering processes. The results of this work are not yet conclusive, but they lead to understanding that these forces may be of great importance. Meanwhile, sedimentation influence on clustering and vice-versa has already been explored in DNS and theory in more

detail [Park2014, 5, 7, 8, 14, 29, 41, 53, 57, 80, 103, 119, 127, 132]. Nevertheless the role of gravity in clustering remains an open field. For now, it seems that gravity weakens the clustering of small particles $St < 1$ and increases of large particles $St > 1$.

The advances in studies on clustering of monodispersed particles in HIT has been summarized above. The matter is far more complicated when it comes to the collection of polydispersed particles. Recognizing the influence of polydispersity on clustering is especially important when interpreting experiments with small particles and verifying a theory on experimental basis. Natural sets of particles (like cloud droplets), but also those produced in the laboratory, usually are biased by unavoidable polydispersity. Many of the DNS and laboratory experiments cited here as monodispersed particle studies have sections dedicated to polydispersity influence. First, but still unsolved problem in dealing with polydisperse particles is choosing statistical variables that can represent the size distribution with respect to clustering processes. There were many propositions, from mean arithmetic Stokes number, to various volume, surface or particle number weighted means. Secondly, the problem is the very way of describing clustering, which would capture its complexity. Some try to define a single measure of segregation [33], other analyze collective radial distribution function (RDF) [107, 109] as well as cluster sizes, structure and motion [69, 70]. Minier [78] reviews available statistical description methods of polydisperse, multiphase turbulent flows. Generally the scarce research agrees on a few topics. Even mild polydispersity (like $\Delta St > \langle St \rangle / 5$ in Saw et al. [107, 109]) reduces overall clustering. The lengthscale of droplet clusters falls into ranges 10-30, 20-30, 40-50 η (depends on the study), so in dissipation range. The lifetime is longer than τ_η and that more than just particle mean $\langle St \rangle$ is needed to statistically describe clustering. There is no agreement if there is dependence on Re_λ , turbulence intensity or shape of size distribution, or if cluster sizes depend on St .

From the above summary of research on clustering we can conclude that the basic mechanisms have still not been understood enough to grasp its impact on cloud evolution. *Tu jeszcze zdanie o wnioskach z powyzszego, do ktorych odwolujemy sie przy analizie dziur.* Next I follow the concept that structures connected to turbulence intermittency may play a significant role in particle spatial distribution change. However fully resolved simulations of NSE for atmospheric-like turbulence is beyond computational reach, hence the need to examine reduced models.

1.1.4 Vortex structures versus cloud droplet clustering

The concept of the paper by Kostinski and Shaw [65] is that the factor of-10 acceleration in the growth of the “lucky” droplets (the fastest

one-in-a-million) combined with traditional turbulent cascade ideas is enough to explain the size-gap problem in cloud droplet growth theory. This gap, called condensation-coalescence bottleneck as well, is a lack of understanding the processes bringing in around 15 min cloud droplets, that grew by condensation to around 20 μm in radius, to 40 μm , for which size gravitational collisions become effective growth process. Although the Kostinski and Shaw [65] paper did not explain how to get such a fast growing lucky droplet, it gave the lesson that even very rare local events may have great impact on global state of a cloud. Bec et al. [10] showed in statistical analysis of DNS that there is precise connection between the intermittent nature of the carrier turbulent flow and the accelerated growth of particles by increased collisions. However one may miss important information when paying attention to global statistics only, for example where and how these collisions occur. For this reason, the researchers studying the distribution and collisions of particles in the flow, became interested in the trend of searching for coherent structures in turbulence that can influence these processes [13, 18, 20, 38, 91].

It was mentioned before, that intense vortex structures (or vortex tubes) probably play important role in turbulence intermittency and hence may have particular impact on dynamics of heavy inertial particles. Previous efforts to study this dynamics in vortices were made by simulating droplet trajectories in a prescribed velocity field for several simple single-vortex models. Such research for the simplest model of a line vortex with stretching was conducted by Markowicz, Bajer, and Malinowski [74] with limitation to horizontally oriented vortices. Some specific features of droplet trajectories for monodisperse droplets in another model, a Burgers vortex with stretching, were examined in 2D by Marcu, Meiburg, and Newton [73] for arbitrary alignment with respect to gravity and by Hill [55] for horizontal alignment together with collisions. Ravichandran, Perlekar, and Govindarajan [99] studied the behaviour of particles near fixed points, with no gravity, between two like-signed vortices. Ravichandran and Govindarajan [98] analysed Lagrangian density around the particle in 2D point vortex, gaussian vortex and collection of point vortices (no gravity), especially with respect to caustics formation. [40] used this analysis for polydisperse droplets to show growth of particles by increased collisions around single vortex. Picardo et al. [93] in the DNS of turbulent flow (without gravity) indicate the regions that are possibly responsible for enhanced collision probability - vortex-strain worm-rolls - and claim that particles in intense vortex tubes are rapidly ejected into strong straining sheets. On the whole, interest in the topic of the vortices role in particle clustering and collisions has been considerable in recent years. My research was part of this trend and surely filled in one of the gaps. Namely, in my investigation I took into account the 3D motion of a particle under gravity force as well

as described the collective motion of polydispersed particles in a vortex as a proxy of droplets in a real cloud turbulence.

1.2 RESEARCH PROBLEM STATEMENT

Generally the objective of this research is to show that in cloud turbulence, presence of a long-lasting, violent vortical structure is probable and it can cause strong local clustering and segregation of cloud droplets. There are several research ideas behind it. I assume that the motion of a single sedimenting particle in the Burgers vortex model with stretching can be described by means of the formalism of dynamical systems. For some sets of vortex and particle parameters the motion of a particle in two dimensions is determined by different types of attractors and cannot be reduced to Maxey centrifuge mechanism. First hypothesis is that these 2D attractors are crucial in 3D particle motion as well. Second hypothesis states that there is significant clustering of particles near the vortex and in polydispersed systems it leads to a strong size segregation.

Another goal of this thesis is to describe in detail first-of-a-kind observations of relatively large heterogeneities in the form of near-circular "voids" in atmospheric clouds [134]. This work attempts to answer the question whether these structures can be explained solely by the presence of a strong vortex in the field of cloud droplets when modelled according to the above assumptions. Complementary study identifies the conditions under which the void phenomenon in the selected model is created and indicates the potential high impact of imaging technique on voids observation. To the best of author's knowledge, the most novel aspects of this work are complexity of the model chosen for analysis and its application to explain unique in-situ experiment results.

Verification of hypotheses set in this thesis is conducted with the use of simplified model. Particles are small, sedimenting, heavy, inertial and noninteracting with each other, a vortex tube model is Burgers vortex with stretching. The only forces working on particle is Stokes drag and gravity and there is no hydrodynamical interaction between particle and the flow. Due to numerical power limitations, the Basset history force is not included in particle motion simulations. Its role in particle motion in turbulence is a subject of most recent, separate studies. Collisions of particles are not taken into account to extract vortex influence on pattern formation only. Another consequence of numerical power limitations is that simulations do not reproduce the particle number concentrations corresponding to cloud values.

I assume that a single, steady, stationary vortex is a good proxy for a rare vortical event in high Re turbulent flow as to inspect particle motion inside the structure. The Burgers vortex is a reasonable ap-

proximation of such a localised in time and space single vortex in the flow, as discussed in Wilczek [131].

As far as the observations are concerned, it is assumed that the measurement results from mountain-top observatory were not disturbed by the presence of boundaries. Further in the text there is discussion of this assumption. What is most important, however, is that I analysed one and only case of cloud "voids" ever recorded. These observations were the only one of its kind and have not been repeated to this day. During my doctoral studies I was preparing a measurement campaign to confirm these results, with the use of a newly designed device. The prepared equipment, operating well in laboratory conditions, did not comply with harsh conditions present in a cloud at the mountain observatory. The experimental difficulties accompanying the registration of a single droplet in a real cloud are described in the following chapters.

2

METHODS

This Chapter establishes research methods applied in the thesis. Section 2.1 introduces Burgers vortex analytical model and provides literature review for adjusting model parameters. Section 2.2 presents the basics of dynamical systems formalism and brings concepts used for describing the single particle motion in a model of a vortex. Section 2.3 makes a preliminary analysis of the particle equation of motion, tracks the steps to its numerical solution and sets the assumptions for the proper, multiple particle model specific for this thesis. Section 2.4 is devoted to experimental techniques and observation details. Last, but not least, Section 2.5 collects the data on the properties of cloud droplets and cloud turbulence, to establish "cloud-like" conditions that are applied in numerical simulations.

2.1 VORTEX MODEL

A model of intense vortex structure chosen for the analysis is Burgers vortex with stretching [31]. It is exact, axisymmetric, steady solution to NSE and a product of balance between stretching effect and viscous diffusion [92]. It is commonly used as an approximation of a vortex tube in DNS and laboratory experiments [15, 60, 86]. Despite its simplicity and limited connection to 3D turbulence, Burgers vortex serves as a testing ground for many physical and mathematical ideas.

Burgers vortex is a 3D steady velocity field \vec{u} determined by two parameters: *circulation* Γ and *stretching strength* γ . The irrotational motion sweeps vorticity radially inward while simultaneously straining the vortex tube in the axial direction, as presented schematically in Fig. 5. These processes exactly counterbalance the tendency for vorticity to diffuse radially outward and as a result it is constant in time. If vortex axis is aligned with z -axis in the cylindrical coordinate system (r, φ, z) , then its vorticity:

$$\vec{\omega}_{Bur} = \frac{\Gamma}{2\pi\delta^2} e^{-\frac{r^2}{2\delta^2}} \hat{e}_z \quad (16)$$

and velocity field:

$$\vec{u} = -\frac{\gamma}{2} r \hat{e}_r + \frac{\Gamma}{2\pi r} \left(1 - e^{-\frac{r^2}{2\delta^2}} \right) \hat{e}_\varphi + \gamma z \hat{e}_z, \quad (17)$$

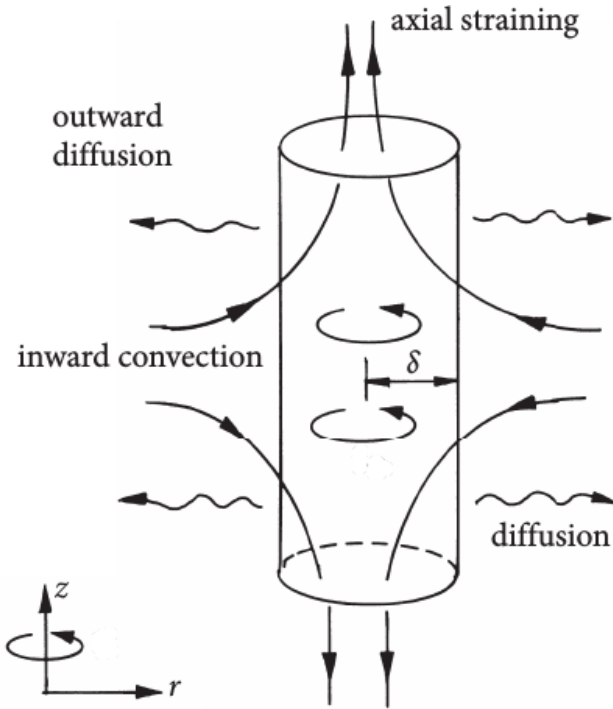


Figure 5: Straining of vorticity in Burgers vortex. δ is vortex core size (from Davidson [39]).

vortex core size
vortex turnover time

where $\delta = \sqrt{2\nu/\gamma}$ is the *vortex core size*. The characteristic timescale of the Burgers vortex flow, *vortex core turnover time*, is:

$$\tau_f = \delta^2 \Gamma^{-1} \quad (18)$$

By the definition, azimuthal velocity reaches its maximum at $r = r_s \delta$, where $r_s = \text{const}$, so the definition introduces a spatial scale r_s into the system. Precise analytical formulation is such, that $r_s = \sqrt{-2W(1, -\exp(-1/2)/2) - 1}$, where $W(k, x)$ denotes Lambert W functions' k -th branch of x . For the purposes of this thesis, only the numerical estimation is used: $r_s \approx 1.5852011$. Burgers vortex velocity components scaled with vortex spatial and time scales, δ and τ_f , are:

$$\vec{u}^+ = -A r^+ \hat{e}_r + \frac{1}{2\pi r^+} \left(1 - e^{-\frac{r^+}{2}} \right) \hat{e}_\varphi + 2A z^+ \hat{e}_z \quad (19)$$

where $A = Re_v^{-1}$ is vortex strain parameter, defined later in the text, and $+$ denotes dimensionless variables. Three dimensionless velocity components are plotted in Fig.6 for $A = 0.001$.

In order to adjust the model to atmospheric turbulence application, one needs to calibrate model parameters. Past theoretical and experimental studies lack general conclusions about vortex characteristic time and length scales, intensity and appearance in turbulence. Most of this inconclusive information that is available is summarised here. Statistical analysis of DNS data [15, 60, 79, 95] and of experimental data [84] indicate that Burgers vortex core size δ

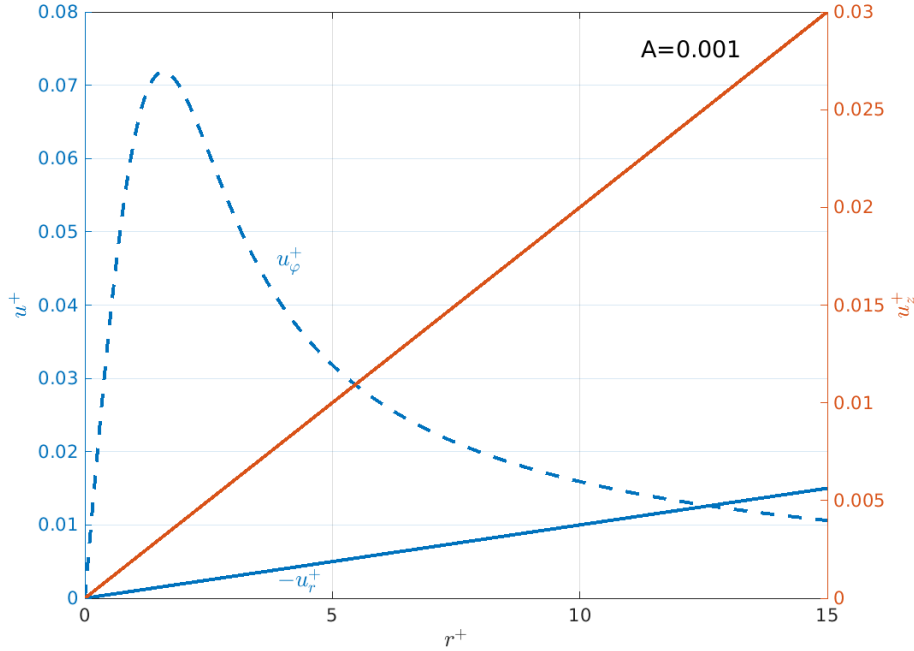


Figure 6: Burgers vortex dimensionless velocity components in cylindrical coordinates. u_ϕ does not depend on any parameter. The rest is plotted for an arbitrarily chosen strain parameter $A = 0.001$. r_s is defined in the text.

has a log-normal probability distribution. It scales roughly with the Kolmogorov length scale: $\delta = m\eta$ and m range varies in different papers. Generally its minimum reaches 1 and maximum around 12–22. The mean values fall into the range $\langle m \rangle = 3 – 7$. Jimenez and Wray [60] estimates the length of a tube and claim that it scales as $\simeq Re_\lambda^{1/2}$. All these studies had relatively low Reynolds number: $Re_\lambda \simeq 100 – 1000$. Belin et al. [15] reports that the vortex Reynolds number is $Re_v = \Gamma/\nu \approx 200 – 400$. This research, among other papers, shows that azimuthal velocity decreases much faster far from the axis than in Burgers vortex model. Pirozzoli [95] investigated this issue as well, but in more detail. Moisy and Jimenez [79] analyzing DNS instant velocity fields propose that vorticity structures' geometrical aspect ratios evolve towards long tubes ($1 : 1 : 10$), while increasing vorticity threshold. In the study by Biferale, Scagliarini, and Toschi [21], statistics of vortex filament lifetime for a low Taylor microscale Reynolds number Re_λ indicate that the maximum lifetime is on the order of the integral timescale, whereas its mean lifetime scales with the Kolmogorov timescale. Many of the works cited here suggest that there is a relation between root mean square velocity fluctuations \bar{u}' and the circulation parameter Γ .

Tu dodac jeszcze jedna informacje o skalowaniu.

2.2 DYNAMICAL SYSTEMS FORMALISM

Dynamical systems theory includes an extensive body of knowledge about qualitative properties of generic smooth families of vector fields and discrete maps. The theory abandons the goal of describing the qualitative dynamics of all systems as hopeless and instead restricts its attention to phenomena that are found in selected systems. Here are presented the dynamical phenomena that are relevant to deterministic system of a single particle moving in Burgers vortex as determined by Eq.15.

Topological features of a dynamical system - singularities, periodic orbits, and the ways in which the orbits intertwine - are invariant under a general continuous change of coordinates. Equilibria and periodic orbits are flow invariant sets. Local quantities such as the eigenvalues of equilibria and periodic orbits, and global quantities such as Lyapunov exponents, metric entropy, and fractal dimensions are examples of properties of dynamical systems independent of coordinate choice. That is why these quantities are good descriptors of flow structure. The definitions of several of the above are given below.

dynamical system

A *dynamical system* is a triple $\{M, f, T\}$ consisting of manifold M called the phase (or state) space endowed with a family of smooth evolution functions f^t that for any time $t \in T$ map the manifold into itself: $f^t : M \mapsto M$. In the case of continuous-time dynamical system and real time $t \in \mathbb{R}$, the family $\{f^t\}_{t \in T}$ of evolution operators is called a *flow* (under additional conditions). A *flow map* for a given t transforms a state vector $x_0 \in M$ into another state vector $x \in M$:

$$f^t : x_0 \mapsto x(x_0, t) \quad (20)$$

trajectory and orbit

A sequence of points $x(t) = f^t(x_0)$ for t in finite range is called the *trajectory* through the point x_0 . A trajectory can be stationary, periodic or aperiodic. An *orbit* refers to totality of states that can be reached from the point x_0 .

Continuous dynamical system can be written as system of coupled ordinary differential equations. When a dynamical system is represented by a set of equations $\dot{x}(t) = v(x, t)$, then $v(x, t)$ is called a *generalized velocity field*.

equilibrium point

Equilibrium point x_k (also referred to as a stationary, fixed, critical, invariant, rest, stagnation) is a state vector for which $\forall t v(x_k, t) = 0$ (equivalently $\forall t f^t : x_k \mapsto x_k$). A *periodic orbit/cycle* p is the set of points $M_p \subset M$ swept out by a trajectory that returns to the initial point in a finite time.

periodic orbit

attractor

An *attractor* Ω is a subset of M onto which a flow is contracting i.e. there exists a connected state space volume that maps into itself under forward evolution. The attractor may be unique, or there can coexist any number of distinct attracting sets, each with its own *basin of attraction* - the set of all points that fall into the attractor under forward evolution. The attractor can be a fixed point (a sink), a periodic

orbit (a limit cycle), aperiodic, or any combination of the above. Conversely, if we can enclose a set Ω by a connected state space volume $M_0 \subset M$ and then show that almost all points within M_0 , but not in Ω , eventually exit M_0 , we refer to Ω as a *repeller*.

The state space M is stratified into a union of orbits. In order to understand the dynamics of the system it is enough to understand how M is stratified and to grasp the nature of its orbits. The central term in this process is stability. Stability matrix is a basic tool characterizing the stability of an orbit:

$$A_{ij}(x) \equiv \frac{\partial}{\partial x_j} (v_i(x)) \quad (21)$$

where $x = x(x_0, t)$ is a trajectory. It expresses the rate of the infinitesimal neighbourhood deformation along the trajectory. However to get to know finite time deformation needed for stability analysis, one needs to know the Jacobian matrix J^t . Its relations to stability matrix are provided here only for the cases of interest to this thesis: equilibrium points and periodic orbits.

For equilibrium point x_k the Jacobian matrix is:

$$J^t(x_k) = e^{A(x_k)t} \quad (22)$$

hence the stability of equilibrium point x_k is determined by eigenvalues of stability matrix $\lambda_k^{(l)} = a_k^{(l)} + i b_k^{(l)}$. Assuming that these eigenvalues are non-degenerate, $\lambda^{(l)} \neq \lambda^{(m)}$ for any pair of eigenvalues, the following claims are present.

- If all $a^{(l)} < 0$, then the equilibrium is stable - a *sink*. For $b^{(l)} = 0$, it is an *stable node*; for $b^{(l)} \neq 0$, it is an *stable spiral/focus*.
- If some $a^{(l)} < 0$, and other $a^{(l)} > 0$, the equilibrium is hyperbolic, or a *saddle*.
- If all $a^{(l)} > 0$, then the equilibrium is repelling, or a *source*. For $b^{(l)} = 0$, it is an *unstable node*; for $b^{(l)} \neq 0$, it is an *unstable spiral/focus*.
- If $\det A(x_k) = 0$, $\text{tr} A(x_k) \neq 0$ it is neutral, a *center* (elliptic).
- If some $a^{(l)} = 0$ there is a symmetry or a bifurcation.

Figures 7 and 8 show diagrams of number of equilibrium point examples. It is important to realise that these examples are pictured in phase space, not in real space.

A periodic orbit of a continuous-time flow can be:

- stable, a sink or a *limit cycle*,
- hyperbolic or a saddle, unstable to perturbations outside its stable manifold,

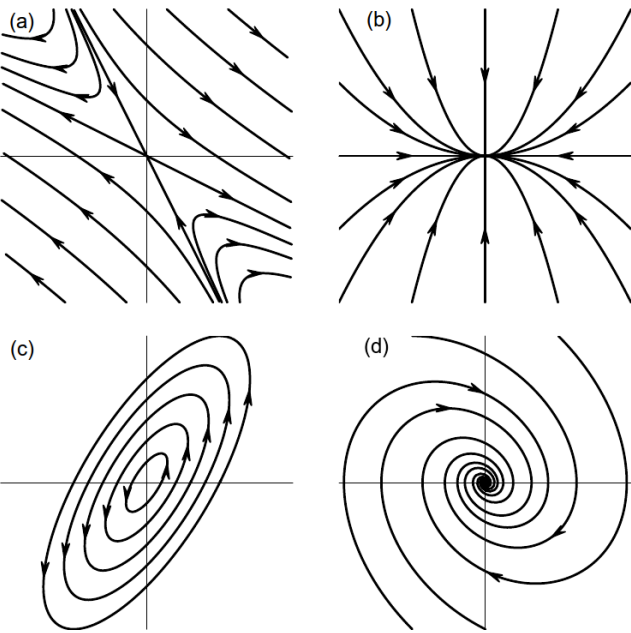


Figure 7: Trajectories in linearized neighborhoods of several 2-dimensional equilibria: (a) saddle (hyperbolic), (b) stable node (attracting), (c) center (elliptic), (d) stable spiral (from Cvitanović et al. [37]).

- elliptic, neutral or marginal,
- partially hyperbolic,
- repelling, or a source, unstable to any perturbation

The range of system parameter values for which a periodic orbit is stable is called its *the stability window*. The set of initial points that are asymptotically attracted to stable periodic orbit in infinity (for a fixed set of system parameter values) is called *the basin of attraction* of the limit cycle. For the detailed analysis of periodic orbit stability conditions see [37].

Hopf bifurcation

Bifurcation is a change of the topological type of the system as its parameters pass through a *bifurcation (critical) value*. One of the classes of bifurcations is so called *Hopf bifurcation* [66]. Suppose α is a bifurcation parameter and $\alpha_{cr} = 0$ is the critical value. In Hopf bifurcation, for $\alpha \leq 0$ the equilibrium is a stable focus. If $\alpha > 0$ the equilibrium becomes an unstable focus and the system has a stable periodic orbit. This is presented schematically in Fig.9.

In order to use the methodology described above to analyze the motion of a particle in a vortex of axial symmetry, it is necessary to first define the state space. When choosing a cylindrical coordinates in \mathbb{R}^3 the position vector is $\vec{r} = \vec{r}(r, \varphi, z)$, the state vector is $\mathbf{x} = (r, \varphi, z, \dot{r}, \dot{\varphi}, \dot{z})$ and generalized velocity $\mathbf{v} = (\dot{r}, \dot{\varphi}, \dot{z}, \ddot{r}, \ddot{\varphi}, \ddot{z})$.

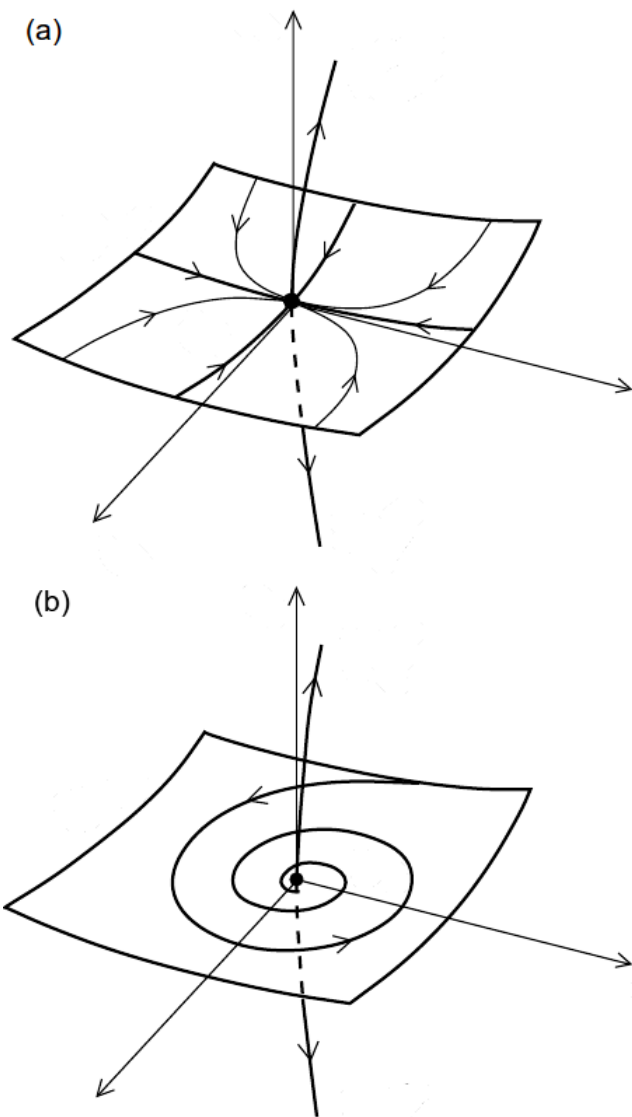


Figure 8: Trajectories in linearized neighborhoods of 3-dimensional equilibria: (a) saddle, (b) saddle-focus.

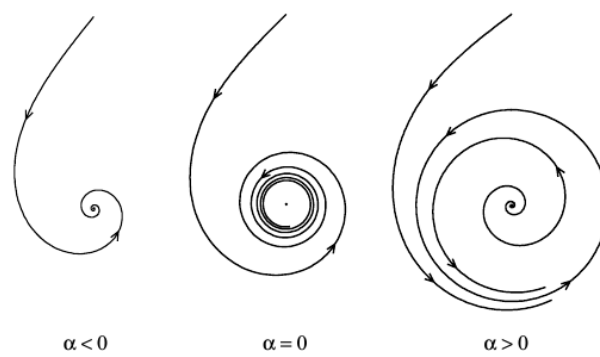


Figure 9: Hopf bifurcation depicted in a plane. α is bifurcation parameter, its critical value is $\alpha_{cr} = 0$. The figure comes from [66].

2.3 NUMERICAL SIMULATIONS

2.3.1 Single particle trajectory

Solving Eq. 15, the equation of particle motion, for arbitrary parameters and initial conditions, even in steady vortex flow as defined in ?? requires numerical calculations. Below are described the consecutive steps needed to perform these calculations. First few steps of the procedure are also of use for analytical analysis.

In the rectangular coordinate system, in which z axis is aligned with vortex axis, gravity force vector, without loss of generality, is defined to be inclined by the arbitrary angle $\theta \in (0, 90^\circ]$ to vortex axis:

$$\vec{g} = -g (\sin \theta \hat{e}_y + \cos \theta \hat{e}_z) \quad (23)$$

where g is gravitational constant. In cylindrical coordinates:

$$\vec{g}/g = -\sin \theta \sin \varphi \hat{e}_r - \sin \theta \cos \varphi \hat{e}_\varphi - \cos \theta \hat{e}_z, \quad (24)$$

$$\ddot{\vec{r}} = (\ddot{r} - r\dot{\varphi}^2)\hat{e}_r + (2\dot{r}\dot{\varphi} + r\ddot{\varphi})\hat{e}_\varphi + \ddot{z}\hat{e}_z. \quad (25)$$

Equation 15 decomposed into components looks therefore as follows:

$$\ddot{r} - r\dot{\varphi}^2 = \tau_p^{-1} (-\gamma r/2 - \dot{r}) - g \sin \theta \sin \varphi \quad (26)$$

$$2\dot{r}\dot{\varphi} + r\ddot{\varphi} = \tau_p^{-1} \left(\frac{\Gamma}{2\pi r} (1 - \exp(-\gamma r^2/4\nu)) - r\dot{\varphi} \right) - g \sin \theta \cos \varphi \quad (27)$$

$$\ddot{z} = \tau_p^{-1} (\gamma z - \dot{z}) - g \cos \theta \quad (28)$$

The system is primarily dependent on a set of six dimensional parameters: $\{\Gamma, \gamma, \theta, \tau_p, g, \nu\}$. The non-dimensionalization however leads to Eq. ??-?? and gives a set of 4 dimensionless parameters $\{St, S_v, \theta, A\}$ to be defined below. Dimensionless variables are denoted henceforth by $+$.

$$\ddot{r}^+ - r^+ \dot{\varphi}^{+2} = -St^{-1} (Ar^+ + \dot{r}^+ + S_v \sin \varphi) \quad (29)$$

$$2\dot{r}^+ \dot{\varphi}^+ + r^+ \ddot{\varphi}^+ = St^{-1} \left(\frac{1}{2\pi r^+} (1 - e^{-\frac{r^+2}{2}}) - r^+ \dot{\varphi}^+ - S_v \cos \varphi \right) \quad (30)$$

$$\ddot{z}^+ = St^{-1} (Az - \dot{z}^+ - S_v \cot \theta) \quad (31)$$

vortex strain parameter

A quantity $A = \nu \Gamma^{-1} = Re_v^{-1}$ is the dimensionless strain parameter, the inverse of vortex Reynolds number Re_v . Stokes number here is calculated with the use of vortex turnover time τ_f so $St = \nu \tau_p A^{-1} \delta^{-2}$. The sedimentation parameter is $S_v = \nu^{-1} g A \delta \tau_p \sin \theta$. It characterizes the motion in a plane perpendicular to the vortex axis (r, φ), that is called here *2D space*. As one can see the equation describing particle motion along the vortex axis (Eq. ??) are independent from the equations describing motion in 2D space (Eq.??, ??), i.e. they depend on different variables. Thus they can be solved separately. The analysis

of single droplet motion using similar formalism was conducted by Marcu, Meiburg, and Newton [73].

The set of equations 29-31 is used next to transcribe the state vector evolution:

$$\dot{\mathbf{x}}^+ = \frac{d}{dt^+} \begin{bmatrix} r^+ \\ \varphi \\ z^+ \\ \dot{r}^+ \\ \dot{\varphi}^+ \\ \dot{z}^+ \end{bmatrix} = \begin{bmatrix} \dot{r}^+ \\ \dot{\varphi}^+ \\ \dot{z}^+ \\ -M_1 r^+/2 - M_2 \dot{r}^+ - M_3 \sin \varphi^+ + r \dot{\varphi}^{+2} \\ M_2 (1 - \exp(-r^{+2}/2)) / 2\pi r^{+2} - M_3 \cos \varphi^+ / r^+ - 2\dot{r}^+ \dot{\varphi}^+ / r^+ - M_2 \dot{\varphi}^+ \\ M_1 z^+ - M_2 \dot{z}^+ - M_4 \end{bmatrix} \quad (32)$$

while for convenience, new equation parameters are defined:

$$M_1 = \frac{2A}{St} = \frac{\tau_p}{\gamma^{-1}} St^{-2}, \quad (33)$$

$$M_2 = St^{-1},$$

$$M_3 = Fr^{-2}, \quad (34)$$

$$M_4 = Fr^{-2} \cot \theta.$$

In such a form the set of dimensionless equations (Eq. 32) is solved numerically in Matlab environment by *ode45* build in solver, which is based on an explicit Runge-Kutta (4,5) formula, the Dormand-Prince pair. It is a single-step solver and it uses adaptive time steps. Relative error tolerance assumed is 10^{-3} , absolute error tolerance is 10^{-6} .

2.3.2 Multiple particles in vortex domain

To imitate processes occurring in clouds and examine the effect exerted on a droplet field by the presence of a vortex, a 3D vortex model was designed. Its domain is cylindrical in shape, of radius D and half-length Z (see Fig. 10). Initially the domain is filled uniformly with a given number concentration n of particles. No interaction between droplets is imposed. During the course of simulation, particles leaving the simulation domain are removed.

New particles are constantly placed in the simulation domain in the following way. Cylinder shell of constant width $\Delta r_{box} = 200\mu\text{m}$ (chosen as a compromise between largest particle size and grid accuracy) is discretized by imposing a rectangular grid on it, where one grid box has real dimensions $(\Delta r_{box}, \Delta \varphi_{box}, \Delta z_{box})$ and volume V_{box} .

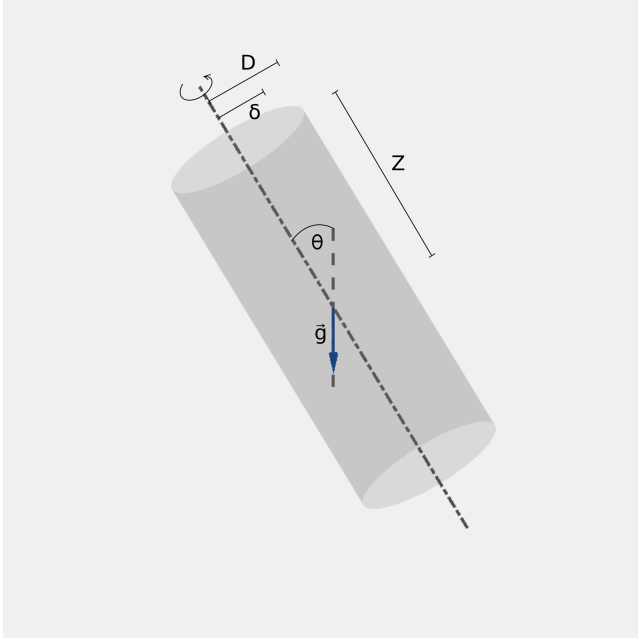


Figure 10: A scheme of numerical simulation's vortex model domain. D is cylinder radius, Z is its half-length, δ is vortex core size, θ is gravity alignment angle, \vec{g} is gravity direction.

$$\Delta r_{\text{box}} = \Delta z_{\text{box}} = 200 \mu\text{m}, \quad (35)$$

$$\Delta \varphi_{\text{box}} = \Delta r_{\text{box}}/D, \quad (36)$$

$$V_{\text{box}} = \Delta r_{\text{box}}^3, \quad (37)$$

$$\vec{v}_{\text{box}} = \vec{u}_r(r = D) = -\gamma D/2 \hat{e}_r, \quad (38)$$

$$iN_i = n * V_{\text{box}}, \quad (39)$$

$$\Delta t_{\text{box}} = \Delta r_{\text{box}}/|\vec{v}_{\text{box}}| = 2\Delta r_{\text{box}}(\gamma D)^{-1}. \quad (40)$$

Initial particle velocity \vec{v}_{box} is set to equal fluid radial stretching velocity at cylinder surface. Initial positions of the new particles are generated on the grid with number density n and randomized with homogeneous spatial distribution, so the probability of having a particle in an arbitrary i -th box is the same for all the boxes and equals N_i . New particles are placed in the shell at time intervals of equal duration Δt_{box} . The initiation of new particles is designed in such a manner to somehow connect the vortex domain with an external environment where the concentration of particles is assumed to be n as well.

Tu moze jeszcze bedzie fragment o tym jak sie zmienia liczba czastek w czasie w roznych symulacjach.

Droplet number concentration within the domain is almost constant and the pattern does not change. After a few seconds, each simulation becomes steady.

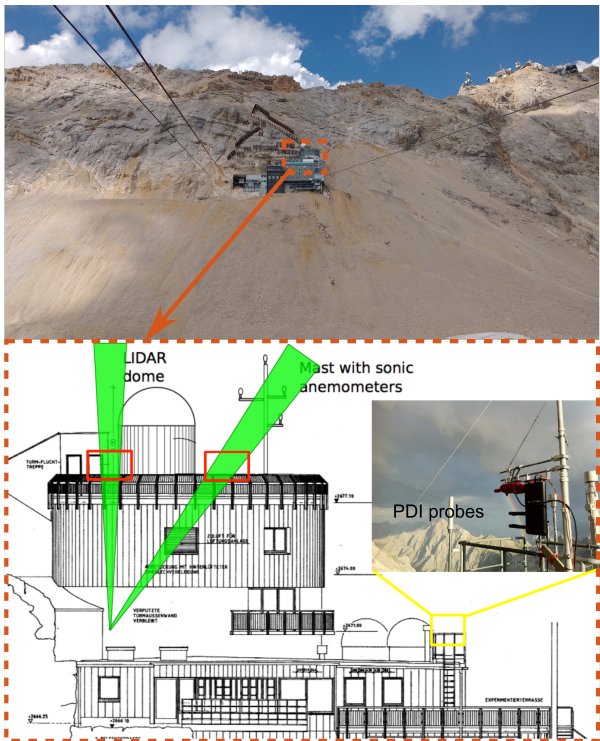


Figure 11: Upper part of the figure presents an image of UFS observatory on the slope of Zugspitze. Lower part shows the arrangement of instruments at the UFS roof.

2.4 CLOUD VOIDS OBSERVATION

Observations of the already mentioned cloud structures called cloud voids were performed with the use of lasersheet photography technique. They were accompanied by simultaneous measurement of turbulence and cloud droplet properties. The details of the lasersheet technique and turbulence methods are outlined below in subsequent subsections.

Observations were performed on 27 and 29 August 2011 at Umweltforschungsstation Schneefernerhaus (UFS) on the slopes of Zugspitze in the German Alps. Each time, the cloud event lasted for several hours. Figure 11 presents the measurement setup on UFS roof. For a detailed description of the observatory and characterization of the usual cloud and turbulence conditions on site, see Risius et al. [102] and Siebert et al. [113]. Authors of these papers showed that turbulence and cloud microphysical properties at the measurement site are quite reasonable representations of measurements made in “free” clouds away from the surface.

2.4.1 Atmospheric turbulence measurements

High-resolution measurements of small-scale turbulence during cloud void events were performed by 3D ultrasonic anemometers operated at 10 Hz, providing digital outputs for three components of wind velocity $\vec{u} = (u, v, w)$, where u and v are horizontal components and w is vertical velocity. Having 3D velocity, the mean wind velocity and its fluctuations are estimated in appropriately selected time intervals (also by running average). The time series is treated as spatial series on the basis of Taylor's frozen-flow hypothesis. Velocity fluctuations' 2nd order structure functions are calculated. The Kolmogorov "2/3 law" formulated for the structure functions (Eq. 9) determines mean energy dissipation rate $\langle \epsilon \rangle$ and further the Kolmogorov spatial scale $\langle \eta \rangle$.

Droplet size distribution was measured by a phase Doppler interferometer (PDI) probe mounted approximately 6 m down from the cloud voids observation point. The principle of the device is based on heterodyne detection of Doppler-shifted light from individual droplets, that results in a robust measurement of the droplet diameter and a single component of the droplet velocity vector [35].

Relative humidity and temperature measurements were conducted on-site as well. Relative humidity during cloud immersion was around 100%. More on cloud microphysical properties measurements can be found in Siebert et al. [113].

2.4.2 Lasersheet photography technique

In lasersheet photography particles are illuminated by a sheet of laser light. A camera placed at a certain angle to this plane collects images of the light scattered by the particles. In general, particle image recorded by the camera depends on the incoming light, the mutual position of the light sheet and the camera sensor, sensor properties and the nature of scattering process itself. Firstly, the light incident on the particle is characterized by its spectrum and spatial structure of the incident beam, what depends on the particle position with respect to width, length and divergence of laser sheet. Secondly, the camera sensor pixel responds with a signal registration only if it receives an amount of energy exceeding a certain threshold. The amount of light received by the camera depends on aperture and exposure time. Light scattered by a particle passes through the optics and undergoes some transformations, specific to a camera. What is more, the particle image on the sensor is characterized by the internal intensity distribution (diffraction pattern). All this influences single pixel signal intensity. Image size depends on particle size, optics' magnification, position with respect to the focus and other factors[89]. Thirdly, the

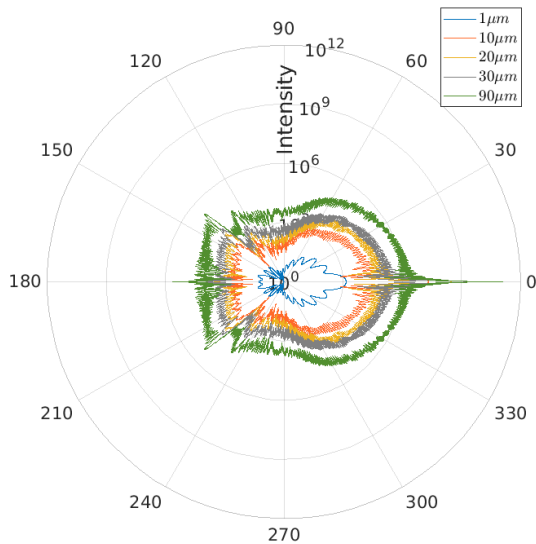


Figure 12: Relative intensity of scattered light (on radial axis, in logarithmic scale) on scattering angle and sphere radius according to Mie scattering theory.

scattered light intensity at an arbitrary angle depends nonlinearly on particle size when comes to light scattering on cloud-like particles. A larger particle can give a lower scattered intensity than a smaller one, or there may be several orders of magnitude difference in intensity between particles differing by one order of magnitude in size. The scattering theory applied for cloud droplets and visible light is called Mie theory and is summarised next.

The Mie scattering theory is a rigorous mathematical theory describing the problem of elastic scattering of light by a dielectric sphere of arbitrary size and homogeneous refractive index in the case in which a sphere size is similar to or larger than the wavelength of the incident light. It shows a complex angular and particle size dependency of the scattered light intensity (van de Hulst, 1957). Figure 12 presents this dependency for chosen parameter ranges. Thus, brightness of images of laser light scattered by polydisperse set of droplets is not expected to be monotonic with the particle size.

In cloud void observations in 2011 clouds were illuminated by a laser sheet created with a frequency-doubled high-power Nd:YAG laser (532 nm, 45 W). The sheet was set either vertical or oblique with respect to gravity. The angle between the laser sheet plane and camera recording plane in the oblique case was chosen to increase the scattering intensity on droplets and falls within the range of 30–40 deg. The laser sheet in the observation region was around 50 cm wide and 1 cm thick. Images covering the approximately 2 m long section of the sheet at a distance approximately 10 m from the source were taken

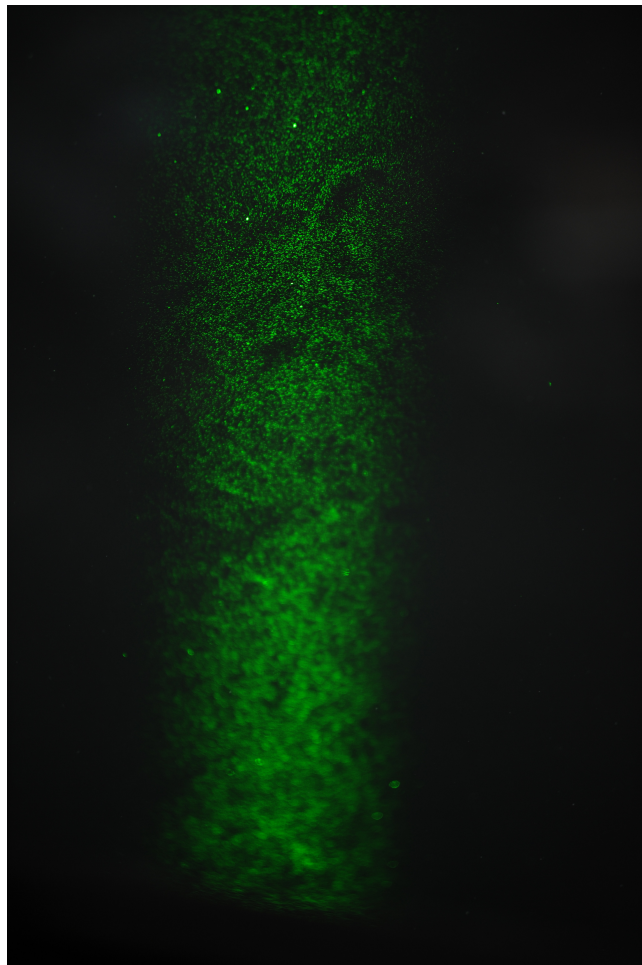


Figure 13: Image of mountain-top cloud particles, illuminated by a laser sheet light (Nd:YAG laser, 532 nm, 45 W), taken at 8:24 AM on 27th of August 2011 by Markus Neumann. Exposure time: 1/3200 s, focal length: 200 mm, f/2.8.

with a Nikon D3s 12 MP DSLR camera. Figure 13 shows an example of an unprocessed image.

2.4.3 *Experimental particle imaging vs. numerical simulations*

The setting of the measurement system does not allow to evaluate precisely the influence of the laser-sheet geometry on droplet imaging in and around cloud voids. However in order to compare measurements with the results of the numerical simulations, a simplified procedure of droplet size scaling and color scaling, including the effects of laser imaging technique, is proposed. For this purpose, the following assumptions are made:

- one particle image is recorded by one pixel,

- the signal received by a pixel changes linearly with incident light intensity only,
- each particle is in focus and its image size depends linearly on the particle size,
- the experiment in clouds was set up to allow best visualization of maximal number of particles possible.

Calculation of the Mie scattering intensity is performed with the help of an algorithm that was described in Bohren and Huffman [24]. The scattering angle corresponds to 40 deg. In the size range of cloud particles, the light intensity has a general growing tendency, but it is still strongly nonlinear. There are 3 orders of magnitude difference between particles of 1 and 30 μm radius. Relative intensity is calculated on this basis. Next, the brightness scaling is made. It assumes that experiment was set up to enable visualization of 95 % of particle size spectrum. The particle size at which the cumulant of the particle size distribution reaches 95 % was calculated. Particles larger than this size have brightness equal to 1 in the simulation visualisations. Brightness for the other particles scales linearly with relative scattered light intensity. To mimic camera sensitivity, there is a threshold below which particles get brightness equal to 0. In the plot with white background, the relation is opposite, so the brightest particles are black, and the least bright are white. This color scaling is used in Chapter [Chapter 4](#) for numerical simulation plots and calculations.

Dwa zdania o próbie z ramka światła (opcjonalnie).

2.5 CLOUD-LIKE CONDITIONS

In order to draw conclusions from the analytical and numerical models, that are meaningful from cloud turbulence point of view, it is necessary to determine cloud particle and vortex parameter space. In this case, cloud particle and turbulence data is needed to indicate what is further called "cloud-like" conditions. However simultaneous measurements of cloud droplet microphysics and turbulence properties, as stated before, are scarce. Here, some data collected in various clouds during different experiments are presented. Table 2 contains basic variables, such as mean TKE dissipation rate $\langle \epsilon \rangle$, η calculated with the use of mean dissipation rate, Tylor microscale Reynolds number Re_λ (calculated according to Eq.6), droplet radius range R , mean droplet radius $\langle R \rangle$ and mean concentration. It is important to remember that mean values estimations may significantly differ between papers. Fig.[14](#) presents in addition the Stokes number St and settling parameter S_v space corresponding to some data in Table 2.

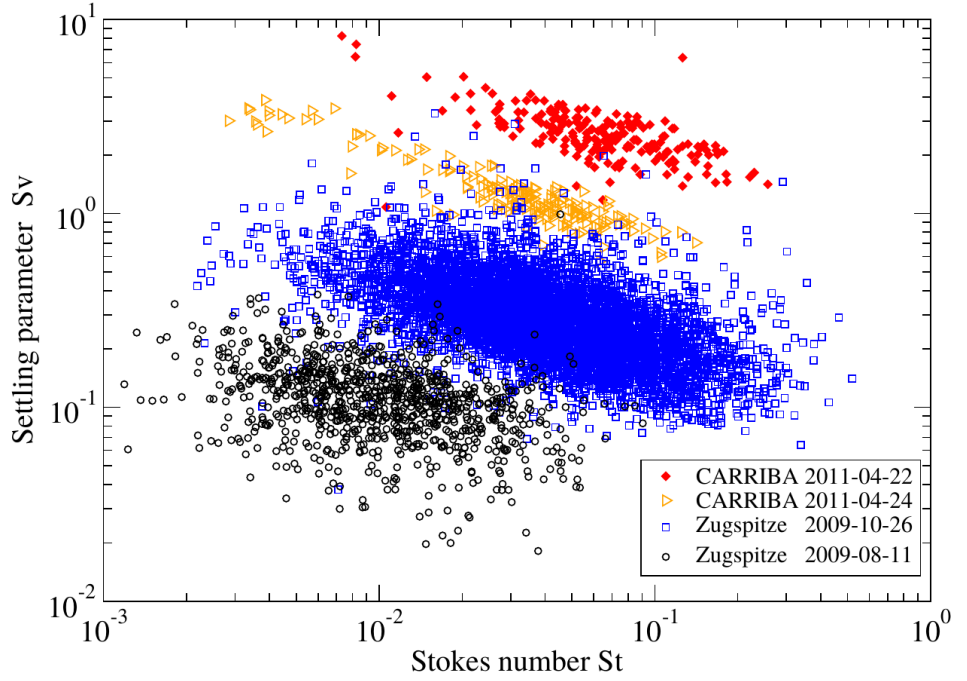


Figure 14: Stokes number St and settling parameter S_v space. Each point is based on a 1 s average of cloud data. The CARRIBA data represent typical conditions for clean (red) and slightly more polluted (yellow) cases and provide a reference for typical trade wind cumuli (see [115] for more details). Reprinted from [113].

Table 1: Cloud and turbulence basic data collected in different experiments: at UFS on Zugspitze mountain in Cu and Sc, during POST campaign in Sc, in CARRIBA campaign in Cu.

	unit	UFS, Zugspitze [113]			POST[59]		CARRIBA[115]	
clouds	-	no clouds	small Cu ^c , thin Sc ^c	Sc ^c	Sc ^m TISL	Sc ^m CTMSL	shallow Cu ^m	
$\langle \epsilon \rangle$	$\text{m}^2 \text{s}^{-3}$	$8.5 \cdot 10^{-2}$	10^{-1}	10^{-1}	$0.07 - 0.32 \cdot 10^{-3}$	$0.38 - 1.46 \cdot 10^{-3}$	$2 \cdot 10^{-3}$	$3 \cdot 10^{-3}$
η	mm	0.4	-	-	$2.39 - 3.32$	$1.24 - 1.78$	-	-
Re_λ	-	6200	-	-	-	-	-	-
R	μm	-	$2.5 \cdot 10$	$3 \cdot 17$	-	-	$4 \cdot 47$	$4 \cdot 45$
$\langle R \rangle$	μm	-	4.45	6.45	-	-	19	13.5
$\langle n \rangle$	cm^{-3}	-	532	275	-	-	42	80

The data provided are now used to select interesting parameter ranges for further analysis. Kolmogorov spatial scale is assumed to have a value around $\eta = 0.5$ mm, which is characteristic for Zugspitze measurements without and with clouds (described later in the text). The studies cited in 2.1 indicate, that it is reasonable to assume the ratio between delta and η to fall within the range $m \in [2, 20]$. Then $\delta \in$

[0.1, 1] cm. Cloud droplets are assumed to have radius $R \in [1, 25]$ μm . The maximal ratio between droplet radius and vortex radius is then $R/\delta \approx 2.5 \cdot 10^{-3}$ and the cloud droplets certainly fulfill the assumption of small particle. Paper by Belin et al. [15] mentions presence of vortices of strain value in the range $[2.5 - 5] \cdot 10^{-3}$, however at this point I would not like to narrow it down to values obtained in such a low Re_λ single case.

Part II

RESULTS

Tu znajdzie sie kilka zdan opisu, co mozna znalezc w poszczegolnych rozdzialach wynikowych pracy.

3

CHARACTERISTICS OF SINGLE PARTICLE MOTION IN A BURGERS VORTEX

This chapter addresses the dynamics of the system, which is the particle moving in a Burgers vortex, defined by the set of differential equations (Eq. 29-31 and its dimensional counterpart). The system differs significantly depending on gravity presence. First, with the use of dynamical system formalism, the system is stratified into its orbits and dynamics of these orbits is determined. Second, particular emphasis is placed on describing the characteristic time scales of the motion and their mutual relations. These tasks are performed with the hope of finding a measure of spatial pattern formation efficiency in relation to the model parameters.

It was stated before, that the equation describing particle motion along the vortex axis (Eq. 31) is independent from the ones describing motion in 2D space (Eq. 29-30). Thus in this chapter they are analysed in separate sections.

3.1 MOTION ALONG THE VORTEX AXIS

Particle motion along the vortex axis is determined by stretching outflow drag and gravity force only. As a consequence, the particle position along axis shows an exponential dependence on time, which is explained below.

In this dimension, every particle has one equilibrium point z_b , so according to the definition in Sec. 2.2 a point in which $\ddot{z} = 0$, $\dot{z} = 0$. Its dimensional and dimensionless relation to system parameters:

$$z_b^+ = S_v A^{-1} \cot \theta \quad (41)$$

$$z_b = z_b^+ \delta = v^{-1} g \delta^2 \tau_p \cos \theta \propto R^2 \quad (42)$$

Gravity force and stretching can balance only if z is positive, so $z_b > 0$. It is a source, so a kind of an unstable equilibrium. Position z_b with respect to vortex core size δ and particle radius R for cloud-like conditions, is plotted in Fig. 15.

Eq. ?? can be integrated with arbitrary constants C_1 and C_2 leading to the following general solution:

$$z^+(t) = C_1 \exp \lambda_1 t^+ + C_2 \exp \lambda_2 t^+ + z_b^+ \quad (43)$$

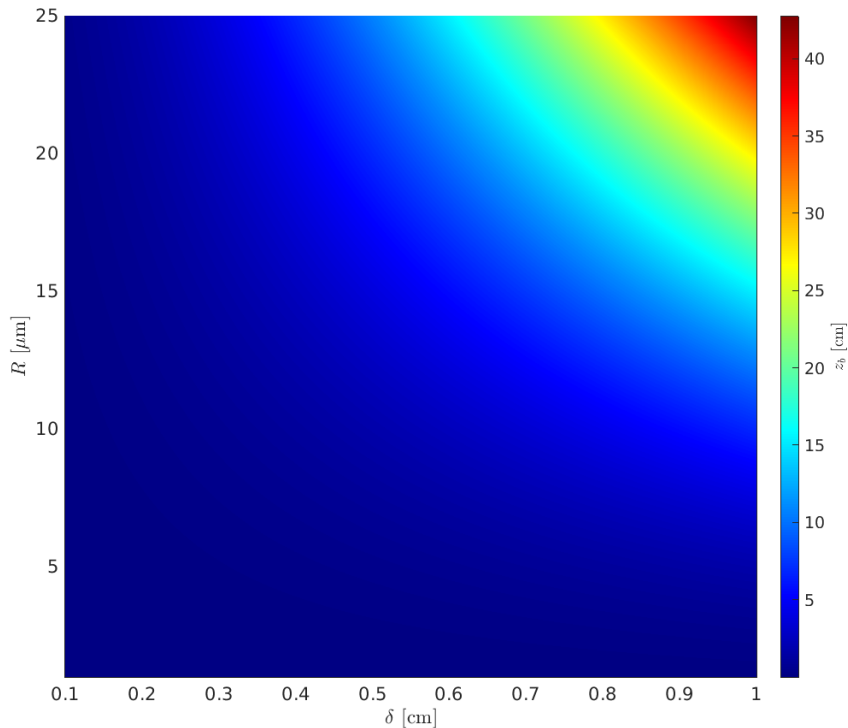


Figure 15: Equilibrium position z_b versus vortex core size δ and particle radius R for $\theta = \pi/2$. Plot variables' ranges correspond to cloud-like conditions.

so $z^+(t)$ indeed depends exponentially on time. By setting the initial conditions to $z^+(0) = z_0^+$, $\dot{z}(0) = w_0$ one obtains the following specific solution:

$$\frac{z^+(t^+) - z_b^+}{z_0^+ - z_b^+} = \frac{1}{\lambda_1 - \lambda_2} \left[\lambda_1 \exp \lambda_2 t^+ - \lambda_2 \exp \lambda_1 t^+ + \frac{w_0^+}{z_0^+ - z_b^+} (\exp \lambda_1 t^+ - \exp \lambda_2 t^+) \right] \quad (44)$$

$$\lambda_{1/2} = \left(\mp \sqrt{1 + 4 A S t} - 1 \right) / 2 S t \quad (45)$$

This equation describes particle motion along the axis, by expressing the evolution of particle distance from equilibrium point with respect to its initial distance from the equilibrium point. In order to give a sense of this solution, it was rewritten using the newly defined dimensionless k parameter:

$$k = (1 + 4 A S t)^{-\frac{1}{2}} = (1 + 2 \tau_p \gamma)^{-\frac{1}{2}} \quad (46)$$

where $k \in (0, 1)$, and dimensionalized:

$$\frac{z(t) - z_b}{z_0 - z_b} = \left[\frac{1}{2} (1 - k) - k \frac{\tau_p w_0}{z_0 - z_b} \right] e^{\frac{-t}{2\tau_p} (k^{-1} + 1)} + \left[\frac{1}{2} (1 + k) + k \frac{\tau_p w_0}{z_0 - z_b} \right] e^{\frac{-t}{2\tau_p} (k^{-1} - 1)}. \quad (47)$$

One can see that the first term in 47 is leading for small times, especially when the initial velocity is nonzero. In longer times the second term is a leading term.

As has already been argued in the introduction, the Burgers vortex is a good approximation for a relatively long-lasting vortex only locally in turbulent flow. Therefore, the motion of particles in a vortex which has finite size and lifetime should be considered. For this reason further discussion of particle motion along the axis is devoted to the estimation of what is here defined as *exit time* τ_{ex} : the time at which a particle starting at position $z(t=0) = z_0$, with zero initial velocity $\dot{z}(t=0) = 0$, reaches an arbitrary finite domain border $\pm Z$.

exit time

First, the Eq. 47 for the initial velocity set to zero, $w_0 = 0$, simplifies to:

$$\frac{z(t) - z_b}{z_0 - z_b} = \frac{1}{2} (1 - k) e^{\frac{-t}{2\tau_p} (k^{-1} + 1)} + \frac{1}{2} (1 + k) e^{\frac{-t}{2\tau_p} (k^{-1} - 1)} \quad (48)$$

In this case, the direction of motion depends on the relative position of z_0 and z_b only. This thesis assumes that particles are significantly smaller than vortex size: $R \ll \delta$, and thus $\tau_p \gamma \ll 1$. In large times $t \gg \tau_p$ this assumption allows to approximate Eq.48 to:

$$\frac{z(t) - z_b}{z_0 - z_b} = e^{\frac{t}{\tau_p}} \quad (49)$$

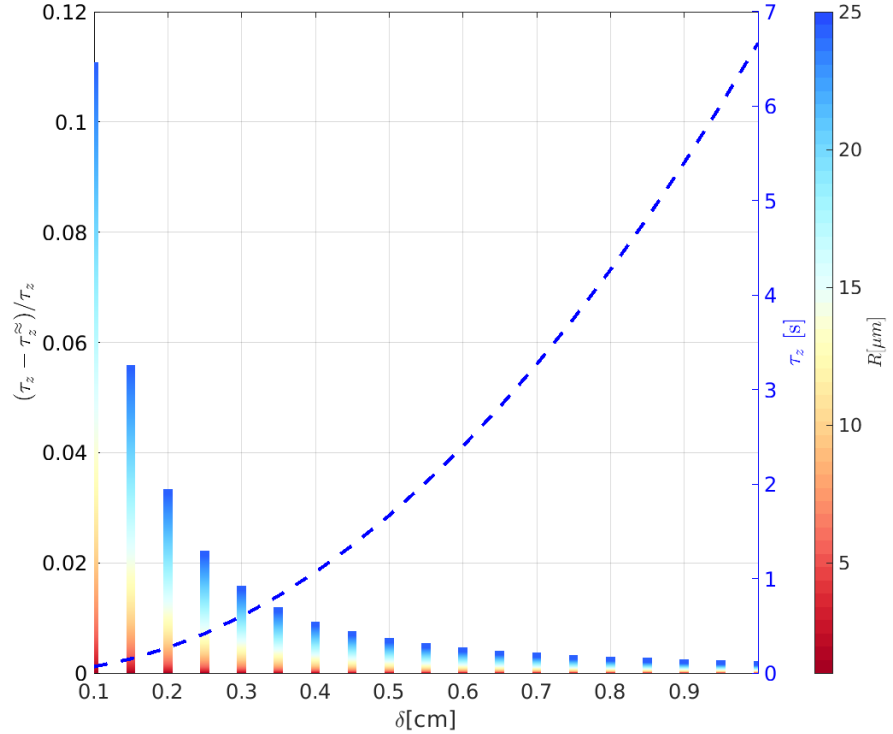


Figure 16: Characteristic time of the motion along vortex axis τ_z (green line, right y-axis) versus vortex core size δ and its relative error (left y-axis, bar chart) versus δ and particle radius R . Colorscale indicates dependence on R . Plot variables' ranges correspond to cloud-like conditions.

where τ_z is the characteristic time of the motion along vortex axis:

$$\tau_z = \frac{2}{k^{-1} - 1} \tau_p = \frac{2}{\sqrt{1 + 2\tau_p \gamma} - 1} \tau_p \quad (50)$$

According to small particles assumption, τ_z can be approximated as well:

$$\tau_z \approx \frac{2\tau_p}{1 + 2\tau_p \gamma / 2 - 1} = 2\gamma^{-1} = v^{-1}\delta^2. \quad (51)$$

Figure 16 presents τ_z relative error (accurate value from Eq.50 minus approximated value from Eq.51 divided by the accurate value) with respect to δ (on X-axis) and R (color). We see that for cloud-like variables' ranges the approximation is fully justified. What is interesting is that the approximated τ_z does not depend on particle size, so it is the same for all the particles in polydisperse dispersion. It is also easy to notice that in cloud-like conditions particle response time is always significantly smaller than characteristic time of motion along axis $\tau_z \gg \tau_p$. For example when the vortex core size δ is 1 cm, then τ_z is approximately 6.7 s, and for 0.5cm it is approximately 1.6 s.

The simplified equation of motion, Eq.ch3:eq12, must be solved in order to estimate the exit time:

$$\frac{\text{sign}(z_0 - z_b)Z - z_b}{z_0 - z_b} = e^{\frac{\tau_{ex}}{\tau_z}} \quad (52)$$

so there is:

$$\tau_{ex} = \tau_z \log \left(\frac{\text{sign}(z_0 - z_b)Z - z_b}{z_0 - z_b} \right) \quad (53)$$

The function under the logarithm is denoted as $L(Z, z_0; z_b)$ and further:

$$L(Z, z_0; z_b) = \frac{Z - \text{sign}(z_0 - z_b)z_b}{|z_0 - z_b|} = \frac{Z/z_b - \text{sign}(z_0 - z_b)}{|z_0/z_b - 1|} = \frac{\overbrace{Z/z_b}^{Z^*} - \text{sign}(z_0/z_b - 1)}{\underbrace{|z_0/z_b - 1|}_{z_0^*}}. \quad (54)$$

Then the estimated exit time:

$$\tau_{ex}(Z^*, z_0^*; \tau_z) \approx \tau_z \log(L(Z^*, z_0^*)) \quad (55)$$

$$L(Z^*, z_0^*) = \frac{Z^* - \text{sign}(z_0^* - 1)}{|z_0^* - 1|} \quad (56)$$

$$(57)$$

where $Z^* \in (1, \infty)$, $z_0^* \in [-Z^*, 1] \cup (1, Z^*]$. For $z_0^* = 1$ (when $z_0 = z_b$) the estimation gives $\tau_{ex} = \infty$, so it agrees with the fact, that z_b is an unstable equilibrium point.

The logarithmic factor in τ_{ex} is depicted in Fig. 17. It depends on domain half-length Z and initial position z_0 ratios to z_b . It is hard to draw any direct conclusions for single particle exit time on the basis of Fig.17 alone. However there is an interesting feature when thinking about the collection of particles in the vortex. Namely, the mean value of logarithmic factor over z_0^* (over all initial positions) equals one for every Z^* (for every vortex half-length):

$$\langle \log L(Z^*, z_0^*) \rangle_{z_0^*} = \frac{1}{2Z^*} \int_{-Z^*}^{Z^*} \log L(Z^*, z_0^*) dz_0^* = 1 \quad (58)$$

This means that independently of vortex length, when dealing with uniformly distributed set of particles, the logarithmic factor does not have influence on mean exit time.

3.2 MOTION IN THE PLANE PERPENDICULAR TO VORTEX AXIS

The trajectories determined in 2D space by Eq.29-31 have several different attractors. The exact choice depends on the system parameters. Presence of gravity force distinguishes two basic cases. There are presented below.

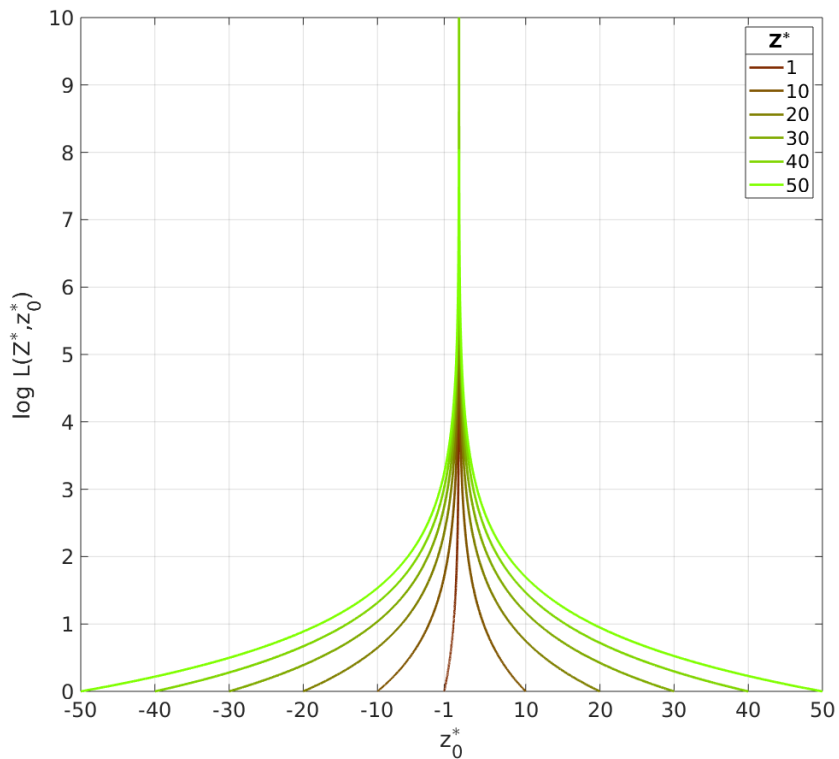


Figure 17: Logarithmic factor $\log L$ (in τ_{ex}) vs. z_0^* - ratio of initial position and equilibrium position. Line color is scaled by Z^* values which refer to different ratios of vortex half-length and equilibrium position.

3.2.1 Without gravity (vertical vortex)

The system without gravity force in 2D space is equal to the system in which gravity is parallel to the vortex axis ($\theta = 0$). It comes down to the fact that sedimentation parameter S_v is zero. In this case the nondimensional equations of motion are:

$$\begin{cases} \ddot{r^+} - r^+ \dot{\varphi}^{+2} = -St^{-1} (Ar^+ + \dot{r}^+) \\ 2\dot{r}^+ \dot{\varphi}^+ + r^+ \ddot{\varphi}^+ = St^{-1} \left(\frac{1}{2\pi r^+} (1 - e^{-\frac{r^+2}{2}}) - r^+ \dot{\varphi}^+ \right) \end{cases} . \quad (59)$$

and the system posses axial symmetry. This set of equations depends on two parameters only: St/A and St . The attractors: an equilibrium point positioned on the vortex axis $r^+ = 0$ or a circular orbit of radius r_{orb}^+ (defined later), inherit the axial symmetry. The system changes according to Hopf bifurcation scheme. Lets put $\alpha = 16\pi^2 - St/A$ as a bifurcation parameter. This translates to the fact, that if:

$$St \leq St_{\text{cr}}(A) \equiv 16\pi^2 A, \quad (60)$$

the only attractor, the equilibrium point at the axis, is a stable focus ($\alpha \leq 0$). In the opposite case $St > St_{\text{cr}}$, the equilibrium point is an unstable focus, accompanied by a stable periodic circular orbit ($\alpha > 0$). Particle trajectories around such attractors are presented schematically in Fig. [Figure 9](#). Having established the existence of attractors, their impact on particle kinematics is studied.

3.2.1.1 Stable periodic orbit

The first type of trajectory that is analysed is the particle moving on stable periodic orbit. The radius of the periodic orbit, denoted as r_{orb}^+ , satisfies the equation:

$$[1 - \exp(-r^{+2}/2)] / 2\pi r^{+2} = \sqrt{A/St}, \quad (61)$$

which depends uniquely on St/A . Fig. [18](#) presents numerical solution of this equation. For ease of reference, X-axis shows r_{orb}^{+2} and Y-axis shows $\sqrt{St/A}$. Two asymptotic limits are included as well. For small orbit radius, $r_{\text{orb}}^+ \ll 1$, it is possible to approximate left-side of Eq.[61](#) by developing Taylor series around zero and get:

$$[1 - \exp(-r^{+2}/2)] / 2\pi r^{+2} \approx \left(\frac{1}{2} - \frac{r^{+2}}{8} + O(r^{+4}) \right) / 2\pi \quad (62)$$

which then gives the relation

$$r_{\text{orb}}^{+2} \sim -16\pi\sqrt{A/St} + 4 \quad (63)$$

shown in Fig.[18](#) by curved dashed blue line. On the other side, in the limit of large orbit radius there is:

$$[1 - \exp(-r^{+2}/2)] / 2\pi r^{+2} \approx (r^{+2} - O(r^{+4})) / 2\pi \quad (64)$$

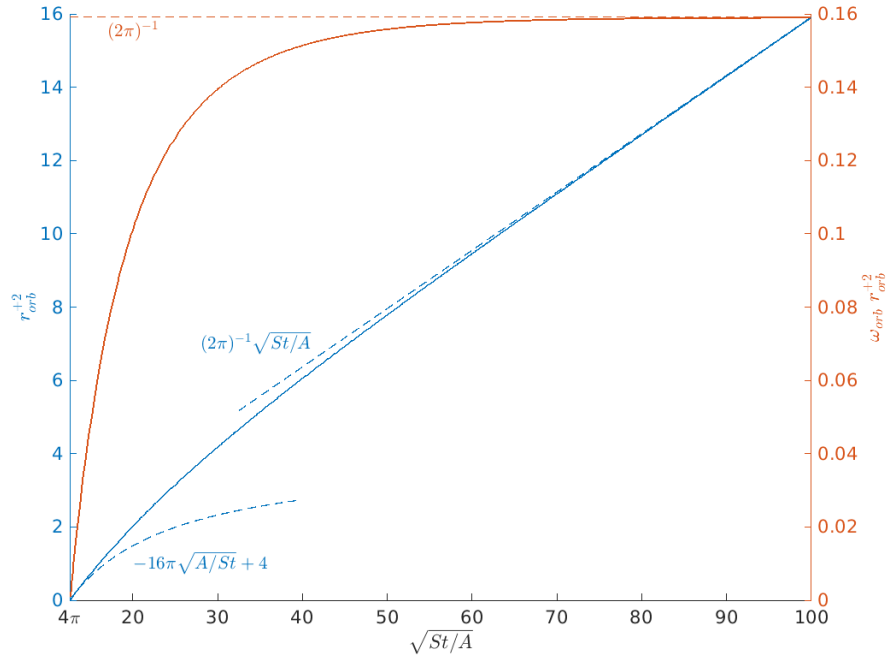


Figure 18: Particle stable periodic orbit radius r_{orb}^{+2} square (left y-axis) and orbit nondimensional angular momentum (right y-axis) with respect to parameter $\sqrt{St/A}$. Dashed lines represent asymptotic relations.

which leads to the asymptotic:

$$r_{\text{orb}}^{+2} \sim \frac{1}{2\pi} \sqrt{\frac{St}{A}} \quad (65)$$

shown in Fig.18 as straight dashed blue line. After all, r_{orb}^{+2} shows monotonic growth with $\sqrt{St/A}$.

The second conclusion based on the solution to equation 61 is that non-dimensional angular velocity at circular periodic orbit is

$$\omega_{\text{orb}}^+ = \sqrt{A/St}, \quad (66)$$

or in other words, particle rotation time is $\tau_{\text{orb}}^+ = \sqrt{St/A}$. What is interesting, is that the orbit angular velocity is equal to fluid angular velocity:

$$\omega_{\text{orb}}^+ = u_\phi^+(r_{\text{orb}}^+)/r_{\text{orb}}^+. \quad (67)$$

so particle circling on its orbit has zero relative velocity with respect to the fluid. What is more, particle angular momentum $\omega^+ r^{+2}$ on circular orbit (orange line plot in Fig. 18, right Y-axis) in large radius limit is approximately constant in time and independent of particle size, equal to $(2\pi)^{-1}$.

$\sqrt{St/A}$ solely determines orbit stratification in 2D space in no-gravity

case and the circular periodic orbit dynamics. It is then important to investigate its connection to dimensional system parameters:

$$\sqrt{\frac{St}{A}} = \sqrt{\frac{2\rho_p}{9\rho_a} \frac{R}{A\delta}} \quad (68)$$

Periodic orbit (non)existence condition from Eq.60 is reformulated to:

$$R \geq R_{cr}(A, \delta) \equiv 4\pi \sqrt{\frac{9\rho_a}{2\rho_p}} \delta A \approx 0.84\delta A, \quad (69)$$

or alternatively:

$$A \leq A_{max}(R, \delta) \equiv \sqrt{\frac{2\rho_p}{9\rho_a} \frac{R}{4\pi\delta}} \approx 1.2 \frac{R}{\delta} \quad (70)$$

so the maximal (critical) strain parameter value A_{max} (A_{cr} is designated to another bifurcation process here) in cloud-like conditions is of the order of the droplet radius to vortex radius ratio. Dimensional periodic orbit is $r_{orb} = r_{orb}^+ \delta$, so the solution obviously depends on $\sqrt{St/A}$ parameter only and then is scaled by vortex core size δ .

The numerical solution presented in Fig.18 is now shown in the Fig. 19 in dimensional form, where vortex core size is chosen arbitrarily: $\delta = 0.5$ cm. In this parameters' range, the particle orbit radius is of the order of vortex core size. One can see, that in the large orbit limit, from Eq.65 there is:

$$r_{orb} \propto \sqrt{R\delta A^{-1}} \quad (71)$$

It is interesting to notice that the dimensional angular velocity ω_{orb} is independent of A . It is in fact inversely proportional to particle radius R and vortex core size δ :

$$\omega_{orb} = \sqrt{A/St} \tau_f^{-1} = \sqrt{9\rho_a/2\rho_p} (R\delta)^{-1} \propto (R\delta)^{-1}. \quad (72)$$

Angular velocity on periodic orbit does not depend on A , but its existence does. Fig.20 presents cloud-like values of angular velocity ω_{orb} . The existence condition is presented in Fig.20 by $R = R_{cr}(A)$ plots. For a given A periodic orbits exist in $R > R_{cr}(A)$ area.

Particle rotation time being an inverse of angular velocity is proportional to vortex core radius and particle radius:

$$\tau_{orb} = \sqrt{\nu^{-1} \tau_p} \delta = \sqrt{2\tau_p \gamma^{-1}} \propto R\delta. \quad (73)$$

The previously established assumption of small particles i.e. $\tau_p \ll \gamma^{-1}$ leads to the conclusion that $\tau_{orb} \ll \gamma^{-1}$ as well. More on the timescales of motion can be found later in the text.

Having identified system attractors and their basic features, their realistic impact on particle kinematic is studied. The probability that a

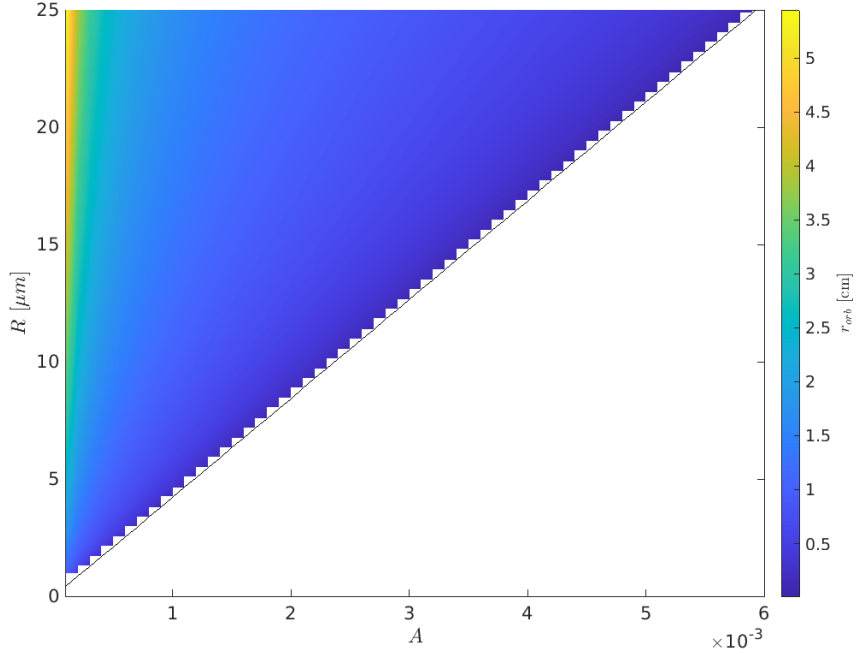


Figure 19: Particle stable orbit radius r_{orb} dependence on particle radius R and vortex strain parameter A for cloud-like parameter ranges and vortex core size $\delta = 0.5$ cm. Black line represents critical parameter value as for stable orbit existence.

particle founds itself in phase space exactly in the equilibrium point or on periodic orbit is low. More probable is that it is positioned somewhere else and is pulled towards its attractor/s. That fact is the motivation for the detailed study of particles approaching their attractors conducted below.

3.2.1.2 Stable focus or stable periodic orbit attraction

I analyze the scales of motion and features of the particle trajectory starting at arbitrary position and approaching its attractor (stable focus at the axis or circular orbit). For the sake of simplicity, the starting radial positions selected for analysis are the only spatial scales distinguished in the equations. That means: the position at the axis $r^+(0) = 0$ and at $r^+(0) = r_s$. The motion of a particle defined in this way is called here a "docking process". Time at which the docking process occurs is consequently called docking time and noted t_{doc}^+ . In short, for the purposes of further analysis, I distinguish two types of processes:

- in-orbit docking: $r^+(0) = 0$, $\dot{r}^+(0) = u_r^+(0)$, particle is attracted by its periodic orbit r_{orb}^+

docking process

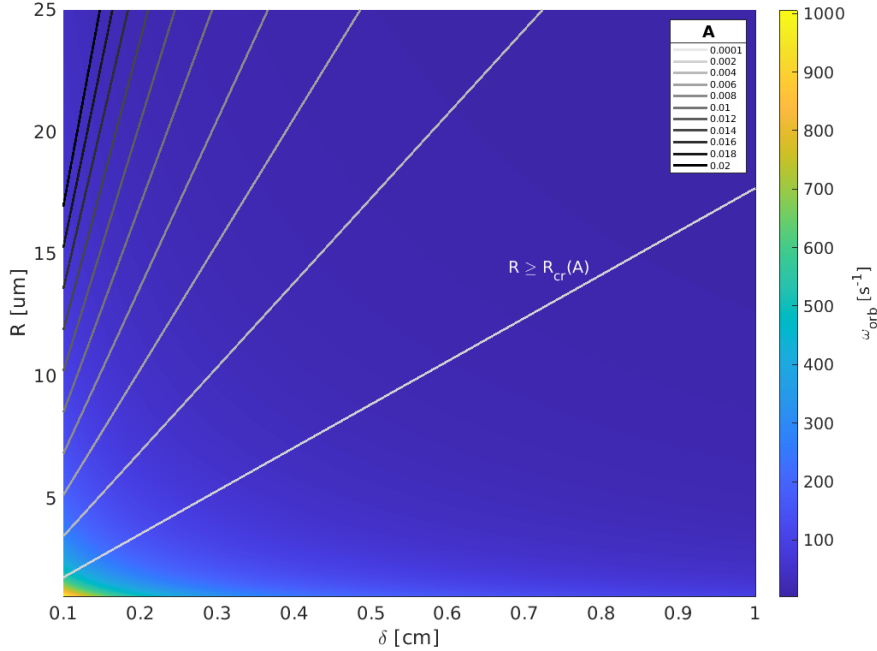


Figure 20: Particle stable orbit angular velocity ω_{orb} dependence on particle radius R and vortex core radius δ for cloud-like parameter ranges. Parameter domain above the line corresponding to an arbitrary A value is the domain in which stable periodic orbit exists.

Table 3: Initial ($t^+ = 0$) and final ($t^+ = t_{\text{doc}}^+$) particle state in numerical simulations of docking processes. σ is an arbitrary small parameter.

docking	$r^+(0)$	$\dot{r}^+(0)$	$r^+(t_{\text{doc}}^+)$
in-orbit	σ	$u_r^+(\sigma)$	$r_{\text{orb}}^+ - \sigma$
axis	$r_s - \sigma$	$u_r^+(r_s - \sigma)$	σ

- axis docking: $r^+(0) = r_s$, $\dot{r}^+(0) = u_r^+(r_s)$ particle is attracted by a point on vortex axis $r^+ = 0$.

Due to the fact, that the particle approaches its destined radial position asymptotically, numerical simulation of the docking process was defined between points in the phase space indicated in the Table 3.

The choice of small σ parameter will be elaborated on later.

Figure 21 and Fig. 22 show tracking particles which undergoes docking process, on axis and in-orbit respectively. Three panels show radial position, radial velocity and angular velocity of particles. Each line represents a particle with different St and A parameters. St range was chosen to be $St \in (0, 1)$ and A range was adjusted in each case. Line color corresponds to St/A value, line color intensity to different St and A representations of the same St/A value. From Fig. 21 it is hard to see any rule on parameter dependence. All the particles tend

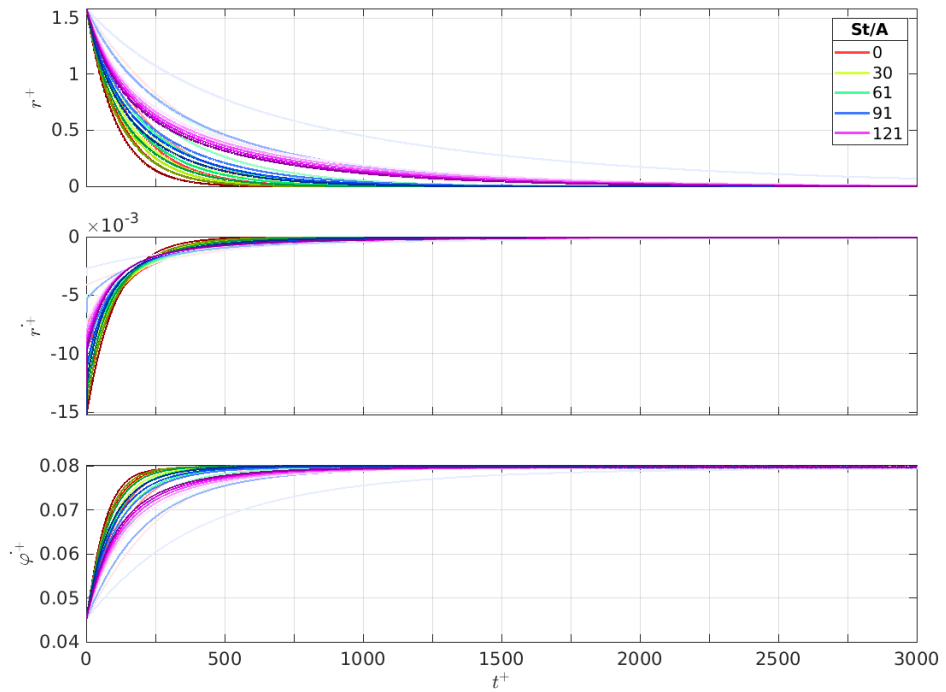


Figure 21: Tracking of a particle while docking on axis, for $\sigma = 10^{-4}$. Line color corresponds to St/A value, line color intensity to different St and A representations. Upper panel- radial coordinate, middle panel - radial velocity, lower panel - angular velocity. Plots are magnified for better visibility.

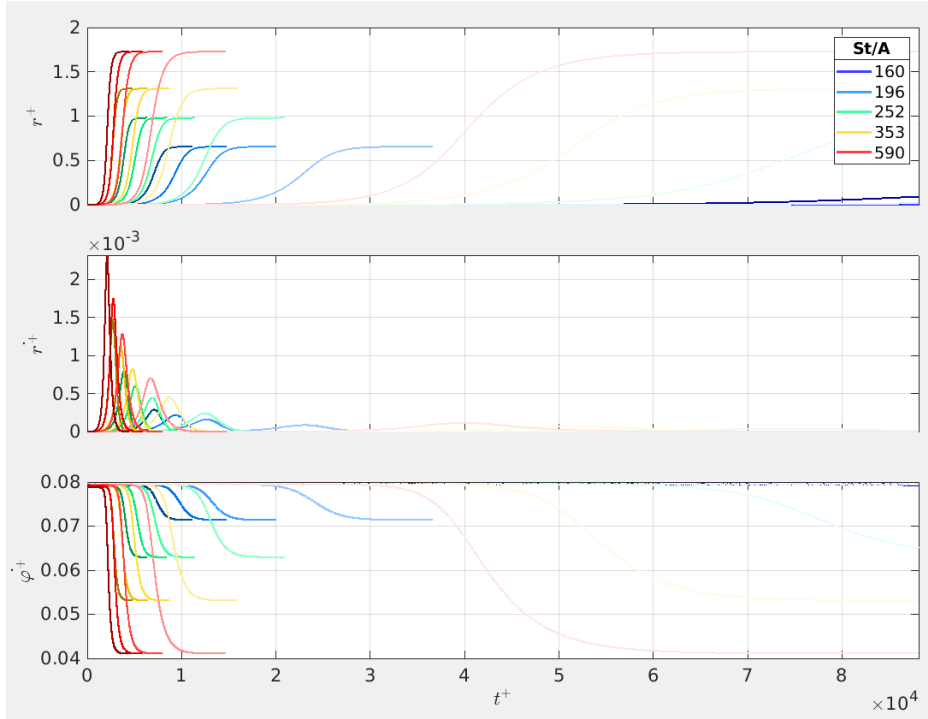


Figure 22: Tracking of a particle while docking in orbit, for $\sigma = 10^{-4}$. Line color corresponds to St/A value, line color intensity to different St and A representations. Upper panel- radial coordinate, middle panel - radial velocity, lower panel - angular velocity.

to have the same angular velocity when they dock on the axis, the radial velocity towards the axis diminish in time in a kind of exponential manner. The ratio at which it happens depends on both St and A , the same is for t_{doc}^+ . In Fig. 21 one can notice, that particles has the same angular velocity at the start and it decreases to a value determined by St/A only. The same time the radial velocity rises and falls again to zero almost symmetrically in time, when the particle reaches its orbit at r_{orb}^+ .

Figure 23 and Fig. 24 represent the same data, but rescaled. X-axis is scaled separately for each trajectory by docking time. In Fig. 23, on Y-axes, the radial velocity is scaled by the fluid velocity at the starting point $u_r(r_s)$, angular velocity is scaled by the fluid angular velocity at the final position σ , so $u_\varphi(\sigma)/\sigma$. In Fig. 24, on Y-axes, radial position is scaled by circular orbit radius, radial velocity is scaled by the opposite of fluid velocity at the starting point $-u_r(\sigma)$, angular velocity is scaled by the particle angular velocity at the circular orbit ω_{orb}^+ . By doing so, one can obtain trajectories that depend almost only on St/A parameter - lines of the same color, but different intensity, converge. The greatest difference is seen in particle angular velocity response to fluid, which is caused by different St . Fig. 24 reveals that when the particle is docking in-orbit, it first follows the fluid motion around the axis, with radial velocity close to zero. With rotational velocity,

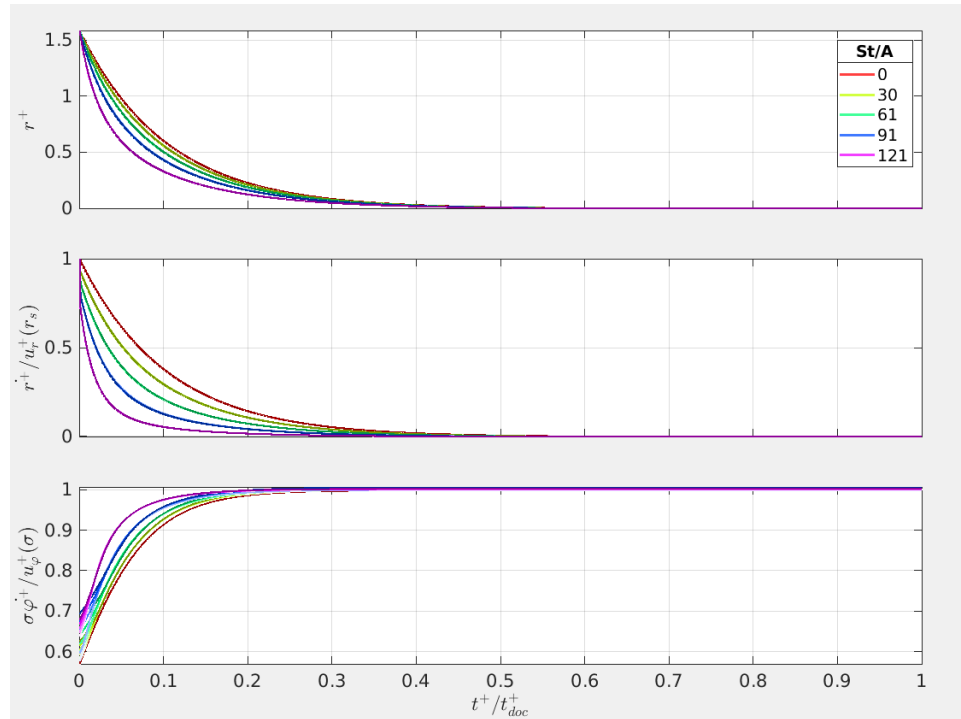


Figure 23: Same as in Fig. 21, but X-axis is scaled separately for each trajectory by a docking time. On Y-axes, the radial velocity is scaled by the fluid velocity at the starting point $u_r(r_s)$, angular velocity is scaled by the fluid angular velocity at the final position σ , so $u_\varphi(\sigma)/\sigma$.

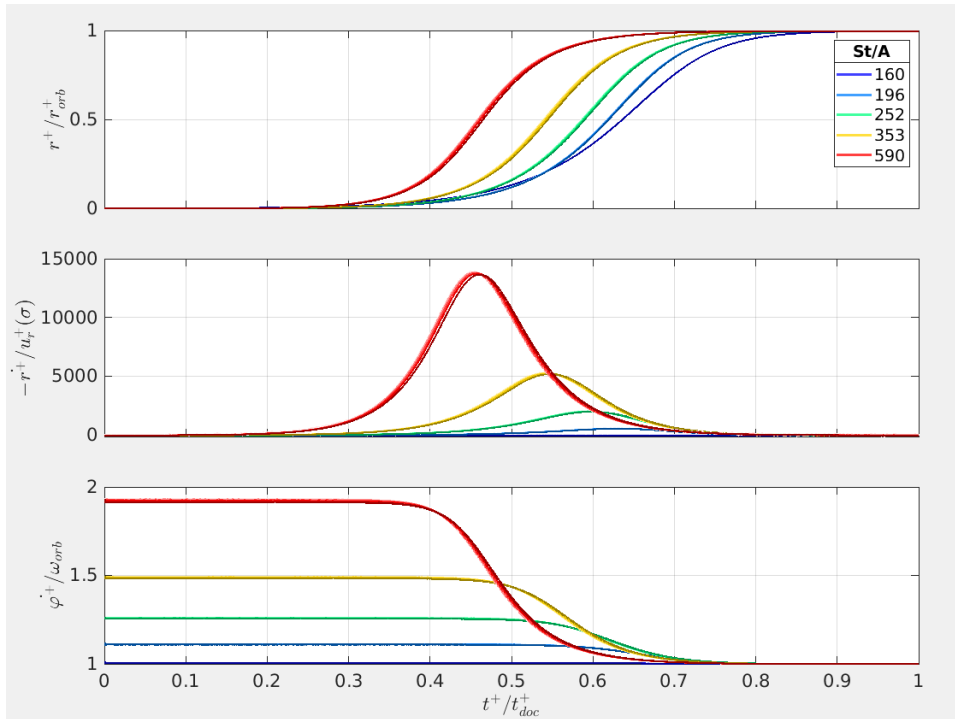


Figure 24: Same as in Fig. 22, but X-axis is scaled separately for each trajectory by docking time. On Y-axes, radial position is scaled by circular orbit radius, radial velocity is scaled by the opposite of fluid velocity at the starting point $-u_r(\sigma)$, angular velocity is scaled by the particle angular velocity at the circular orbit ω_{orb}^+ .

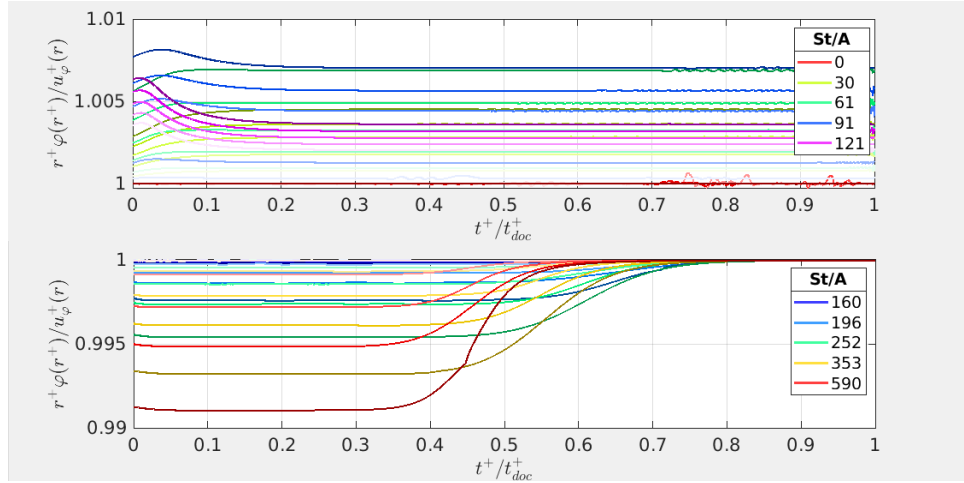


Figure 25: Angular velocity of a particle while docking at the axis (top) and in-orbit (bottom). X-axis is scaled separately for each trajectory by a docking time. On Y-axis, angular velocity is scaled by the fluid angular velocity at particle position. Line color corresponds to St/A value, line color intensity to different St and A representations.

the centrifugal force starts acting on it and causes a rapid increase in radial speed in the direction away from the vortex axis. Increasing distance from the axis in turn results in a steep decrease of the angular velocity, and further the decrease of the radial velocity. Then the particle approaches its periodic orbit: radial velocity goes to zero, rotational velocity goes to ω_{orb} . The rate of these changes depends on the parameters of the model in a complex way. The attempt to find the approximate dependence is conducted below.

There is strong time correlation between radial and angular velocity change. In fact when one looks closer at the angular velocity at the particle, it is possible to notice that it depends the most on the radial position of the particle. Figure 25 presents particle angular velocity in the docking processes, scaled by fluid angular velocity at the position of the particle. It seems that the particles, although their Stokes number can reach value of 1, when it comes to angular motion almost follow the flow from the beginning of the motion, and then asymptotically reach fluid velocity.

Unfortunately the attempt to simplify the equation of motion by assuming that particle angular velocity is equal to the fluid velocity at particle position leads to a contradiction - such an assumption could be made only in the linear vortex model. Even then the first of Eq.59 is a case of a Chini equation and in general it is not possible to solve it analytically. In-orbit docking radial velocity resembles a gaussian function and the radial position the error function (see Fig.24, but the tests proved they are not).

Now lets look closer at the axis docking process. Figures 21 and 23

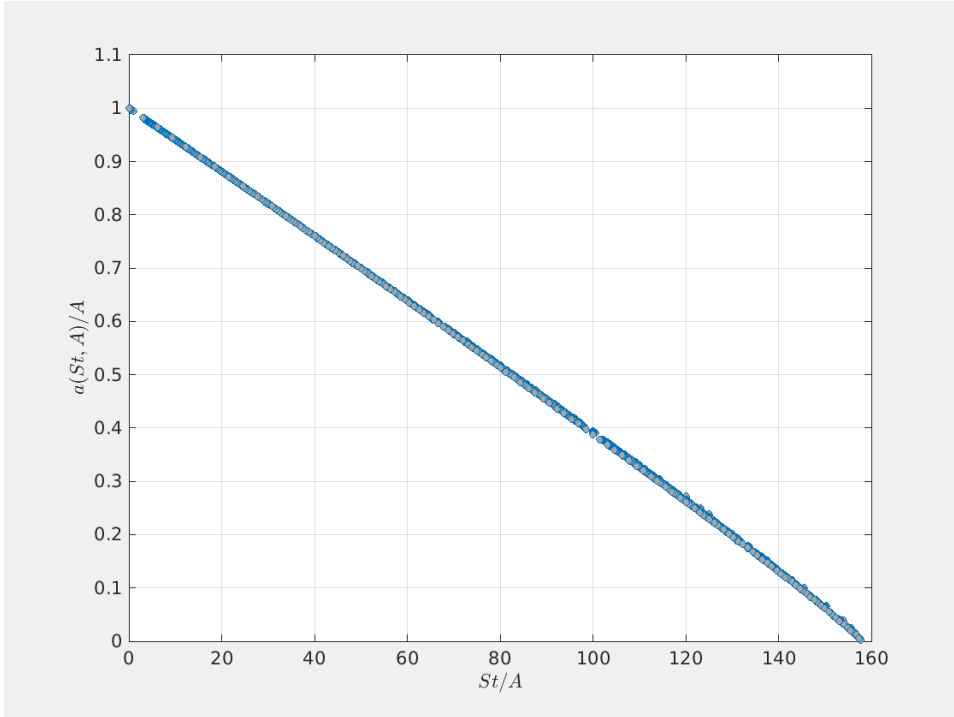


Figure 26

show that the particle firstly move with radial velocity the same as fluid's velocity: $v_r^+(r_s - \sigma)$. Next the particle radial velocity decreases rapidly in time. When the time is scaled by docking time, t^+/t_{doc}^+ , the rate of this decrease depends on St/A parameter only. Angular velocity increases towards fluid velocity close to the axis, $v_\varphi^+(\sigma)/\sigma$, when particle is approaching the axis.

The first glance at 21 and 23 leads to the observation that the radial motion (as for $r(t)$ and $\dot{r}(t)$) of the particle docking on the axis resembles exponential decay. Logarithmic plots show these clearly linear dependence in time except for small times ($t^+ \ll t_{\text{doc}}^+$). Therefore, a simplified model of this process is proposed below and an attempt is made to estimate axis docking timescale τ_{d1}^+ .

Lets assume that in the axis docking process we have:

$$r^+(t) \propto \exp \frac{-t^+}{\tau_{d1}^+} \quad (74)$$

and that $\tau_{d1}^+ = \tau_{d1}^+(St, A)$.

I performed linear fit of the function $y = -a * x + b$ on the numerical trajectories for a range of St and A , taking $y = \log r^+(t^+)$ and $x = t^+$. Figure 26 presents the directional coefficient fitted values in a way that reveals the relation with system parameters: on X-axis there

is St/A and on the Y-axis there is a_{fit}/A . It is clear that $\frac{a_{fit}}{A}$ depends only on St/A . In conclusion:

$$\frac{a_{fit}}{A} \approx \left(1 - \frac{1}{16\pi^2} \frac{St}{A}\right) \quad (75)$$

and further:

$$\tau_{d1}^+(St, A) \approx A^{-1} \left(1 - (16\pi^2)^{-1} \frac{St}{A}\right)^{-1}. \quad (76)$$

Dimensional axis docking timescale is then:

$$\tau_{d1} = \tau_{d1}^+ \tau_f = 2\gamma^{-1} \left(1 - (16\pi^2)^{-1} \frac{St}{A}\right)^{-1} \quad (77)$$

Estimated dimensional timescale τ_{d1} depends primarily on γ^{-1} . This is exactly the same as in the case of motion along vortex axis (see Eq.51).

Further the analysis of t_{doc}^+ for arbitrary parameter ranges was conducted. Figure 27 presents the results of t_{doc}^+ numerical calculation with respect to St and A . The colorscale is logarithmic. Line that consists of local maxima represents the $St = St_{cr}(A)$ boarder. For $St \approx St_{cr}(A)$ the forces working on the particle almost balance, so the docking time is very long. When approaching the critical value, it asymptotically goes to infinity. Figure 28 shows the same results, but in dimensional form. The exact values cannot be easily interpreted, but what is important is that the asymptotic behaviour described is conserved. There is also rapid growth of docking time observed in $St \rightarrow 0$ limit.

Although the docking time is defined in a twofold way, it seems to have a physical meaning: the values are of a similar order, it goes towards on the both sides of the critical value.

Since σ in theory is infinitesimally small but the numerical calculation demands finite value, the sensitivity analysis was conducted below for $\sigma = 10^{-n}$, $n = 1, 2, 3, 4, 5$. - do zrobienia jak staczy czasu.

3.2.2 With gravity (inclined vortex)

Nonparallel alignment of the gravity vector and vortex axis ($\theta \neq 0$) destroys the axial symmetry of the system and introduces the presence of other attractors, such as non-circular periodic orbit and multiple equilibrium points outside the axis.

For a nonzero θ , every particle always has equilibrium points in 2D space. Position of these points in 2D space is determined by S_v and A

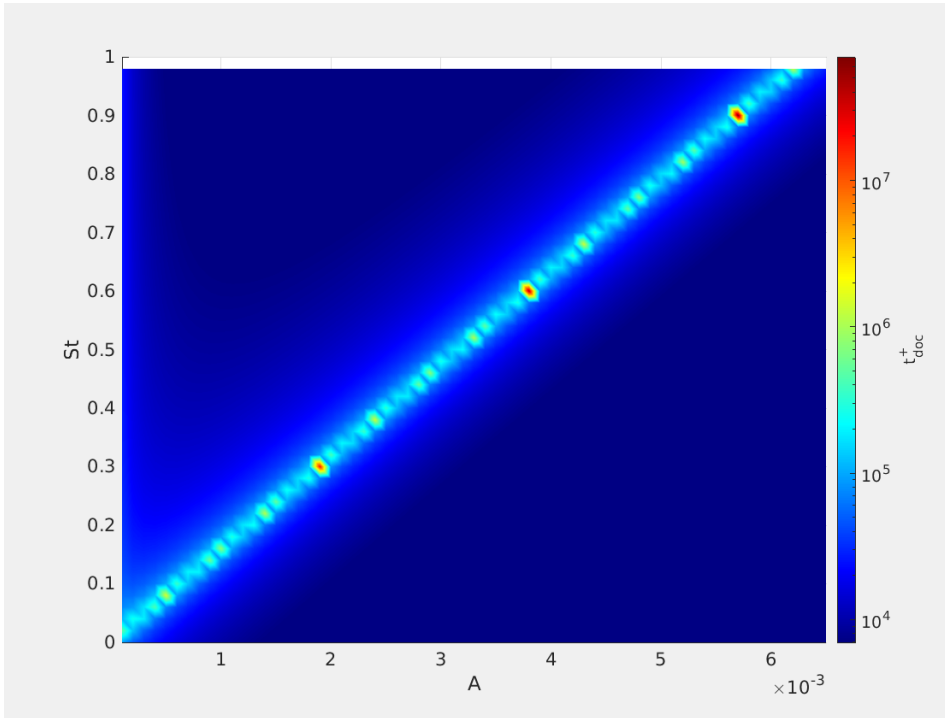


Figure 27: Nondimensional docking time calculated numerically with respect to St and A for arbitrary variable ranges with $\sigma = 10^{-5}$. Line of local maxima corresponds to $St = St_{\text{cr}}(A)$ and shows the stability border: particles to the left undergo in-orbit docking, particles to the right - axis docking.

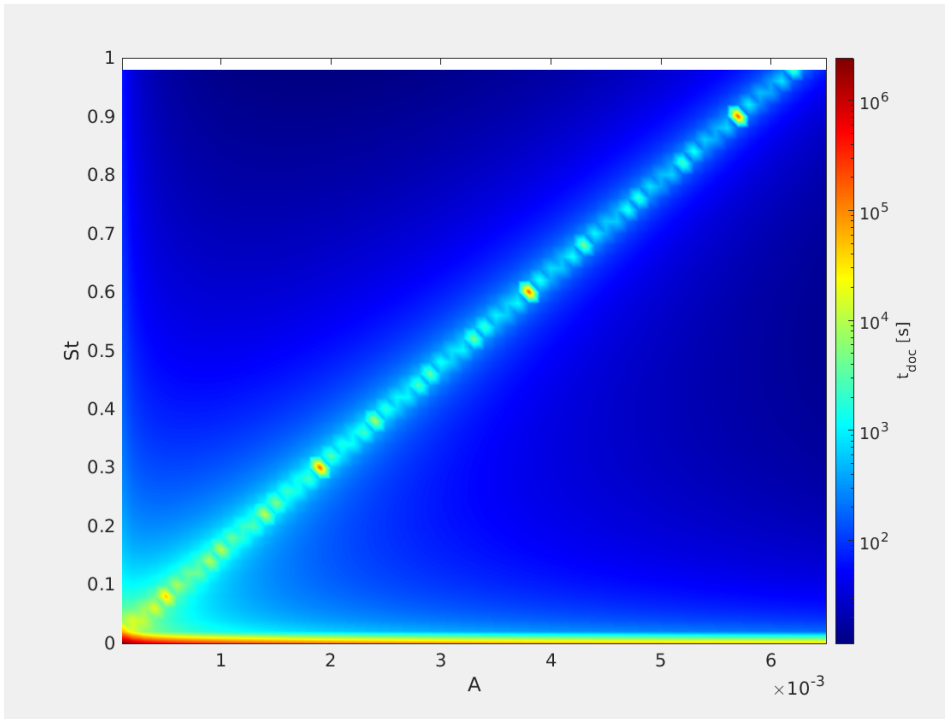


Figure 28: Dimensional docking time as presented in Fig. 27 in the case $R = 13 \mu\text{m}$.

Table 4: Burgers vortex non-dimensional numbers

A_{cr}	0.02176
r_i	2.1866
S_{vi}	0.0815
r_s	1.585201
S_{vs}	0.0718

and it can be uniquely determined by solving the equilibrium point equation:

$$f_A(r^+) = S_v, \quad (78)$$

where function $f_A(r^+)$ is defined for each A :

$$f_A(r^+) = r^+ A \sqrt{1 + \left(\frac{1 - \exp\left(\frac{-r^+}{2}\right)}{2\pi A r^+} \right)^2} \quad (79)$$

and is called an equilibrium curve (see Fig.2 in Marcu, Meiburg, and Newton [73]). Detailed analysis of this eqation's solutions is performed below.

Equilibrium curves for a dozen of A values are plotted in Fig. 29. It is easy to find that $f_A(0) = 0$ and $\lim_{r^+ \rightarrow \infty} f_A(r^+) = \infty$. Moreover, there exists a critical value of nondimensional strain A_{cr} for which bifurcation from one unique solution (for $A \geq A_{cr}$) to maximally three solutions (for $A < A_{cr}$) occurs. A_{cr} corresponds to the equilibrium curve that has a horizontal slope at the inflection point. A_{cr} value was estimated numerically (see the Table 4). It is also easy to prove that the equilibrium curves asymptotically tend to the function $f_{A \rightarrow 0+}(r) = (1 - \exp(-r^2/2)) / 2\pi r$. This function, unlike equilibrium curves for $A \in (0, A_{cr})$ does not have a minimum.

For $A \geq A_{cr}$ the equilibrium curve is a monotonically increasing function of r^+ so there exists exactly one solution for every S_v value. For $A < A_{cr}$ the equilibrium curve always has one maximum at r_{max}^+ and one minimum at r_{min}^+ . The inflection point of $A = A_{cr}$ equilibrium curve plot lies at r_i and for S_{vi} (numerical estimations in the Table 4). It restricts values of r_{max}^+ from above and values of r_{min}^+ from below. Let's define:

$$S_{v min} = f_A(r_{min}^+) \quad (80)$$

$$S_{v max} = f_A(r_{max}^+) \quad (81)$$

Consequently, for $S_v < S_{v min}$ and for $S_v > S_{v max}$, there is only one solution. For $S_v = S_{v min}$ and for $S_v = S_{v max}$, there are two solutions. For $S_{v min} < S_v < S_{v max}$, there are three solutions. All the conclusions are summarised in Table 5.

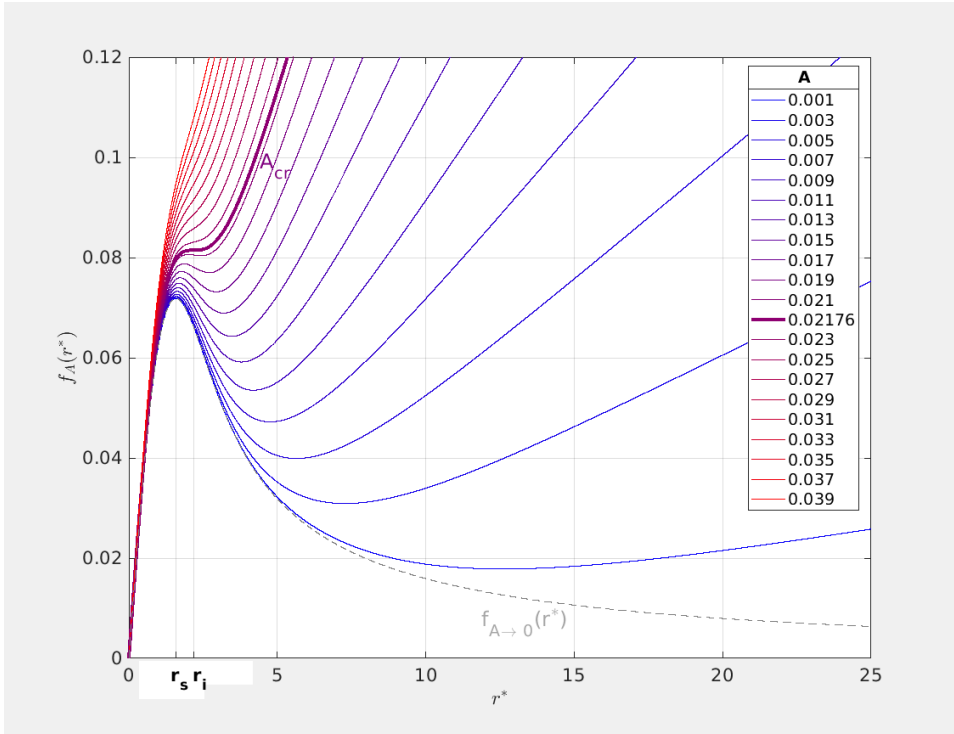


Figure 29: Equilibrium curve plots for different A values. A_{cr} , r_s , r_i are defined in the text body. Gray dashed line shows an equilibrium curve which is an asymptotic limit of $A \rightarrow 0+$

Table 5: Existence and position of equilibrium points with respect to A and S_v parameters. A_{cr} , r_s , r_{\min}^+ , $S_{v \min}$, $S_{v \max}$ are defined in the text body.

A	S_v	nr of eq. points
$\geq A_{cr}$	arbitrary	1
$< A_{cr}$	$< S_{v \min}$	1 at $r_0^+ < r_s$
	$[S_{v \min}, S_{v \max}]$	2 or 3, I: $r_0^+ \leq r_{\max}^+ < r_i$, II: $r_0^+ \in (r_{\max}^+, r_{\min}^+)$, III: $r_0^+ > r_{\min}^+$
	$> S_{v \max}$	1 at $r_0^+ > r_{\min}^+ > r_i$

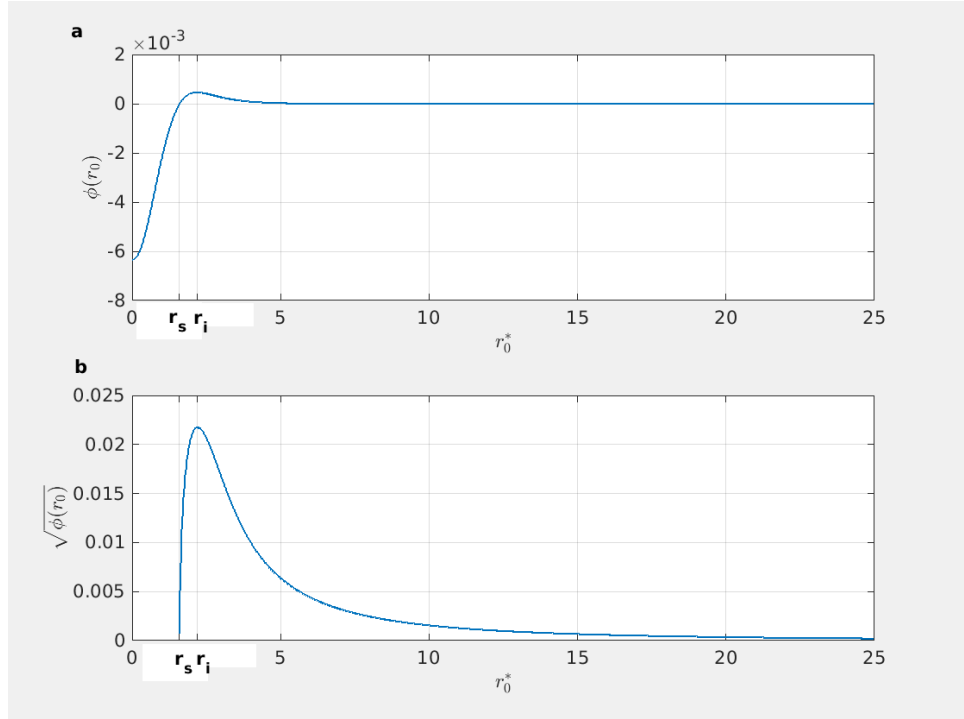


Figure 30: Plot of the function $\phi(r_0^+)$ determining equilibrium point stability (a) and its square radius $\sqrt{|\phi(r_0^+)|}$ (b) with respect to equilibrium point radial position.

Not only is the existence of the multiple solutions important but their stability as well. Let r_0^+ denote an arbitrary dimensionless solution of Eq. 78. The exact form of the stability condition of the solution r_0^+ is governed by the function $\phi(r_0^+)$ (defined in Marcu, Meiburg, and Newton [73]). The condition can take two different forms depending on the sign of this function:

$$\phi(r_0^+) = \frac{1}{(2\pi)^2} \left[\frac{1 - \exp(-r_0^{+2}/2)}{r_0^{+2}} \right] \left[\frac{1 - \exp(-r_0^{+2}/2)}{r_0^{+2}} - \exp(-r_0^{+2}/2) \right]. \quad (82)$$

Plots of $\phi(r_0^+)$ and its square root are shown in Fig. 30.

Function $\phi(r_0^+)$ has only one zero at r_s (see Table 4). For small radii, $r_0^+ < r_s$, the equilibrium is a spiral/focus, and it is stable if:

$$St \leq \frac{A}{|\phi(r_0^+)|}. \quad (83)$$

For greater radii, $r_0^+ > r_s$, the equilibrium point is either a stable node or a saddle. The condition for stability depends explicitly only on A :

$$A \geq \sqrt{|\phi(r_0^+)|}. \quad (84)$$

Table 6: Stability conditions of particle equilibrium points present in the Burgers vortex with respect to vortex strain parameter A and dimensionless radial position r^+ . A_{cr} , $\varphi(r^+)$, r_s , r_i , r_{min}^+ and r_{max}^+ are defined in the text body.

	$\leq r_s$	(r_s, r_{max}^+)	$[r_{max}^+, r_{min}^+)$	$\geq r_{min}^+$
$A < A_{cr}$	focus, unstable if $St > A/ \varphi(r_0^+) $	stable node	saddle	stable node
			stable node	

Analysis of the equilibrium point stability conditions by Marcu, Meiburg, and Newton [73] is expanded here with emphasis on the dependence on strain parameter A . Because stability condition for larger radii $r_0^+ > r_s$ expressed by Eq.84 is independent of St , additional conclusions can be drawn. Numerical calculations lead to the result, that for every $A < A_{cr}$ there is:

$$\sqrt{\varphi(r_{max}^+(A))} = \sqrt{\varphi(r_{min}^+(A))} = A. \quad (85)$$

In the range between maximum and minimum $r_0^+ \in (r_{max}^+, r_{min}^+)$ there is $\sqrt{\varphi(r_0^+)} > \sqrt{\varphi(r_{min}^+(A))}$, so the condition in Eq.84 is not satisfied and the points in this range are not stable. For $r_0^+ > r_{min}^+$ there is $\sqrt{\varphi(r_0^+)} < \sqrt{\varphi(r_{min}^+(A))}$, so the condition in Eq.84 is satisfied and the points in this range are stable. In the case $A \geq A_{cr}$ the condition in Eq.84 is satisfied, because $A > \max_{r_0^+} (\sqrt{\varphi(r_0^+)}) = A_{cr}$. The unique solution is a stable node. These results are summarised in Table 6.

The stability properties can be analysed with S_v as a leading parameter too, in contrast to equilibrium curve viewpoint. Figure 31 presents equilibrium point r_0^+ plots versus A . Line colors refer to various S_v parameters. Continuous line represents stable point, dashed - unstable. Three colored regions in the background mark three stability domains: light gray corresponds to condition in Eq.84 satisfied (a stable node), light green to the same condition not satisfied (a saddle), light red points to the focus region $r_0^+ < r_s$. Stability of the focus is governed by Eq.83, so St must be considered as well. An example of stability properties in the region $r_0^+ < r_s$ is shown by the cross signs - they represent the example of unstable foci for $St = 0.5$. r_s , r_i and A_{cr} are marked on the axes for reference.

In Fig. 31, the following conclusions about stability can be drawn. For $S_v < S_{vs}$ there is at least one focus near the axis, at $r_0^+ < r_s$, stable or unstable. When $A \geq A_{cr}$ it is unique, when $A < A_{cr}$ it can be accompanied by a saddle and a stable node or a stable node itself. For $S_v \in (S_{vs}, S_{vi})$ and when $A < A_{cr}$ there is at least the stable node far from the axis. In addition there can be the saddle and the stable node near the axis, the saddle and the focus or the focus itself. When

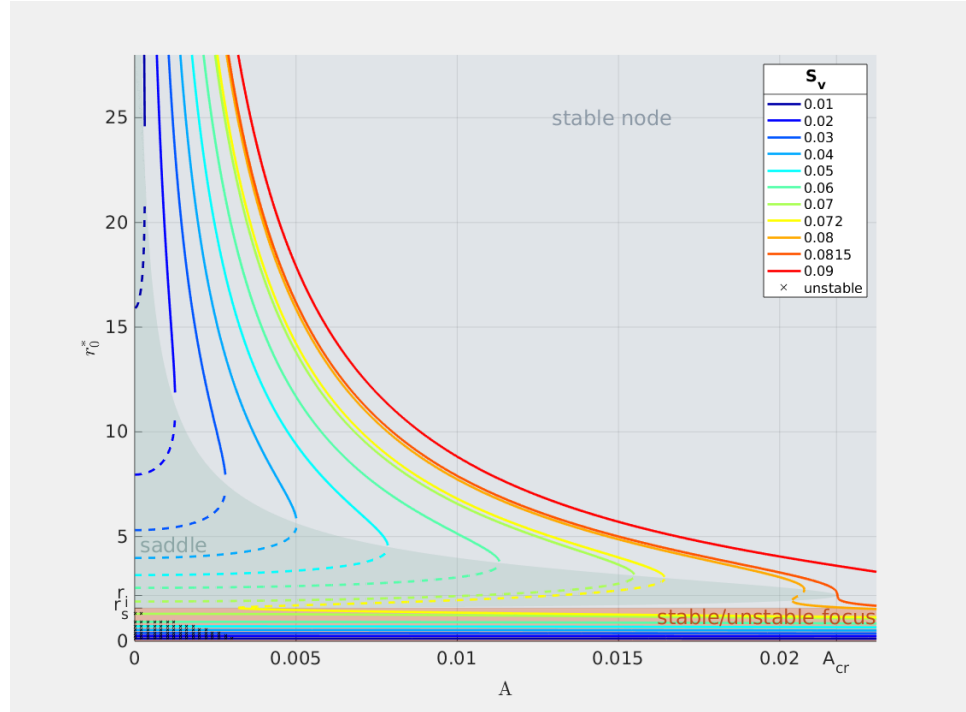


Figure 31: Equilibrium point r_0^+ position versus A . Line colors refer to various S_v parameters, continuous line - to stable point, dashed line - to unstable. The colored regions in the background mark various stability subdomains: light gray - a stable node, light green - a saddle, light red - a focus. Crosses show example of unstable foci in the light red region for the case of $St = 0.5$.

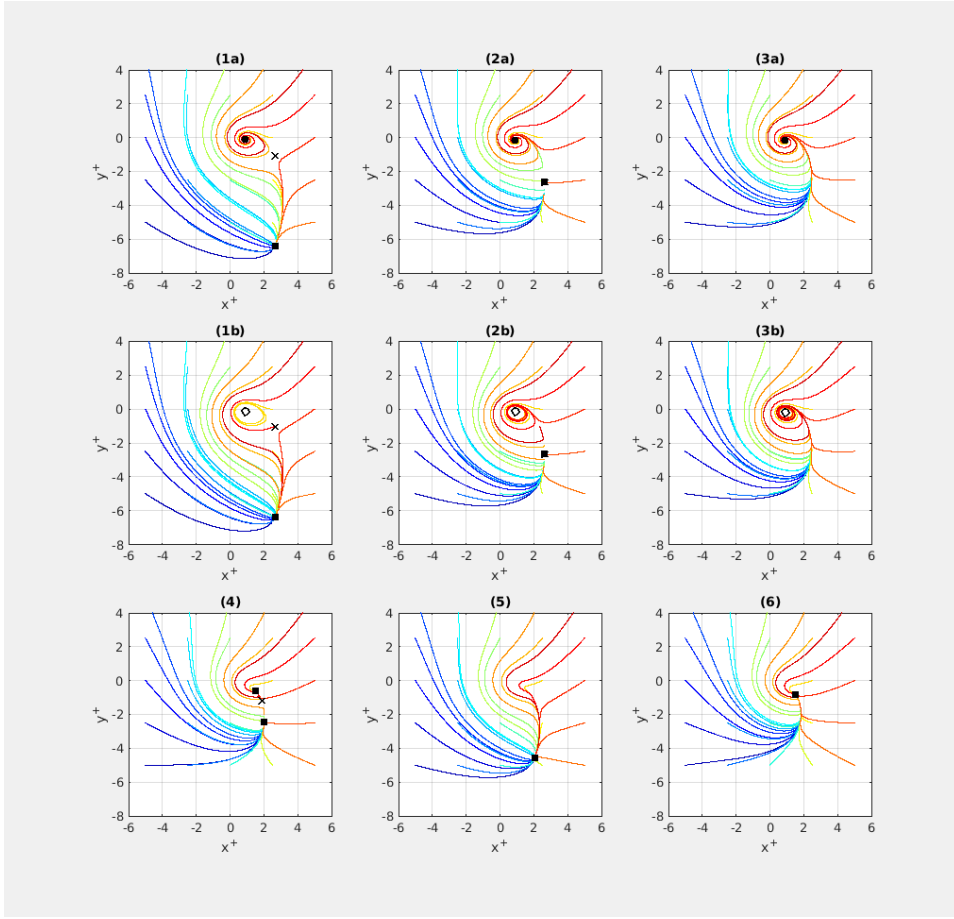


Figure 32: Particle trajectory plots for various sets of (A, Sv, St) parameters.

In each figure 25 particles are initialised at regular grid with zero velocity. Line colors vary in order to improve clarity. Scattered points represent equilibrium points position, their shape refer to their dynamical type: \times - a saddle, \circ - a focus (filled means stable), \square - stable node. "a" and "b" types present the same (A, Sv) sets, but with different St determining stability of the focus ("a" - stable, "b" - unstable).

$A \geq A_{cr}$ there is only one point near the axis and it is either a focus or a stable node. For S_{vi} there is bifurcation from three possible solutions to just one. When $A < A_{cr}$ the one is a unique stable node far from the axis, when $A \geq A_{cr}$ it is a unique stable node at arbitrary position or a focus near the axis.

The combination of multiple point existence conditions with stability conditions creates a variety of single particle motion scenarios. Some of them were shown in Fig.4-9 in Marcu, Meiburg, and Newton [73]. Fig. 32 here illustrates all nine of these combinations, by showing trajectory plots of particles initially positioned on the chosen grid with zero velocity. Trajectories were calculated numerically for representative sets of parameters. Different line colors are only intended

Table 7: Single particle motion scenarios with respect to A and S_v parameters. Numbers refer to Fig.32

	$A < A_{cr}$	$A \geq A_{cr}$
$S_v < S_{vs}$	(1) (2) (3)	(3)
$[S_{vs}, S_{vi}]$	(1) (2) (4) (5)	(3) (6)
$S_v > S_{vi}$	(5)	(3) (5) (6)

to improve the plot clarity. Singular markers indicate the position of the equilibrium points, while their shape - their dynamic character. Tab.7 summarises the analysis by showing A and S_v parameter ranges with relevant scenarios, as pictured in Fig. 32. These scenarios are of particular interest in the context of void phenomenon explanation, especially the cases with limit cycle. This special solution and its properties are addressed next.

Finding limit cycles in general is a very difficult problem, although there are important in many scientific applications. Numerical simulations show, that as $St/A - |\phi(r_0^+)|^{-1}$ passes through zero, Hopf bifurcation occurs. It means that if the focus near the axis is unstable according to 83, then it is accompanied by a stable limit cycle. The limit cycle cannot be calculated analytically or approximately. However the condition in Eq.83 for unstable focus can be approximated. The assumption needed is that $r^* \leq r_s^*$. Firstly it allows to expand the relation for equilibrium point position as in Eq. ?? in the vicinity of $r^* = 0$. The other assumption is that in this vicinity the dependence on A is weak (see Fig.2 in **Marcu_95**).

$$\left(\frac{Sv}{A}\right)^2 = r^{*2} \left[1 + \left(\frac{1 - \exp(-r^{*2}/2)}{2\pi Ar^{*2}} \right)^2 \right] = r^{*2} + \frac{(1 - \exp(-r^{*2}/2))^2}{(2\pi Ar^*)^2} \simeq r^{*2} + \frac{1}{4\pi^2 A^2} \frac{r^{*2}}{4}$$
(86)

so in the end:

$$r_0^* \simeq 4\pi Sv (1 + (4\pi A)^2)^{-\frac{1}{2}}.$$
(87)

It is equivalent to approximating vortex angular motion by rigid body rotation $u_\varphi^+ = r^+/4\pi$.

Secondly, the function $\phi(r_0^*)$ is approximated as follows:

$$\phi(r_0^*) \simeq -(16\pi^2)^{-1}(1 - r_0^*).$$
(88)

At $r^* = 0$ the (un)stability condition takes the same form as for the case without gravity.

The instability condition, which is, to the best knowledge, equivalent to the existence of a limit cycle, after algebraic transformations comes down to the requirement that the strain parameter is small enough

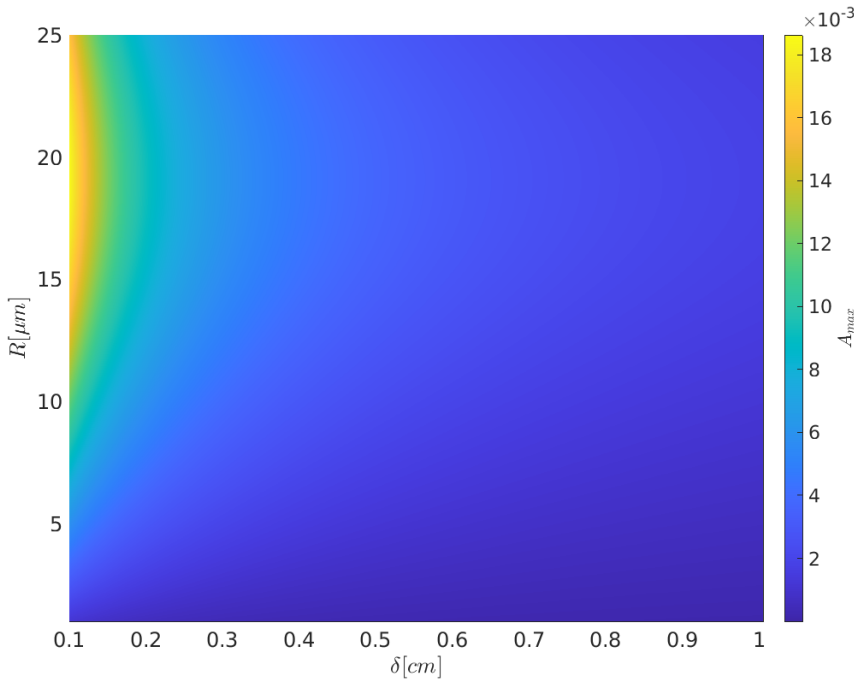


Figure 33: Maximal strain parameter A_{\max} with respect to vortex core size δ and particle radius R , for an arbitrary alignment angle $\theta = \pi/4$.

$A < A_{\max}$ and consequently circulation large enough $\Gamma > \Gamma_{\min}$, where the A_{\max} value is estimated as follows:

$$P \equiv 1 + v^{-1} g^2 \tau_p^3 \sin^2 \theta - 2^{-1} \tau_p \gamma, \quad (89)$$

$$A_{\max} = \left[2^{-1} (4\pi)^{-2} P ((1 + 2 \frac{\tau_p \gamma}{P^2})^{\frac{1}{2}} - 1) \right]^{\frac{1}{2}}. \quad (90)$$

A_{\max} makes sense only if P takes positive values and this is equivalent to the condition that $R/\delta < \sqrt{(\frac{g \rho_a}{2 \rho_p})} \approx 0.067$. This is guaranteed for cloud-like conditions. The maximal strain parameter A_{\max} (minimal circulation Γ_{\min}) increases (decreases) weakly with P . However the direct link to system parameters is intricate. Fig.33 presents its value vs. particle radius and vortex core size for an arbitrary alignment angle.

Figure 34 presents the same relation in a slightly different form. There are just a few δ values explored. Each coloured band represents A_{\max} range obtained for a bundle of alignment angles $\theta \in (0, \pi/2)$. While increasing R , for small particle radii, A_{\max} increases almost linearly with R , then for the larger radii the relation reaches maximum and A_{\max} starts to decrease with R . The linear dependency for $\theta = 0$ agrees with the relation shown in 70, so $A_{\max} \propto R/\delta$ for small particle radii. The position of the maximum depends on θ and is practically independent of δ (at 17.10 μm for $\theta = \pi/2$ and for $\delta = 0.1 \text{ cm}$, at 17.00 μm for $\theta = \pi/2$ and for $\delta = 0.9 \text{ cm}$). As a consequence, A_{\max} values are constrained from above for a given δ and θ , so there is a

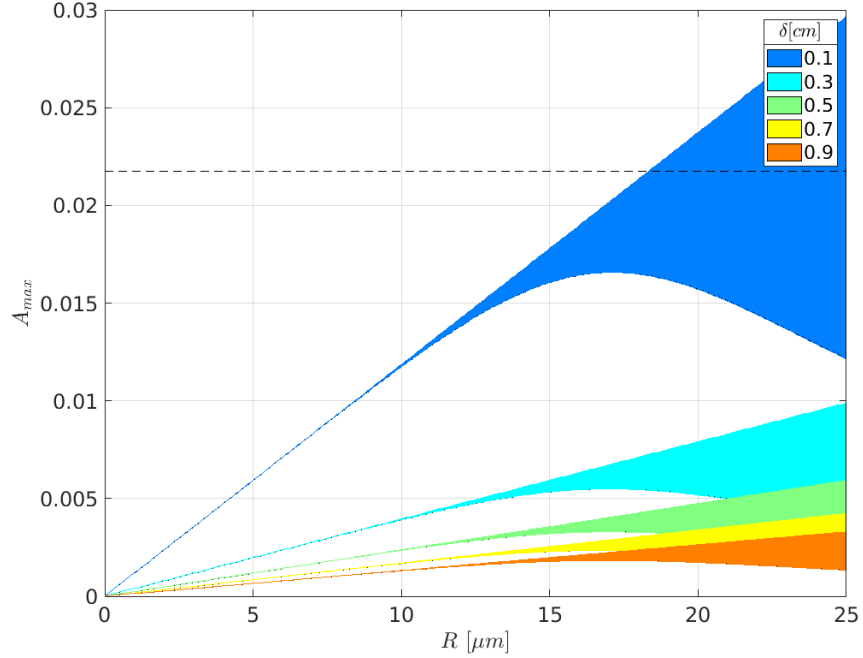


Figure 34: Maximal strain parameter A_{max} with respect to particle radius R for a few vortex core sizes δ , drawn for a bundle of alignment angles. A_{cr} value is shown with a dashed line.

Table 8: Summary of single particle motion timescales

$\tau_z \approx 2\gamma^{-1}$
$\tau_{ex}(Z^*, z_0^*; \tau_z) \approx \tau_z \log(L(Z^*, z_0^*))$
$\tau_{orb} = \sqrt{2\tau_p \gamma^{-1}}$
$\tau_{d1} = 2\gamma^{-1} \left(1 - \frac{S_t}{(4\pi)^2 A}\right)^{-1}$

value of A above which there is no limit cycle solution for any particle size. The other way of looking at this solution is that for arbitrary δ and θ , for a given A there exist a range of particle sizes R that has a limit cycle solution. Increasing strain A , core size δ or the angle θ narrows this range. This fact becomes important when dealing with polydisperse set of particles and is addressed in the next chapter.

3.3 TIME SCALES OF SINGLE PARTICLE MOTION

Approximate relations of a few timescales for single particle motion in Burgers vortex were found: exit time τ_{ex} , connected to timescale of motion along the axis τ_z , no-gravity orbit rotation timescale τ_{orb} and no-gravity axis docking timescale τ_{d1} . For ease of reference, these approximations are summarised in Table 8. Several conclusions about

three dimensional particle motion can be drawn from the comparison of the separately derived time scales:

1. τ_z is approx. independent of particle radius R and vortex strain A .
2. $\tau_{\text{orb}} \ll \tau_z$, so as long as the logarithmic part in Eq.57 is not significantly smaller than 1, the particle starting far from vortex "lids" is able to swirl around the vortex axis for significant amount of time before being expelled by motion along vortex axis.
3. The relation between axis docking timescale and motion along the axis timescale depends primarily on St/A parameter:

$$\frac{\tau_z}{\tau_{d1}} = 1 - \frac{St}{(4\pi)^2 A}. \quad (91)$$

If $St/A \approx 0$, then $\tau_z \approx \tau_{d1}$. Increasing St/A causes τ_z to be smaller than τ_{d1} . It means that in general, particles are expelled from the vortex through its lids faster than approach the vortex axis in docking process. The difference is larger the larger St/A is. The exact relation between process times depend on the initial conditions of particle motion as well.

3.4 SUMMARY

The subject of this chapter was the motion of a single finite-size particle subjected to viscosity and gravity forces only, in a steady fluid motion modelled by a Burgers vortex with stretching. This analysis bridged the gaps and deepened the knowledge on the subject presented in the paper of Marcu, Meiburg, and Newton [73] and by setting a relation to conditions expected in atmospheric clouds. Generally it proves the hypothesis that the nature of 3D cloud droplet motion in such a simplified system is complex and very much dependent on the parameters of the model, which are here vortex stretching, strain, alignment angle and particle size. It cannot be easily reduced or approximated. Particle motion in 2D is governed by orbit attraction/repulsion, which are foci, nodes, circular periodic orbit and/or limit cycle. How much the presence of these orbits determines the total motion of a particle in 3D is primarily influenced by the ratio of time scales of motion in 2D and along the axis. This ratio can be explicitly specified only in selected cases of motion. The intuition suggests that when it comes to multi-particle, polydisperse system, these results demonstrate a great potential in particle segregation, clustering and relative velocity influence.

4

CLOUD VOIDS - INTERPRETATION AND EXPLANATION

This chapter presents experimental, theoretical and numerical results concerning cloud voids. Cloud voids are a phenomenon that was registered only once and was published for the first time in Karpińska et al. [62] by the author of this thesis and others, including the experimental group. 4.1 presents the experimental results in details. 4.2 proposes the necessary conditions for cloud void formation, assuming the model exploited in Chapter 3 in polydisperse particle case and verifies them in cloud-like conditions.

4.1 CLOUD VOIDS EXPERIMENT RESULTS

Cloud voids observations were performed at UFS on Zugspitze slopes in August 2011. Experimental methods used were described in Sec. Section 2.4. This section presents the measurement results.

First, 30-minute long records of turbulence and droplet properties corresponding to the camera acquisition series in two measurement days were chosen for analysis. Droplet size raw measurements are presented in Fig. 35 and the corresponding statistics in Table 9. Both cloud droplets, as well as drizzle drops were captured. On August 29th the droplet number concentration was visibly larger. Unfortunately the device deficiency did not allow for reliable measurement of the droplet concentration on August 29th. Next, the probability distribution of the droplet size has been calculated and presented in Fig. 36. There are clear differences between the distributions measured on both days: the first one is much wider, the tail reach larger values and on average the droplets are about twice as big.

High-resolution measurements of small-scale turbulence during cloud void events were conducted. Applying the methods described in Sec. Section 2.4.1, mean energy dissipation rates and Kolmogorov scales were determined. Droplet and turbulence measured properties together with derived parameters are summarized in Table 9. Values of dimensionless parameters were calculated with the use of mean radius and Kolmogorov timescale. There is about one order of magnitude difference in St between two cases, but the Froude numbers are comparable.

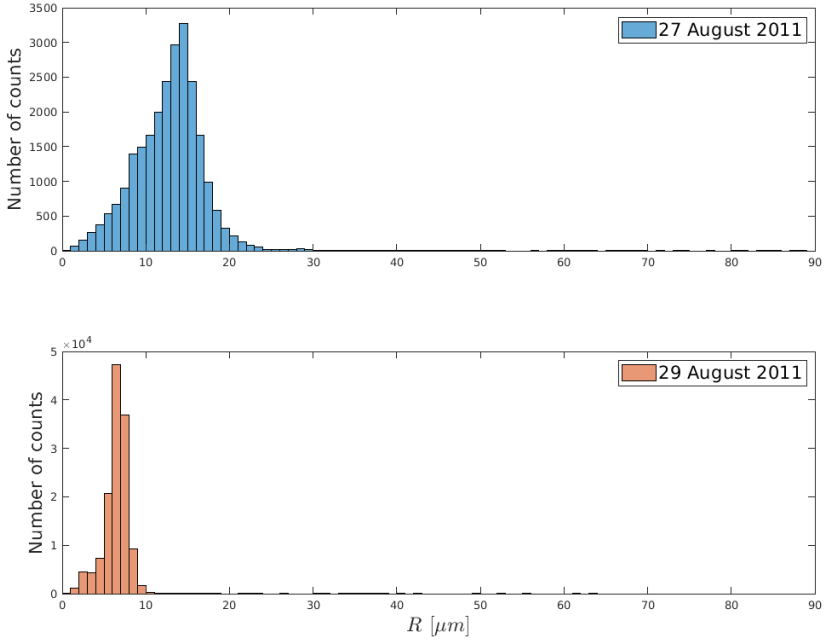


Figure 35: Histograms of droplet size counts measured with a PDI probe at the UFS on 27th and 29th of August 2011.

Multiple cloud images and movies were collected by laser-sheet imaging technique on the measurement days. In general two kinds of events in which droplet spatial distribution is visibly inhomogeneous were distinguished. The first kind is characterized by an irregular interface separating clear-air and cloudy-air volumes and/or cloudy volumes of visibly different properties over a wide range of spatial scales (panel b) in Fig. 37). Inhomogeneities of the second kind, present within the cloudy volumes, were called cloud voids in "Swiss cheese" clouds. Cloud voids were small (a few centimetres scale), the interface was usually blurry (see panels a) and c) in Fig. 37) and the shapes of clear-air regions were often close to round or elliptic (see magnified voids in Fig. 38). It is important to point out that the more intuitive expression "cloud holes" with regards to the second kind inhomogeneities is avoided on purpose because it is commonly used referring to the cloud-free regions occurring in stratocumulus decks, as described for example in Gerber_2005.

Inhomogeneities of the first kind are argued to be created in the process of cloud – clear-air mixing (e.g. [Warhaft_2000]). In contrast, in some series of images and movies, the shape of the recorded tracks of cloud droplets suggest the following cloud void origin hypothesis: they result from interactions between inertial, heavy cloud droplets and small-scale vortices present in a turbulent cloud. Comparison of the two described cases becomes straightforward when conducted on the basis of the enclosed movies [database]. In the movie "ms01" be-

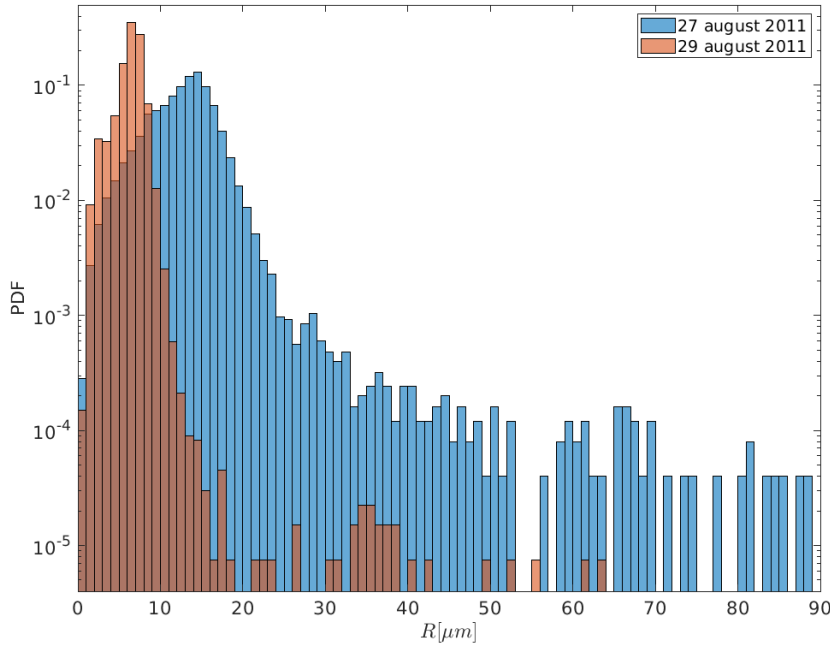


Figure 36: Droplet size probability distributions calculated for the data obtained with a PDI probe at the UFS on 27th and 29th of August 2011.

tween 13 s and 22 s there are two cloud void appearances. Motion of the void in the homogeneous cloud field resembles motion of a worm. Movie "ms02" presents cloudy and clear air mixing at the cloud edges.

There were a few series of cloud void images collected with various laser-camera settings on the two experimental days. The best quality series, made in the morning of the 27th, was chosen for void size analysis. For the series of 17 photos selected for analysis, there were four in which voids were not clear enough to be accounted for. In the remaining 13 photos 27 voids were identified. Each one's size was manually determined. In the case of a round void, the diameter was taken as the size; in a case of flattened or ellipsoidal void, the maximal chord was taken. The typical void diameter was estimated to be 3.5 ± 1 cm; the maximal, 12 ± 4 cm; the minimal, 1 ± 0.5 cm. Images from the analysed series from the morning of August 27th showing examples of objects identified as voids are presented in the panel a) of Fig. 37. Voids captured on the 29th of August were not analysed due to the large uncertainty resulting from the unknown geometry of the camera-laser set-up. The general experimental observation was that the voids were smaller than those on August 27th. Definitive experimental verification of the cloud void origin is not possible on the basis of collected data only; however, in next sections, I argue that

Table 9: Properties of turbulence and cloud droplets during 30-minutes long observation periods. Values of dimensionless parameters are calculated with the use of mean radius.

	August 27th	August 29th
Energy dissipation rate ϵ [cm ² /s ³]	550	700
Kolmogorov length scale η [mm]	0.50	0.47
Komogorov timescale τ_η [ms]	17	15
Droplet radius R [μm]	12.9 ± 4.8	6.4 ± 1.5
Stokes number St	0.126	0.035
Sedimentation parameter S_v	0.676	0.172
Froude number Fr	0.186	0.203
Number density n [cm ⁻³]	56 ± 47	no data

void creation due to inertia of droplets present inside vortex tubes is highly probable.

4.2 CLOUD VOID CREATION CONDITIONS

Lets assume that cloud voids are caused by the presence of a long-lasting vortex that appear numerously in turbulence structure and lets use the model of particle motion in a vortex explored in [Chapter 3](#), applied to cloud particles in atmospheric turbulence. Is the model able to produce a "void effect"? If yes, what are the necessary conditions? How they translate to model parameters? This section tries to answer all these questions.

The use of analytical model requires the precise definition of a void. For the start, we have a collection of cloud droplets of certain size distribution, distributed uniformly in the air, where the appearance of a Burgers vortex of a certain size, circulation and gravity alignment, creates a void of a few centimetres size, lasting a few seconds. Here the void is defined as an inhomogeneity in droplet field, a region almost devoid of droplets. It has nearly cylindrical shape, in the cross section it takes a form close to a circle or an ellipsoid. In order to obtain a void using the model, the following hypothesis on polydisperse particle collective behaviour are formulated. Firstly, the majority of droplets' trajectories are determined by limit cycle attraction. Secondly, the radius of curvature of the limit cycle is large enough to recognize it, as the void in observations is clearly distinguishable from random spatial distribution fluctuations. Attraction by a single stable equilibrium point far from the axis is not considerable, so the trajectories do not cross the void. Finally, the time needed to form the void is shorter then exit time for most of the particles. These conditions are inspected in the following subsections.

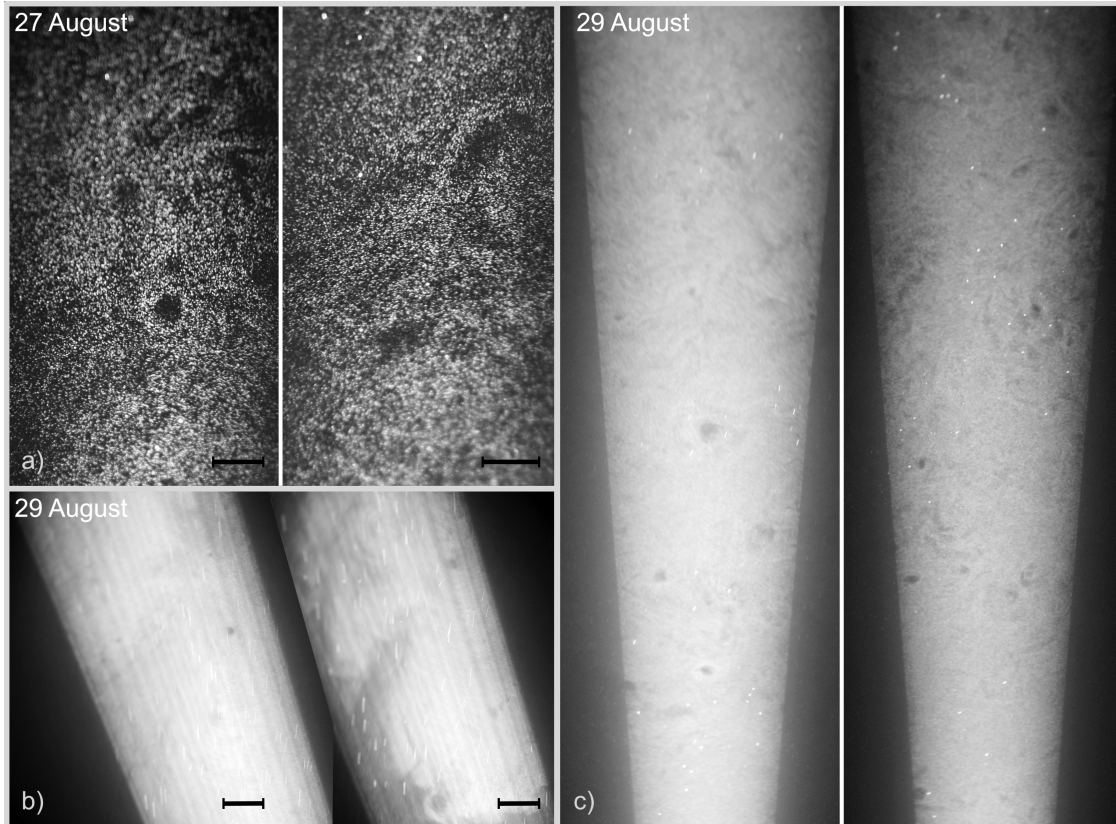


Figure 37: Examples of cloud voids observed at the UFS station with various camera-laser configurations. Images taken on 27 August (panel a) were chosen to estimate cloud void sizes. The ones recorded on 29 August evening (panel b) show the difference between inhomogeneities produced by cloud voids and those resulting from the mixing with clear air at the cloud edge. Other images from 29 August (panel c) suggest that the voids can be quite frequent in the sample volume. Bright spots and lines are due to presence of larger precipitation particles. 10 cm long segment is shown to represent spatial scale assumed in the void size calculation. For more details, see the movies attached in the supplementary materials.

4.2.1 Polydisperse droplet trajectories

The conditions defined above for the motion of the polydisperse collection of droplets in the 2D space are met if most of the drops realize motion scenarios referred to in Fig. [Figure 32](#) as (1b)-(3b), and possibly only a small part of the largest droplets of scenario (5). If there is a void characterized by (A, δ, θ) , then the size range $[R_<, R_>]$ of particles that realize one or more of the scenarios (1b)-(3b) is constrained. All of the particles must have at least one unstable focus r_0^+ near the axis. This is guaranteed by the two conditions: $r_0^+ < r_s$ and $A < A_{\max}(R, \delta, \theta)$ for all $R \in [R_<, R_>]$. So for a vortex described by (A, δ, θ) the range $[R_1, R_2]$ is approximately defined by A_{\max} as described in last paragraph of [Section 3.2.2](#). However, it can be fur-

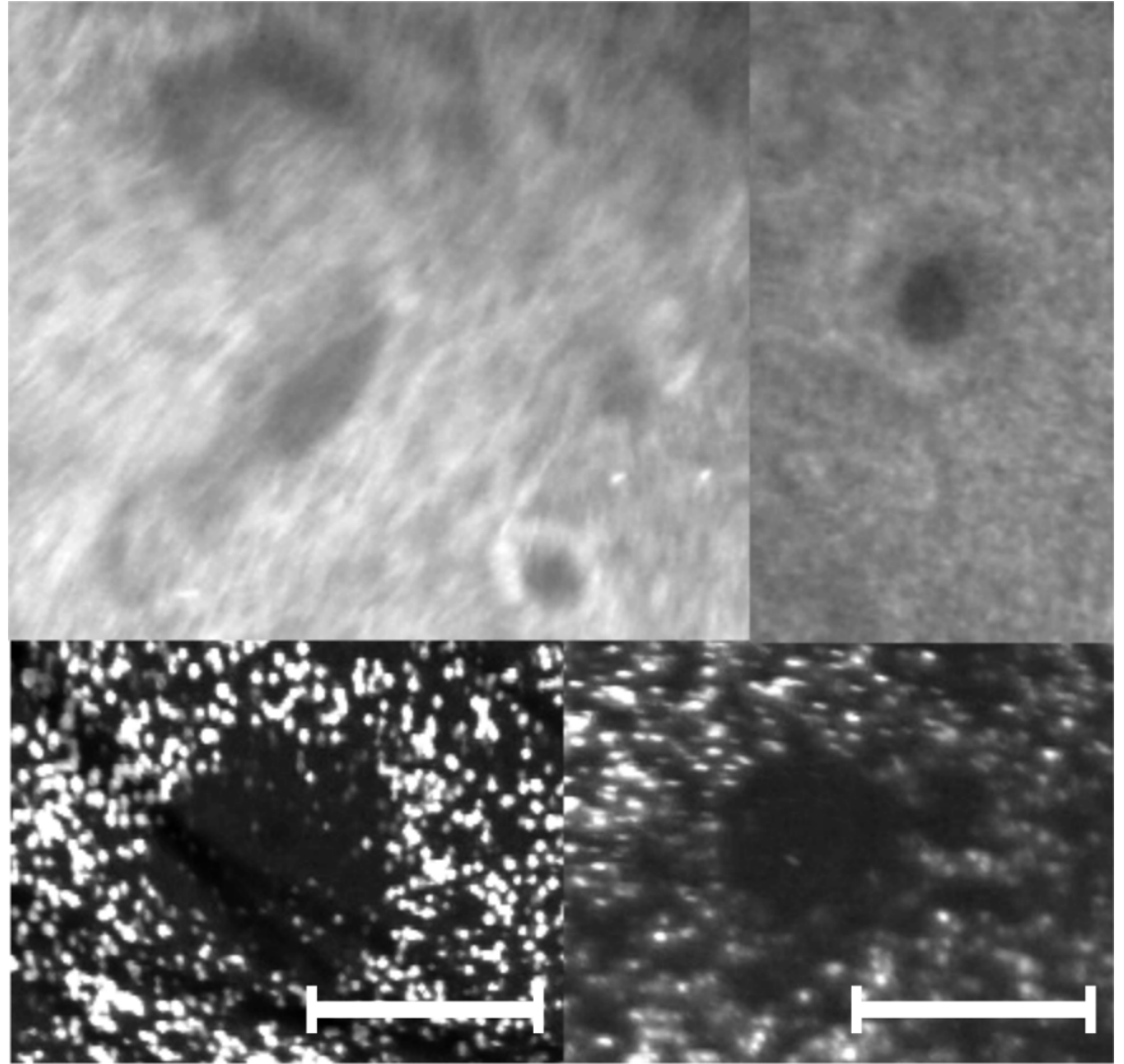


Figure 38: Example close-ups of variously shaped cloud voids observed at the UFS station with different camera-laser configurations. 5 cm long section is placed in each image to represent spatial scale assumed in the void size calculation.

ther restricted by the condition $r_0^+ < r_s$. To verify the last, a value called R_s is calculated numerically and it is defined by the relation $r_0^+(R_s, A, \delta, \theta) = r_s$. Finally, limit cycle is a solution for a range of particle radii $[R_<, R_>]$ if:

- $R_1 < R_s < R_2$, then $R_< = R_1, R_> = R_s$, or
- $R_1 < R_2 < R_s$, then $R_< = R_1, R_> = R_2$.

Figure 39 presents results of numerical calculations of R_1, R_2, R_s in the vortex parameters domain, specific for cloud-like conditions (first, second and third row respectively). Colour scale was selected to be common to all three variables. Alignment angle θ cases are arbitrary, but smaller than $\pi/4$, for the clarity of the figures. For the larger the

angle, the narrower the A and δ domain in which limit cycle is a solution. The fourth row shows the difference $R_2 - R_s$. R_1 decreases when strain parameter A decreases (circulation increases) or vortex size δ decreases. On the contrary to R_1 , R_2 and R_s increase when strain parameter A decreases (circulation increases) or vortex size δ decreases. The last row reveals, that the inequality sign between R_2 and R_s is not constant, but changes with vortex parameters. $R_>$ should be calculated in two ways, depending on these parameters.

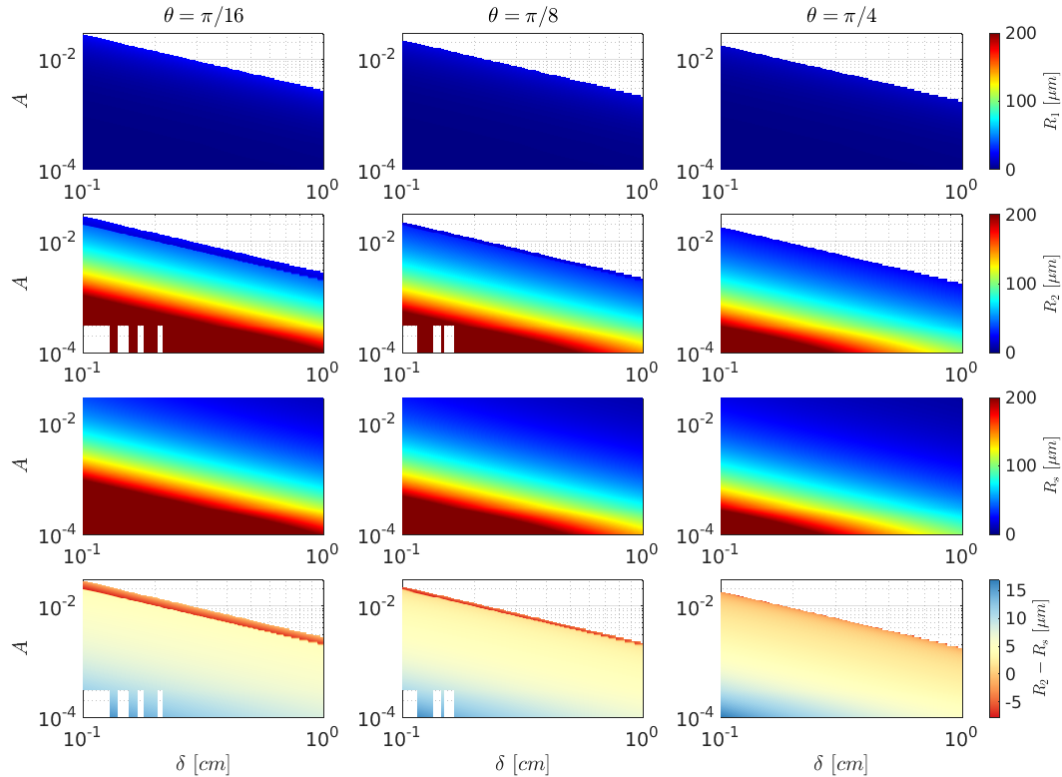


Figure 39: Approximated size range of particles $[R_1, R_2]$ that has a limit cycle solution, represented by color scale, with respect to vortex parameters (first and second row), R_s (third row), as defined in the text body and the interval between R_2 and R_s (fourth row), obtained numerically. Colorscale is common for R_1 , R_2 and R_s , separate for $R_2 - R_s$. Three alignment angle values selected are represented in columns. Vortex parameters domain corresponds to cloud-like conditions.

Figure 39 shows final results: left margin of the range $R_>$, right margin of the range $R_<$ and their interval magnitude, thus giving approximate parameter ranges of cloud void-creating vortex. Colour scales in this case differ to highlight the accurate values. Presented $R_<$ values reach from around $29 \mu\text{m}$ for $\theta = \pi/16$ and around $19 \mu\text{m}$ for $\theta = \pi/4$ to well below $1 \mu\text{m}$, so they are surely relevant for cloud droplets. $R_>$ has opposite A dependence and it reaches from around

$17 \mu\text{m}$ for all three theta to particle sizes that are far out of cloud droplets bounds. What is interesting, is the interval magnitude ΔR . The minimal value of those presented in the figure is $\min(\Delta R) = 27, 14, 4 \mu\text{m}$ for $\theta = \pi/16, \pi/8, \pi/4$ respectively. These are also values that are of the same order as in cloud conditions.

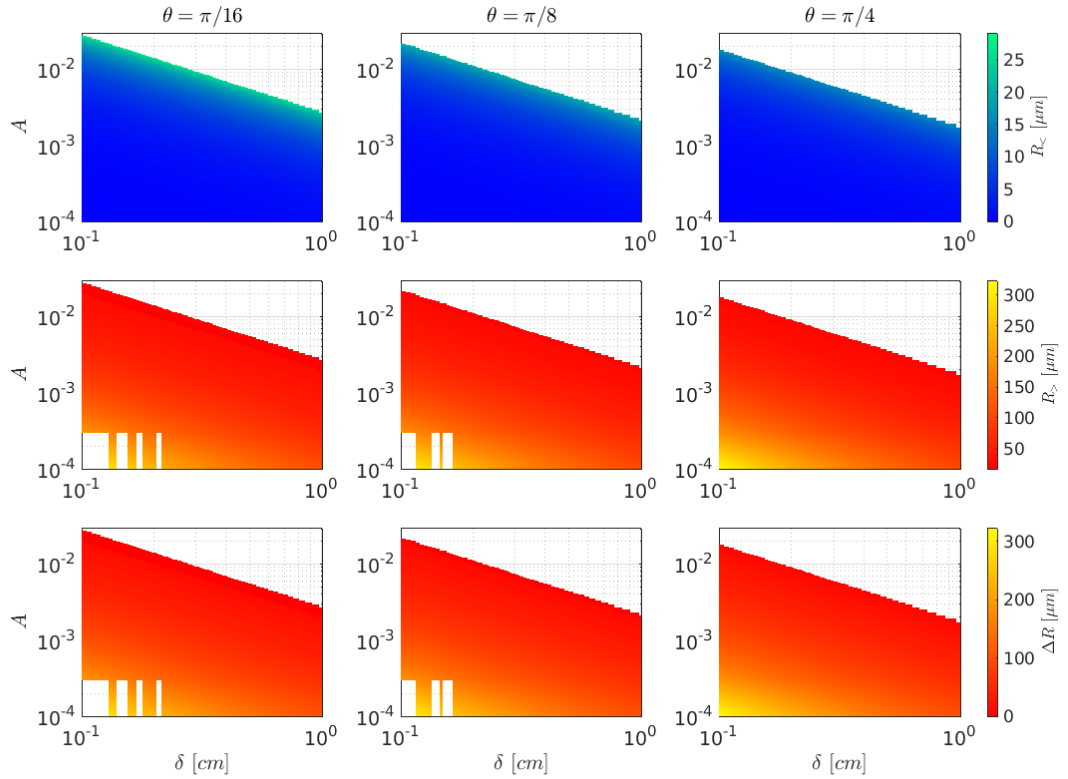


Figure 40: Numerical calculation of approximated size range of particles $[R_<, R_>]$ (first and second row) that create a cloud void, as well as interval between them ΔR (third row) in relation with vortex parameters. Colorscale is common for $R_>$ and ΔR . Three alignment angle values selected are represented in columns. Vortex parameters domain corresponds to cloud-like conditions.

R_1 decreases when strain parameter A decreases (circulation increases) or vortex size δ decreases. On the contrary to R_1 , R_2 and R_s increase when strain parameter A decreases (circulation increases) or vortex size δ decreases.

Finally some general clues about cloud void formation in 2D on the basis of theoretical model are lined:

1. There is a threshold (minimal) value of circulation needed for void creation (corresponding to A_{\max}). It increases with inclination angle ($\sin \theta$) and vortex size δ .

2. The greater the circulation the smaller particles have their unstable points near the axis.
3. The range of particles having unstable points near the axis increases with increasing circulation and decreases with increasing inclination angle and vortex size δ .

Building up on these results it may be concluded that theoretical void formation conditions can be fulfilled in cloud-like conditions when it comes to 2D space. According to the model it should be harder to observe voids in vortices of larger δ . When it comes to the inclination, the larger the angle, the smaller the particles thrown out of vortex center. On the other hand, increasing inclination angle decreases the range of particles circling around the void. However, larger droplets motion resemble then sedimentation through the vortex and altogether increasing inclination angle might facilitate void formation. The last conclusion is that it should be more difficult to observe voids the larger particle size range is.

4.2.2 Void size estimation

The curvature of droplet trajectories should be large enough for a void to be noticeable. In order to estimate the curvature radius we perform the following reasoning. In the face of lack of analytical limit cycle solution, droplet trajectory curvature radius can be approximated by the periodic orbit radius, which was explored in detail in [Section 3.2.1.1](#). For this reason, stable periodic orbit radius numerical calculation results are presented in a novel form in Fig.?? for various representative vortex parameters. Every color represents one of droplet sizes: $R = 3, 13, 23 \mu\text{m}$ chosen to be within the experimental range for August 27th (see Table 9). The figure illustrates contour plots for selected orbit radii (0.5 cm, 2 cm, 5 cm), corresponding to cloud void sizes observed. Overlapping (blue on a top, then pink and green) coloured surfaces match subspaces of stable periodic orbit existence.

Figure ?? shows the results of r_{orb} calculation in a different view.

Figure 41 further narrows down the void-forming parameter domain.

4.2.3 Timescales of motion

Timescales of motion found for a single particle can be interpreted in the case of polydisperse collection of particles. Lets take the arbitrary range of sizes $[R_-, R_+]$ and find the relations between their timescales. Firstly, motion along vortex axis is governed by τ_z quantity, which approximately does not depend on particle size. Difference in total

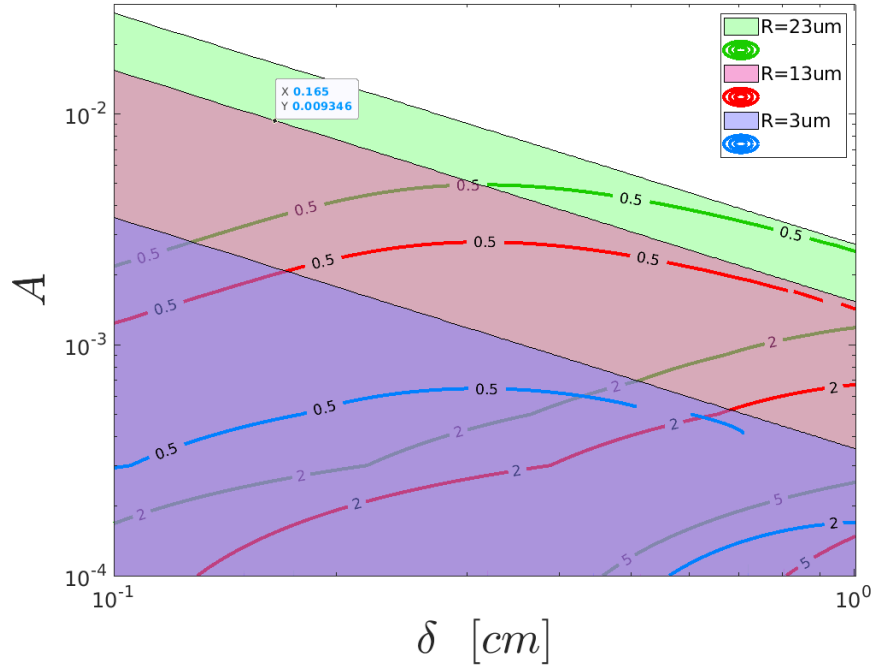


Figure 41: Contour plot of stable periodic orbit radius for droplets of radii $R = 3, 13, 23 \mu\text{m}$ for cloud-like parameter ranges of δ and A . Overlapping (blue on a top, then pink and green) coloured surfaces match parameter domains in which stable periodic 2D orbit exist for droplet radius given by its colour. Dashed lines are contour plots for r_{orb} equal to 0.5 cm ,2 cm, 5 cm. Black points represent simulation parameters sets (filled later, referred to in ???).

exit times results from the difference of equilibrium point position $z_b \propto R^2$ and according to Eq.57:

$$\frac{\tau_{ex>}}{\tau_{ex<}} = \frac{\log(L(Z_{>}^*, z_{0>}^*))}{L(Z_{<}^*, z_{0<}^*)}. \quad (92)$$

When it comes to circular orbit timescale, there is:

$$\frac{\tau_{orb>}}{\tau_{orb<}} = \frac{R_{>}}{R_{<}}, \quad (93)$$

so it increases proportionally with droplet size. Finally the relations for docking times are implicit. Figure [Figure 28](#) - tu opisac, ze tam gdzie dazy do nieskonczonosci czas dokowania, to wiadomo, ze szybciej wypadna przez τ_{dok} mniejsze. A takie regiony sa dwa. Moze ten wykres przerobic na delta i A, zeby byl porownywalny z tymi powyzej?

4.3 SUMMARY

3D void formation due to the presence of Burgers vortex in droplets field is fully possible for cloud-like conditions.

5

CLOUD VOIDS SIMULATIONS

5.1 NUMERICAL SIMULATION RESULTS

5.2 MIE SCATTERING INFLUENCE

5.3 PREFERENTIAL CONCENTRATION STATISTICS

6

SUMMARY AND DISCUSSION

BIBLIOGRAPHY

- [1] In: () .
- [2] In: () .
- [3] In: () .
- [4] In: () .
- [5] In: () .
- [6] A. Arnèodo et al. "Universal Intermittent Properties of Particle Trajectories in Highly Turbulent Flows." In: *Phys. Rev. Lett.* 100 (25 June 2008), p. 254504. DOI: [10.1103/PhysRevLett.100.254504](https://doi.org/10.1103/PhysRevLett.100.254504). URL: <https://link.aps.org/doi/10.1103/PhysRevLett.100.254504>.
- [7] Orlando Ayala, Bogdan Rosa, Lian-Ping Wang, and Wojciech W Grabowski. "Effects of turbulence on the geometric collision rate of sedimenting droplets. Part 1. Results from direct numerical simulation." In: *New Journal of Physics* 10.7 (July 2008), p. 075015. DOI: [10.1088/1367-2630/10/7/075015](https://doi.org/10.1088/1367-2630/10/7/075015). URL: <https://doi.org/10.1088%2F1367-2630%2F10%2F7%2F075015>.
- [8] Lucia Baker, Ari Frankel, Ali Mani, and Filippo Coletti. "Coherent clusters of inertial particles in homogeneous turbulence." In: *Journal of Fluid Mechanics* 833 (2017), pp. 364–398. DOI: [10.1017/jfm.2017.700](https://doi.org/10.1017/jfm.2017.700).
- [9] J. Bec, L. Biferale, M. Cencini, A. Lanotte, S. Musacchio, and F. Toschi. "Heavy Particle Concentration in Turbulence at Dissipative and Inertial Scales." In: *Phys. Rev. Lett.* 98 (8 Feb. 2007), p. 084502. DOI: [10.1103/PhysRevLett.98.084502](https://doi.org/10.1103/PhysRevLett.98.084502). URL: <https://link.aps.org/doi/10.1103/PhysRevLett.98.084502>.
- [10] JÃ©rÃ©mie Bec, Samriddhi Sankar Ray, Ewe Wei Saw, and Holger Homann. "Abrupt growth of large aggregates by correlated coalescences in turbulent flow." In: *Phys. Rev. E* 93 (3 Mar. 2016), p. 031102. DOI: [10.1103/PhysRevE.93.031102](https://doi.org/10.1103/PhysRevE.93.031102). URL: <https://link.aps.org/doi/10.1103/PhysRevE.93.031102>.
- [11] Jeremie Bec. "Multifractal concentrations of inertial particles in smooth random flows." In: *Journal of Fluid Mechanics* 528 (2005), pp. 255–277. DOI: [10.1017/S0022112005003368](https://doi.org/10.1017/S0022112005003368).

- [12] Jérémie Bec, Luca Biferale, Guido Boffetta, Massimo Cencini, Stefano Musacchio, and Federico Toschi. "Lyapunov exponents of heavy particles in turbulence." In: *Physics of Fluids* 18.9 (2006), p. 091702. DOI: [10.1063/1.2349587](https://doi.org/10.1063/1.2349587). eprint: <https://doi.org/10.1063/1.2349587>. URL: <https://doi.org/10.1063/1.2349587>.
- [13] Jérémie Bec, Luca Biferale, Massimo Cencini, Alessandra S. Lanotte, and Federico Toschi. "Effects of vortex filaments on the velocity of tracers and heavy particles in turbulence." In: *Physics of Fluids* 18.8 (2006), p. 081702. DOI: [10.1063/1.2338598](https://doi.org/10.1063/1.2338598). eprint: <https://doi.org/10.1063/1.2338598>. URL: <https://doi.org/10.1063/1.2338598>.
- [14] Jérémie Bec, Holger Homann, and Samriddhi Sankar Ray. "Gravity-Driven Enhancement of Heavy Particle Clustering in Turbulent Flow." In: *Phys. Rev. Lett.* 112 (18 May 2014), p. 184501. DOI: [10.1103/PhysRevLett.112.184501](https://doi.org/10.1103/PhysRevLett.112.184501). URL: <https://link.aps.org/doi/10.1103/PhysRevLett.112.184501>.
- [15] F. Belin, F. Moisy, P. Tabeling, and H. Willaime. "Worms in a turbulence experiment, from hot wire time series." In: *Fundamental Problematic Issues in Turbulence*. Trends in Mathematics. Springer Basel A.G., 1999, pp. 129–140. DOI: [10.1007/978-3-0348-8689-5_14](https://doi.org/10.1007/978-3-0348-8689-5_14).
- [16] Gregory P Bewley, Ewe-Wei Saw, and Eberhard Bodenschatz. "Observation of the sling effect." In: *New Journal of Physics* 15.8 (Aug. 2013), p. 083051. DOI: [10.1088/1367-2630/15/8/083051](https://doi.org/10.1088/1367-2630/15/8/083051). URL: <https://doi.org/10.1088%2F1367-2630%2F15%2F8%2F083051>.
- [17] Akshay Bhatnagar, Anupam Gupta, Dhrubaditya Mitra, and Rahul Pandit. "Heavy inertial particles in turbulent flows gain energy slowly but lose it rapidly." In: *Phys. Rev. E* 97 (3 2018), p. 033102. DOI: [10.1103/PhysRevE.97.033102](https://doi.org/10.1103/PhysRevE.97.033102). URL: <https://link.aps.org/doi/10.1103/PhysRevE.97.033102>.
- [18] Akshay Bhatnagar, Anupam Gupta, Dhrubaditya Mitra, Rahul Pandit, and Prasad Perlekar. "How long do particles spend in vortical regions in turbulent flows?" In: *Phys. Rev. E* 94 (5 2016), p. 053119. DOI: [10.1103/PhysRevE.94.053119](https://doi.org/10.1103/PhysRevE.94.053119). URL: <https://link.aps.org/doi/10.1103/PhysRevE.94.053119>.
- [19] L. Biferale, G. Boffetta, A. Celani, B. J. Devenish, A. Lanotte, and F. Toschi. "Lagrangian statistics of particle pairs in homogeneous isotropic turbulence." In: *Physics of Fluids* 17.11 (2005), p. 115101. DOI: [10.1063/1.2130742](https://doi.org/10.1063/1.2130742). eprint: <https://doi.org/10.1063/1.2130742>. URL: <https://doi.org/10.1063/1.2130742>.

- [20] L. Biferale, F. Bonaccorso, I. M. Mazzitelli, M. A. T. van Hinsberg, A. S. Lanotte, S. Musacchio, P. Perlekar, and F. Toschi. “Coherent Structures and Extreme Events in Rotating Multi-phase Turbulent Flows.” In: *Phys. Rev. X* 6 (4 2016), p. 041036. DOI: [10.1103/PhysRevX.6.041036](https://doi.org/10.1103/PhysRevX.6.041036). URL: <https://link.aps.org/doi/10.1103/PhysRevX.6.041036>.
- [21] Luca Biferale, Andrea Scagliarini, and Federico Toschi. “On the measurement of vortex filament lifetime statistics in turbulence.” In: *Physics of Fluids* 22.6 (2010), p. 065101. DOI: [10.1063/1.3431660](https://doi.org/10.1063/1.3431660). eprint: <https://doi.org/10.1063/1.3431660>. URL: <https://doi.org/10.1063/1.3431660>.
- [22] R. B. Bird. In: *AICHE Journal* 10.6 (1964), pp. 794–794.
- [23] E. Bodenschatz, S. P. Malinowski, R. A. Shaw, and F. Stratmann. “Can We Understand Clouds Without Turbulence?” In: *Science* 327.5968 (2010), pp. 970–971. ISSN: 0036-8075. DOI: [10.1126/science.1185138](https://doi.org/10.1126/science.1185138). eprint: <http://science.sciencemag.org/content/327/5968/970.full.pdf>. URL: <http://science.sciencemag.org/content/327/5968/970>.
- [24] Craig F. Bohren and Donald R. Huffman. “Absorption and Scattering of Light by Small Particles.” In: (1998). DOI: [10.1002/9783527618156](https://doi.org/10.1002/9783527618156).
- [25] O. Boucher et al. “Climate Change 2013: The Physical Science Basis. Contribution of Working Group I to the Fifth Assessment Report of the Intergovernmental Panel on Climate Change.” In: Cambridge, United Kingdom and New York, NY, USA, 2013, p. 1535.
- [26] Mickaël Bourgoin and Haitao Xu. “Focus on dynamics of particles in turbulence.” In: *New Journal of Physics* 16.8 (2014), p. 085010. DOI: [10.1088/1367-2630/16/8/085010](https://doi.org/10.1088/1367-2630/16/8/085010). URL: <https://doi.org/10.1088%2F1367-2630%2F16%2F8%2F085010>.
- [27] Andrew D Bragg and Lance R Collins. “New insights from comparing statistical theories for inertial particles in turbulence: II. Relative velocities.” In: *New Journal of Physics* 16.5 (2014), p. 055014. DOI: [10.1088/1367-2630/16/5/055014](https://doi.org/10.1088/1367-2630/16/5/055014). URL: <https://doi.org/10.1088%2F1367-2630%2F16%2F5%2F055014>.
- [28] Andrew D. Bragg, Peter J. Ireland, and Lance R. Collins. “Mechanisms for the clustering of inertial particles in the inertial range of isotropic turbulence.” In: *Phys. Rev. E* 92 (2 2015), p. 023029. DOI: [10.1103/PhysRevE.92.023029](https://doi.org/10.1103/PhysRevE.92.023029). URL: <https://link.aps.org/doi/10.1103/PhysRevE.92.023029>.
- [29] Andrew D. Bragg, Peter J. Ireland, and Lance R. Collins. “On the relationship between the non-local clustering mechanism and preferential concentration.” In: *Journal of Fluid Mechanics* 780 (2015), pp. 327–343. DOI: [10.1017/jfm.2015.474](https://doi.org/10.1017/jfm.2015.474).

- [30] Jean-Louis Brenguier and Laure Chaumat. "Droplet Spectra Broadening in Cumulus Clouds. Part I: Broadening in Adiabatic Cores." In: *Journal of the Atmospheric Sciences* 58.6 (2001), pp. 628–641. DOI: [10.1175/1520-0469\(2001\)058<0628:DSBICC>2.0.CO;2](https://doi.org/10.1175/1520-0469(2001)058<0628:DSBICC>2.0.CO;2). eprint: [https://doi.org/10.1175/1520-0469\(2001\)058<0628:DSBICC>2.0.CO;2](https://doi.org/10.1175/1520-0469(2001)058<0628:DSBICC>2.0.CO;2). URL: [https://doi.org/10.1175/1520-0469\(2001\)058<0628:DSBICC>2.0.CO](https://doi.org/10.1175/1520-0469(2001)058<0628:DSBICC>2.0.CO).
- [31] J.M. Burgers. "A Mathematical Model Illustrating the Theory of Turbulence." In: ed. by Richard Von Mises and Theodore Von Kármán. Vol. 1. Advances in Applied Mechanics. Elsevier, 1948, pp. 171–199. DOI: [10.1016/S0065-2156\(08\)70100-5](https://doi.org/10.1016/S0065-2156(08)70100-5). URL: <http://www.sciencedirect.com/science/article/pii/S0065215608701005>.
- [32] M. CENCINI, J. BEC, L. BIFERALE, G. BOFFETTA, A. CELANI, A. S. LANOTTE, S. MUSACCHIO, and F. TOSCHI. "Dynamics and statistics of heavy particles in turbulent flows." In: *Journal of Turbulence* 7 (2006), N36. DOI: [10.1080/14685240600675727](https://doi.org/10.1080/14685240600675727). eprint: <https://doi.org/10.1080/14685240600675727>. URL: <https://doi.org/10.1080/14685240600675727>.
- [33] Enrico Calzavarini, Massimo Cencini, Detlef Lohse, and Federico Toschi. "Quantifying Turbulence-Induced Segregation of Inertial Particles." In: *Phys. Rev. Lett.* 101 (8 2008), p. 084504. DOI: [10.1103/PhysRevLett.101.084504](https://doi.org/10.1103/PhysRevLett.101.084504). URL: <https://link.aps.org/doi/10.1103/PhysRevLett.101.084504>.
- [34] S. Chen, M.-K. Yau, P. Bartello, and L. Xue. "Bridging the condensation–collision size gap: a direct numerical simulation of continuous droplet growth in turbulent clouds." In: *Atmospheric Chemistry and Physics* 18.10 (2018), pp. 7251–7262. DOI: [10.5194/acp-18-7251-2018](https://doi.org/10.5194/acp-18-7251-2018). URL: <https://www.atmos-chem-phys.net/18/7251/2018>.
- [35] P. Y. Chuang, E. W. Saw, J. D. Small, R. A. Shaw, C. M. Sippelley, G. A. Payne, and W. D. Bachalo. "Airborne Phase Doppler Interferometry for Cloud Microphysical Measurements." In: *Aerosol Sci. Tech.* 42.8 (2008), pp. 685–703. DOI: [10.1080/02786820802232956](https://doi.org/10.1080/02786820802232956). eprint: [http://dx.doi.org/10.1080/02786820802232956](https://dx.doi.org/10.1080/02786820802232956).
- [36] S. W. Coleman and J. C. Vassilicos. "A unified sweep-stick mechanism to explain particle clustering in two- and three-dimensional homogeneous, isotropic turbulence." In: *Phys. Fluids* 21.11 (2009), p. 113301. DOI: [10.1063/1.3257638](https://doi.org/10.1063/1.3257638). eprint: <https://doi.org/10.1063/1.3257638>.
- [37] P. Cvitanović, R. Artuso, R. Mainieri, G. Tanner, and G. Vattay. *Chaos: Classical and Quantum*. Copenhagen: Niels Bohr Inst., 2016.

- [38] J. DÁVILA and J. C. R. HUNT. "Settling of small particles near vortices and in turbulence." In: *Journal of Fluid Mechanics* 440 (2001), pp. 117–145. DOI: [10.1017/S0022112001004694](https://doi.org/10.1017/S0022112001004694).
- [39] P. A. Davidson. "Turbulence: An introduction for scientists and engineers." In: (2004).
- [40] P. Deepu, S. Ravichandran, and Rama Govindarajan. "Caustics-induced coalescence of small droplets near a vortex." In: *Phys. Rev. Fluids* 2 (2 2017), p. 024305. DOI: [10.1103/PhysRevFluids.2.024305](https://doi.org/10.1103/PhysRevFluids.2.024305). URL: <https://link.aps.org/doi/10.1103/PhysRevFluids.2.024305>.
- [41] A. Dejoan and R. Monchaux. "Preferential concentration and settling of heavy particles in homogeneous turbulence." In: *Physics of Fluids* 25.1 (2013), p. 013301. DOI: [10.1063/1.4774339](https://doi.org/10.1063/1.4774339). eprint: <https://doi.org/10.1063/1.4774339>. URL: <https://doi.org/10.1063/1.4774339>.
- [42] B. Devenish et al. "Droplet growth in warm turbulent clouds." In: *Q. J. Royal Meteorol. Soc.* 138 (2012), pp. 1401–1429. DOI: [10.1002/qj.1897](https://doi.org/10.1002/qj.1897).
- [43] Rohit Dhariwal and Andrew D. Bragg. "Fluid particles only separate exponentially in the dissipation range of turbulence after extremely long times." In: *Phys. Rev. Fluids* 3 (3 2018), p. 034604. DOI: [10.1103/PhysRevFluids.3.034604](https://doi.org/10.1103/PhysRevFluids.3.034604). URL: <https://link.aps.org/doi/10.1103/PhysRevFluids.3.034604>.
- [44] Zhongwang Dou, Peter J. Ireland, Andrew D. Bragg, Zach Liang, Lance R. Collins, and Hui Hui Meng. "Particle-pair relative velocity measurement in high-Reynolds-number homogeneous and isotropic turbulence using 4-frame particle tracking velocimetry." In: *Experiments in Fluids* 59 (2018), pp. 1–17.
- [45] Falkovich G., Fouxon A., and Stepanov M. G. "Acceleration of rain initiation by cloud turbulence." In: *Nature* 419.6903 (2002), pp. 151–154. ISSN: 1476-4687. DOI: [10.1038/nature00983](https://doi.org/10.1038/nature00983).
- [46] G. Falkovich, A. Fouxon, and M. Stepanov. "Statistics of Turbulence-Induced Fluctuations of Particle Concentration." In: *Sedimentation and Sediment Transport*. Ed. by A. Gyr and W. Kinzelbach. Dordrecht: Springer Netherlands, 2003, pp. 155–158. ISBN: 978-94-017-0347-5.
- [47] Gregory Falkovich and Alain Pumir. "Sling Effect in Collisions of Water Droplets in Turbulent Clouds." In: *J. Atmos. Sci.* 64.12 (2007), pp. 4497–4505. DOI: [10.1175/2007JAS2371.1](https://doi.org/10.1175/2007JAS2371.1).
- [48] S. Gienke, A. Kostinski, J. Fugal, R. A. Shaw, S. Borrmann, and J. Stith. "Cloud droplets to drizzle: Contribution of transition drops to microphysical and optical properties of marine stratuscumulus clouds." In: *Geophysical Research Letters* 44.15 (2017), pp. 8002–8010. DOI: [10.1002/2017GL074430](https://doi.org/10.1002/2017GL074430). eprint: <https://doi.org/10.1002/2017GL074430>.

- //agupubs.onlinelibrary.wiley.com/doi/pdf/10.1002/2017GL074430. URL: <https://agupubs.onlinelibrary.wiley.com/doi/abs/10.1002/2017GL074430>.
- [49] Susumu Goto and J. C. Vassilicos. “Sweep-Stick Mechanism of Heavy Particle Clustering in Fluid Turbulence.” In: *Phys. Rev. Lett.* 100 (5 2008), p. 054503. DOI: [10.1103/PhysRevLett.100.054503](https://doi.org/10.1103/PhysRevLett.100.054503). URL: <https://link.aps.org/doi/10.1103/PhysRevLett.100.054503>.
- [50] Toshiyuki Gotoh, Daigen Fukayama, and Tohru Nakano. “Velocity field statistics in homogeneous steady turbulence obtained using a high-resolution direct numerical simulation.” In: *Physics of Fluids* 14.3 (2002), pp. 1065–1081. DOI: [10.1063/1.1448296](https://doi.org/10.1063/1.1448296). URL: <https://doi.org/10.1063/1.1448296>.
- [51] Wojciech W. Grabowski and Lian-Ping Wang. “Growth of Cloud Droplets in a Turbulent Environment.” In: *Ann. Rev. Fluid Mech.* 45.1 (2013), pp. 293–324. DOI: [10.1146/annurev-fluid-011212-140750](https://doi.org/10.1146/annurev-fluid-011212-140750). eprint: <https://doi.org/10.1146/annurev-fluid-011212-140750>.
- [52] K. Gustavsson and B. Mehlig. “Statistical models for spatial patterns of heavy particles in turbulence.” In: *Adv. Phys.* 65.1 (2016), pp. 1–57. DOI: [10.1080/00018732.2016.1164490](https://doi.org/10.1080/00018732.2016.1164490).
- [53] K. Gustavsson, S. Vajedi, and B. Mehlig. “Clustering of Particles Falling in a Turbulent Flow.” In: *Phys. Rev. Lett.* 112 (21 2014), p. 214501. DOI: [10.1103/PhysRevLett.112.214501](https://doi.org/10.1103/PhysRevLett.112.214501). URL: <https://link.aps.org/doi/10.1103/PhysRevLett.112.214501>.
- [54] Thomas Hartlep, Jeffrey N. Cuzzi, and Brian Weston. “Scale dependence of multiplier distributions for particle concentration, enstrophy, and dissipation in the inertial range of homogeneous turbulence.” In: *Phys. Rev. E* 95 (3 2017), p. 033115. DOI: [10.1103/PhysRevE.95.033115](https://doi.org/10.1103/PhysRevE.95.033115). URL: <https://link.aps.org/doi/10.1103/PhysRevE.95.033115>.
- [55] Reginald Janusz Hill. “Geometric collision rates and trajectories of cloud droplets falling into a Burgers vortex.” In: *Phys. Fluids* 17 (2005), p. 037103. DOI: [10.1063/1.1858191](https://doi.org/10.1063/1.1858191).
- [56] Peter J. Ireland, Andrew D. Bragg, and Lance R. Collins. “The effect of Reynolds number on inertial particle dynamics in isotropic turbulence. Part 1. Simulations without gravitational effects.” In: *Journal of Fluid Mechanics* 796 (2016), pp. 617–658. DOI: [10.1017/jfm.2016.238](https://doi.org/10.1017/jfm.2016.238).
- [57] Peter J. Ireland, Andrew D. Bragg, and Lance R. Collins. “The effect of Reynolds number on inertial particle dynamics in isotropic turbulence. Part 2. Simulations with gravitational ef-

- fects." In: *Journal of Fluid Mechanics* 796 (2016), pp. 659–711. DOI: [10.1017/jfm.2016.227](https://doi.org/10.1017/jfm.2016.227).
- [58] A. Jaczewski and S. P. Malinowski. "Spatial distribution of cloud droplets in a turbulent cloud-chamber flow." In: *Quarterly Journal of the Royal Meteorological Society* 131.609 (2005), pp. 2047–2062. DOI: [10.1256/qj.04.65](https://doi.org/10.1256/qj.04.65). eprint: <https://rmets.onlinelibrary.wiley.com/doi/pdf/10.1256/qj.04.65>. URL: <https://rmets.onlinelibrary.wiley.com/doi/abs/10.1256/qj.04.65>.
- [59] I. Jen-La Plante, Y. Ma, K. Nurowska, H. Gerber, D. Khelif, K. Karpinska, M. K. Kopec, W. Kumala, and S. P. Malinowski. "Physics of Stratocumulus Top (POST): turbulence characteristics." In: *Atmospheric Chemistry and Physics* 16.15 (2016), pp. 9711–9725.
- [60] J. Jimenez and A. Wray. "On the characteristics of vortex filaments in isotropic turbulence." In: *J. Fluid Mech.* 373 (1998), pp. 255–285. DOI: [10.1017/S0022112098002341](https://doi.org/10.1017/S0022112098002341).
- [61] A. B. KOSTINSKI and R. A. SHAW. "Scale-dependent droplet clustering in turbulent clouds." In: *Journal of Fluid Mechanics* 434 (2001), pp. 389–398. DOI: [10.1017/S0022112001004001](https://doi.org/10.1017/S0022112001004001).
- [62] K. Karpińska et al. "Turbulence-induced cloud voids: observation and interpretation." In: *Atmospheric Chemistry and Physics* 19.7 (2019), pp. 4991–5003. DOI: [10.5194/acp-19-4991-2019](https://doi.org/10.5194/acp-19-4991-2019). URL: <https://www.atmos-chem-phys.net/19/4991/2019>.
- [63] Y. Knyazikhin, R. B. Myneni, A. Marshak, W. J. Wiscombe, M. L. Larsen, and J. V. Martonchik. "Small-Scale Drop Size Variability: Impact on Estimation of Cloud Optical Properties." In: *Journal of the Atmospheric Sciences* 62.7 (2005), pp. 2555–2567. DOI: [10.1175/JAS3488.1](https://doi.org/10.1175/JAS3488.1). eprint: <https://doi.org/10.1175/JAS3488.1>. URL: <https://doi.org/10.1175/JAS3488.1>.
- [64] A. N. Kolmogorov. "Energy dissipation in locally isotropic turbulence." In: *Doklady AN SSSR*. Vol. 32. 1. 1941, pp. 19–21.
- [65] Alexander B. Kostinski and Raymond A. Shaw. "Fluctuations and Luck in Droplet Growth by Coalescence." In: *Bulletin of the American Meteorological Society* 86.2 (2005), pp. 235–244. DOI: [10.1175/BAMS-86-2-235](https://doi.org/10.1175/BAMS-86-2-235). eprint: <https://doi.org/10.1175/BAMS-86-2-235>. URL: <https://doi.org/10.1175/BAMS-86-2-235>.
- [66] Y. Kuznetsov. 3rd ed. Vol. 112. Applied Mathematical Sciences. Springer-Verlag New York, 2004. ISBN: 978-1-4757-3978-7.

- [67] KATRIN LEHMANN, HOLGER SIEBERT, MANFRED WENDISCH, and RAYMOND A. SHAW. "Evidence for inertial droplet clustering in weakly turbulent clouds." In: *Tellus B* 59.1 (2007), pp. 57–65. DOI: [10.1111/j.1600-0889.2006.00230.x](https://doi.org/10.1111/j.1600-0889.2006.00230.x). eprint: <https://onlinelibrary.wiley.com/doi/pdf/10.1111/j.1600-0889.2006.00230.x>. URL: <https://onlinelibrary.wiley.com/doi/abs/10.1111/j.1600-0889.2006.00230.x>.
- [68] Michael L. Larsen, Raymond A. Shaw, Alexander B. Kostinski, and Susanne Glienke. "Fine-Scale Droplet Clustering in Atmospheric Clouds: 3D Radial Distribution Function from Airborne Digital Holography." In: *Phys. Rev. Lett.* 121 (20 2018), p. 204501. DOI: [10.1103/PhysRevLett.121.204501](https://doi.org/10.1103/PhysRevLett.121.204501). URL: <https://link.aps.org/doi/10.1103/PhysRevLett.121.204501>.
- [69] H. Lian, X. Y. Chang, and Y. Hardalupas. "Time resolved measurements of droplet preferential concentration in homogeneous isotropic turbulence without mean flow." In: *Physics of Fluids* 31.2 (2019), p. 025103. DOI: [10.1063/1.5063673](https://doi.org/10.1063/1.5063673). eprint: <https://doi.org/10.1063/1.5063673>. URL: <https://doi.org/10.1063/1.5063673>.
- [70] Huan Lian, Georgios Charalampous, and Yannis Hardalupas. "Preferential concentration of poly-dispersed droplets in stationary isotropic turbulence." In: *Experiments in Fluids* 54.5 (2013), p. 1525. ISSN: 1432-1114. DOI: [10.1007/s00348-013-1525-3](https://doi.org/10.1007/s00348-013-1525-3). URL: <https://doi.org/10.1007/s00348-013-1525-3>.
- [71] Manish M and Srikrishna Sahu. "Analysis of droplet clustering in air-assist sprays using Voronoi tessellations." In: *Physics of Fluids* 30.12 (2018), p. 123305. DOI: [10.1063/1.5053473](https://doi.org/10.1063/1.5053473). eprint: <https://doi.org/10.1063/1.5053473>. URL: <https://doi.org/10.1063/1.5053473>.
- [72] Yong-Feng Ma, Szymon P. Malinowski, Katarzyna Karpińska, Hermann E. Gerber, and Wojciech Kumala. "Scaling Analysis of Temperature and Liquid Water Content in the Marine Boundary Layer Clouds during POST." In: *Journal of the Atmospheric Sciences* 74.12 (2017), pp. 4075–4092.
- [73] B. Marcu, E. Meiburg, and P. K. Newton. "Dynamics of heavy particles in a burgers vortex." In: *Phys. Fluids* 7 (1995), pp. 400–410. DOI: [10.1063/1.868778](https://doi.org/10.1063/1.868778).
- [74] Krzysztof Markowicz, Konrad Bajer, and Szymon P. Malinowski. "Influence of small-scale turbulence structures on the concentration of cloud droplets." In: *13th Conference on Clouds and Precipitation*. Vol. 1. ICCP-IAMAS. Reno, Nevada, 2000, pp. 159–162.

- [75] Alexander Marshak, Yuri Knyazikhin, Michael L. Larsen, and Warren J. Wiscombe. "Small-Scale Drop-Size Variability: Empirical Models for Drop-Size-Dependent Clustering in Clouds." In: *Journal of the Atmospheric Sciences* 62.2 (2005), pp. 551–558. DOI: [10.1175/JAS-3371.1](https://doi.org/10.1175/JAS-3371.1). eprint: <https://doi.org/10.1175/JAS-3371.1>. URL: <https://doi.org/10.1175/JAS-3371.1>.
- [76] M. R. Maxey. "The gravitational settling of aerosol particles in homogeneous turbulence and random flow fields." In: *J. Fluid Mech.* 174 (1987), pp. 441–465. DOI: [10.1017/S0022112087000193](https://doi.org/10.1017/S0022112087000193).
- [77] Martin R. Maxey and James J. Riley. "Equation of motion for a small rigid sphere in a nonuniform flow." In: *The Physics of Fluids* 26.4 (1983), pp. 883–889.
- [78] Jean-Pierre Minier. "Statistical descriptions of polydisperse turbulent two-phase flows." In: *Physics Reports* 665 (2016). Statistical descriptions of polydisperse turbulent two-phase flows, pp. 1–122. ISSN: 0370-1573. DOI: [10.1016/j.physrep.2016.10.007](https://doi.org/10.1016/j.physrep.2016.10.007). URL: <http://www.sciencedirect.com/science/article/pii/S0370157316303350>.
- [79] F. Moisy and J. Jimenez. "Geometry and clustering of intense structures in isotropic turbulence." In: *J. Fluid Mech.* 513 (2004), pp. 111–133. DOI: [10.1017/S0022112004009802](https://doi.org/10.1017/S0022112004009802).
- [80] Mohammadreza Momenifar and Andrew D. Bragg. "Local analysis of the clustering, velocities and accelerations of particles settling in turbulence." In: *arXiv e-prints*, arXiv:1908.00341 (2019), arXiv:1908.00341. arXiv: [1908.00341 \[physics.flu-dyn\]](https://arxiv.org/abs/1908.00341).
- [81] R. Monchaux, M. Bourgoin, and A. Cartellier. "Preferential concentration of heavy particles: A Voronoï analysis." In: *Physics of Fluids* 22.10 (2010), p. 103304. DOI: [10.1063/1.3489987](https://doi.org/10.1063/1.3489987). eprint: <https://doi.org/10.1063/1.3489987>. URL: <https://doi.org/10.1063/1.3489987>.
- [82] R. Monchaux and A. Dejoan. "Settling velocity and preferential concentration of heavy particles under two-way coupling effects in homogeneous turbulence." In: *Phys. Rev. Fluids* 2 (10 2017), p. 104302. DOI: [10.1103/PhysRevFluids.2.104302](https://doi.org/10.1103/PhysRevFluids.2.104302). URL: <https://link.aps.org/doi/10.1103/PhysRevFluids.2.104302>.
- [83] Romain Monchaux, Mickael Bourgoin, and Alain Cartellier. "Analyzing preferential concentration and clustering of inertial particles in turbulence." In: *International Journal of Multiphase Flow* 40 (2012), pp. 1–18. ISSN: 0301-9322. DOI: [10.1016/j.ijmultiphaseflow.2011.12.001](https://doi.org/10.1016/j.ijmultiphaseflow.2011.12.001). URL: <http://www.sciencedirect.com/science/article/pii/S030193221100245X>.

- [84] H. Mouri, A. Hori, and Y. Kawashima. "Vortex tubes in velocity fields of laboratory isotropic turbulence." In: *Phys. Lett. A* 276 (2003), pp. 115–121. DOI: [10.1103/PhysRevE.67.016305](https://doi.org/10.1103/PhysRevE.67.016305).
- [85] "Multiscale analysis of the invariants of the velocity gradient tensor in isotropic turbulence." In: (2018).
- [86] John C. Neu. "The dynamics of stretched vortices." In: *J. Fluid Mech.* 143 (June 1984), pp. 253–276. DOI: [10.1017/S0022112084001348](https://doi.org/10.1017/S0022112084001348). URL: <https://www.cambridge.org/core/article/dynamics-of-stretched-vortices/1783CBAF5D397FD30CD90BB137533477>.
- [87] Martín Obligado, Tomás Teitelbaum, Alain Cartellier, Pablo Mininni, and Mickaël Bourgoin. "Preferential concentration of heavy particles in turbulence." In: *Journal of Turbulence* 15.5 (2014), pp. 293–310. DOI: [10.1080/14685248.2014.897710](https://doi.org/10.1080/14685248.2014.897710). eprint: <https://doi.org/10.1080/14685248.2014.897710>. URL: <https://doi.org/10.1080/14685248.2014.897710>.
- [88] S. Olivieri, F. Picano, G. Sardina, D. Iudicone, and L. Brandt. "The effect of the Basset history force on particle clustering in homogeneous and isotropic turbulence." In: *Physics of Fluids* 26.4 (2014), p. 041704. DOI: [10.1063/1.4871480](https://doi.org/10.1063/1.4871480). eprint: <https://doi.org/10.1063/1.4871480>. URL: <https://doi.org/10.1063/1.4871480>.
- [89] M. G. Olsen and R. J. Adrian. "Out-of-focus effects on particle image visibility and correlation in microscopic particle image velocimetry." In: *Exp. Fluids* 29.1 (2000), S166–S174. ISSN: 1432-1114. DOI: [10.1007/s003480070018](https://doi.org/10.1007/s003480070018).
- [90] Isidoro Orlanski. "A Rational Subdivision of Scales for Atmospheric Processes." In: *Bulletin of the American Meteorological Society* 56.5 (1975), pp. 527–530. ISSN: 00030007, 15200477. URL: <http://www.jstor.org/stable/26216020>.
- [91] Vincent E. Perrin and Harmen J. J. Jonker. "Effect of the eigenvalues of the velocity gradient tensor on particle collisions." In: *Journal of Fluid Mechanics* 792 (2016), pp. 36–49. DOI: [10.1017/jfm.2016.70](https://doi.org/10.1017/jfm.2016.70).
- [92] A E Perry and M S Chong. "A Description of Eddying Motions and Flow Patterns Using Critical-Point Concepts." In: *Annual Review of Fluid Mechanics* 19.1 (1987), pp. 125–155. DOI: [10.1146/annurev.fl.19.010187.001013](https://doi.org/10.1146/annurev.fl.19.010187.001013). eprint: <https://doi.org/10.1146/annurev.fl.19.010187.001013>. URL: <https://doi.org/10.1146/annurev.fl.19.010187.001013>.
- [93] Jason R. Picardo, Lokahith Agasthya, Rama Govindarajan, and Samriddhi Sankar Ray. "Flow structures govern particle collisions in turbulence." In: *Phys. Rev. Fluids* 4 (3 2019), p. 032601. DOI: [10.1103/PhysRevFluids.4.032601](https://doi.org/10.1103/PhysRevFluids.4.032601). URL: <https://link.aps.org/doi/10.1103/PhysRevFluids.4.032601>.

- [94] M. Pinsky and A. P. Khain. "Fine Structure of Cloud Droplet Concentration as Seen from the Fast-FSSP Measurements. Part I: Method of Analysis and Preliminary Results." In: *Journal of Applied Meteorology* 40.8 (2001), pp. 1515–1537. DOI: [10.1175/1520-0450\(2001\)040<1515:FSOCDC>2.0.CO;2](https://doi.org/10.1175/1520-0450(2001)040<1515:FSOCDC>2.0.CO;2). eprint: [https://doi.org/10.1175/1520-0450\(2001\)040<1515:FSOCDC>2.0.CO;2](https://doi.org/10.1175/1520-0450(2001)040<1515:FSOCDC>2.0.CO;2). URL: [https://doi.org/10.1175/1520-0450\(2001\)040<1515:FSOCDC>2.0.CO](https://doi.org/10.1175/1520-0450(2001)040<1515:FSOCDC>2.0.CO).
- [95] S. Pirozzoli. "On the velocity and dissipation signature of vortex tubes in isotropic turbulence." In: *Physica D* 241 (2012), pp. 202–207. DOI: [10.1016/j.physd.2011.03.005](https://doi.org/10.1016/j.physd.2011.03.005).
- [96] Stephen B Pope. *Turbulent flows*. Cambridge: Cambridge Univ. Press, 2011.
- [97] Alain Pumir and Michael Wilkinson. "Collisional Aggregation Due to Turbulence." In: *Annual Review of Condensed Matter Physics* 7.1 (2016), pp. 141–170. DOI: [10.1146/annurev-conmatphys-031115-011538](https://doi.org/10.1146/annurev-conmatphys-031115-011538). eprint: <https://doi.org/10.1146/annurev-conmatphys-031115-011538>. URL: <https://doi.org/10.1146/annurev-conmatphys-031115-011538>.
- [98] S. Ravichandran and Rama Govindarajan. "Caustics and clustering in the vicinity of a vortex." In: *Phys. Fluids* 27.3 (2015), p. 033305. DOI: [10.1063/1.4916583](https://doi.org/10.1063/1.4916583). eprint: <https://doi.org/10.1063/1.4916583>.
- [99] S. Ravichandran, Prasad Perlekar, and Rama Govindarajan. "Attracting fixed points for heavy particles in the vicinity of a vortex pair." In: *Phys. Fluids* 26.1 (2014), p. 013303. DOI: [10.1063/1.4861395](https://doi.org/10.1063/1.4861395). eprint: <https://doi.org/10.1063/1.4861395>.
- [100] Osborne Reynolds. "XXIX. An experimental investigation of the circumstances which determine whether the motion of water shall be direct or sinuous, and of the law of resistance in parallel channels." In: *Philosophical Transactions of the Royal Society of London* 174 (1883), pp. 935–982. DOI: [10.1098/rstl.1883.0029](https://doi.org/10.1098/rstl.1883.0029). URL: <https://royalsocietypublishing.org/doi/abs/10.1098/rstl.1883.0029>.
- [101] Lewis F. Richardson. *Weather prediction by numerical process*. Cambridge University Press, 1922. URL: <https://archive.org/details/weatherpredictio00richrich>.
- [102] S. Risius, H. Xu, F. Di Lorenzo, H. Xi, H. Siebert, R. A. Shaw, and E. Bodenschatz. "Schneefernerhaus as a mountain research station for clouds and turbulence." In: *Atmos. Meas. Tech.* 8.8 (2015), pp. 3209–3218. DOI: [10.5194/amt-8-3209-2015](https://doi.org/10.5194/amt-8-3209-2015). URL: <http://www.atmos-meas-tech.net/8/3209/2015>.

- [103] Bogdan Rosa and Jacek Pozorski. "Impact of subgrid fluid turbulence on inertial particles subject to gravity." In: *Journal of Turbulence* 18.7 (2017), pp. 634–652. DOI: [10.1080/14685248.2017.1317099](https://doi.org/10.1080/14685248.2017.1317099). eprint: <https://doi.org/10.1080/14685248.2017.1317099>. URL: <https://doi.org/10.1080/14685248.2017.1317099>.
- [104] Mahdi Saeedipour, Simon Schneiderbauer, Stefan Pirker, and Salar Bozorgi. "Numerical simulation of turbulent liquid jet breakup using a sub-grid criterion with industrial application." In: Sept. 2014.
- [105] Izumi Saito and Toshiyuki Gotoh. "Turbulence and cloud droplets in cumulus clouds." In: *New Journal of Physics* 20.2 (2018), p. 023001. DOI: [10.1088/1367-2630/aaa229](https://doi.org/10.1088/1367-2630/aaa229). URL: <https://doi.org/10.1088%2F1367-2630%2Faaa229>.
- [106] Ewe-Wei Saw, Gregory P. Bewley, Eberhard Bodenschatz, Samriddhi Sankar Ray, and Jérémie Bec. "Extreme fluctuations of the relative velocities between droplets in turbulent airflow." In: *Physics of Fluids* 26.11 (2014), p. 111702. DOI: [10.1063/1.4900848](https://doi.org/10.1063/1.4900848). eprint: <https://doi.org/10.1063/1.4900848>. URL: <https://doi.org/10.1063/1.4900848>.
- [107] Ewe-Wei Saw, Juan P L C Salazar, Lance R Collins, and Raymond A Shaw. "Spatial clustering of polydisperse inertial particles in turbulence: I. Comparing simulation with theory." In: *New Journal of Physics* 14.10 (2012), p. 105030. DOI: [10.1088/1367-2630/14/10/105030](https://doi.org/10.1088/1367-2630/14/10/105030). URL: <https://doi.org/10.1088%2F1367-2630%2F14%2F10%2F105030>.
- [108] Ewe Wei Saw, Raymond A. Shaw, Sathyanarayana Ayyalaso-mayajula, Patrick Y. Chuang, and Ármann Gylfason. "Inertial Clustering of Particles in High-Reynolds-Number Turbulence." In: *Phys. Rev. Lett.* 100 (21 2008), p. 214501. DOI: [10.1103/PhysRevLett.100.214501](https://doi.org/10.1103/PhysRevLett.100.214501). URL: <https://link.aps.org/doi/10.1103/PhysRevLett.100.214501>.
- [109] Ewe-Wei Saw, Raymond A Shaw, Juan P L C Salazar, and Lance R Collins. "Spatial clustering of polydisperse inertial particles in turbulence: II. Comparing simulation with experiment." In: *New Journal of Physics* 14.10 (2012), p. 105031. DOI: [10.1088/1367-2630/14/10/105031](https://doi.org/10.1088/1367-2630/14/10/105031). URL: <https://doi.org/10.1088%2F1367-2630%2F14%2F10%2F105031>.
- [110] R. Scatamacchia, L. Biferale, and F. Toschi. "Extreme Events in the Dispersions of Two Neighboring Particles Under the Influence of Fluid Turbulence." In: *Phys. Rev. Lett.* 109 (14 2012), p. 144501. DOI: [10.1103/PhysRevLett.109.144501](https://doi.org/10.1103/PhysRevLett.109.144501). URL: <https://link.aps.org/doi/10.1103/PhysRevLett.109.144501>.

- [111] R. A. Shaw, A. B. Kostinski, and M. L. Larsen. "Towards quantifying droplet clustering in clouds." In: *Quarterly Journal of the Royal Meteorological Society* 128.582 (2002), pp. 1043–1057. DOI: [10.1256/003590002320373193](https://doi.org/10.1256/003590002320373193). eprint: <https://rmets.onlinelibrary.wiley.com/doi/pdf/10.1256/003590002320373193>. URL: <https://rmets.onlinelibrary.wiley.com/doi/abs/10.1256/003590002320373193>.
- [112] Raymond A. Shaw. "Particle-turbulence interactions in atmospheric clouds." In: *Annual Review of Fluid Mechanics* 35.1 (2003), pp. 183–227. DOI: [10.1146/annurev.fluid.35.101101.161125](https://doi.org/10.1146/annurev.fluid.35.101101.161125). eprint: <https://doi.org/10.1146/annurev.fluid.35.101101.161125>. URL: <https://doi.org/10.1146/annurev.fluid.35.101101.161125>.
- [113] H. Siebert, R. A. Shaw, J. Ditas, T. Schmeissner, S. P. Malinowski, E. Bodenschatz, and H. Xu. "High-resolution measurement of cloud microphysics and turbulence at a mountaintop station." In: *Atmos. Meas. Tech.* 8.8 (2015), pp. 3219–3228. DOI: [10.5194/amt-8-3219-2015](https://doi.org/10.5194/amt-8-3219-2015). URL: <http://www.atmos-meas-tech.net/8/3219/2015>.
- [114] H. Siebert, R. A. Shaw, and Z. Warhaft. "Statistics of Small-Scale Velocity Fluctuations and Internal Intermittency in Marine Stratocumulus Clouds." In: *Journal of the Atmospheric Sciences* 67.1 (2010), pp. 262–273. DOI: [10.1175/2009JAS3200.1](https://doi.org/10.1175/2009JAS3200.1). URL: <https://doi.org/10.1175/2009JAS3200.1>.
- [115] H. Siebert et al. "The fine-scale structure of the trade wind cumuli over Barbados – an introduction to the CARRIBA project." In: *Atmospheric Chemistry and Physics* 13.19 (2013), pp. 10061–10077.
- [116] H. Sigurgeirsson and A. M. Stuart. "A model for preferential concentration." In: *Physics of Fluids* 14.12 (2002), pp. 4352–4361. DOI: [10.1063/1.1517603](https://doi.org/10.1063/1.1517603). eprint: <https://doi.org/10.1063/1.1517603>. URL: <https://doi.org/10.1063/1.1517603>.
- [117] Sholpan Sumbekova, Alain Cartellier, Alberto Aliseda, and Mickael Bourgoin. "Preferential concentration of inertial sub-Kolmogorov particles: The roles of mass loading of particles, Stokes numbers, and Reynolds numbers." In: *Phys. Rev. Fluids* 2 (2017), p. 024302. DOI: [10.1103/PhysRevFluids.2.024302](https://doi.org/10.1103/PhysRevFluids.2.024302). URL: <https://link.aps.org/doi/10.1103/PhysRevFluids.2.024302>.
- [118] Keiko Takahashi, Koji Goto, Ryo Onishi, and Masatoshi Imada. "Large-scale intermittency and rare events boosted at dimensional crossover in anisotropic turbulence." In: *Phys. Rev. Fluids* 3 (2018), p. 124607.

- [119] Josin Tom and Andrew D. Bragg. "Multiscale preferential sweeping of particles settling in turbulence." In: *Journal of Fluid Mechanics* 871 (2019), pp. 244–270. DOI: [10.1017/jfm.2019.337](https://doi.org/10.1017/jfm.2019.337).
- [120] Federico Toschi and Eberhard Bodenschatz. "Lagrangian Properties of Particles in Turbulence." In: *Annual Review of Fluid Mechanics* 41.1 (2009), pp. 375–404. DOI: [10.1146/annurev.fluid.010908.165210](https://doi.org/10.1146/annurev.fluid.010908.165210). eprint: <https://doi.org/10.1146/annurev.fluid.010908.165210>. URL: <https://doi.org/10.1146/annurev.fluid.010908.165210>.
- [121] A. Tsinober. "An Informal Introduction to Turbulence." In: vol. 63. Jan. 2004, p. 332. DOI: [10.1007/0-306-48384-X](https://doi.org/10.1007/0-306-48384-X).
- [122] Arkady Tsinober. "An Informal Conceptual Introduction to Turbulence: Second Edition of An Informal Introduction to Turbulence." In: vol. 92. Jan. 2009. ISBN: 9048131731. DOI: [10.1007/978-90-481-3174-7](https://doi.org/10.1007/978-90-481-3174-7).
- [123] Paul A. Vaillancourt and M. K. Yau. "Review of Particle-Turbulence Interactions and Consequences for Cloud Physics." In: *Bulletin of the American Meteorological Society* 81.2 (2000), pp. 285–298. DOI: [10.1175/1520-0477\(2000\)081<0285:ROPIAC>2.3.C0;2](https://doi.org/10.1175/1520-0477(2000)081<0285:ROPIAC>2.3.C0;2). eprint: [https://doi.org/10.1175/1520-0477\(2000\)081<0285:ROPIAC>2.3.C0;2](https://doi.org/10.1175/1520-0477(2000)081<0285:ROPIAC>2.3.C0;2). URL: [https://doi.org/10.1175/1520-0477\(2000\)081<0285:ROPIAC>2.3.C0](https://doi.org/10.1175/1520-0477(2000)081<0285:ROPIAC>2.3.C0).
- [124] Dimitar G. Vlaykov and Michael Wilczek. "On the small-scale structure of turbulence and its impact on the pressure field." In: *Journal of Fluid Mechanics* 861 (2019), pp. 422–446. DOI: [10.1017/jfm.2018.857](https://doi.org/10.1017/jfm.2018.857).
- [125] M. Wacławczyk, Y.-F. Ma, J. M. Kopeć, and S. P. Malinowski. "Novel approaches to estimating the turbulent kinetic energy dissipation rate from low- and moderate-resolution velocity fluctuation time series." In: *Atmospheric Measurement Techniques* 10.12 (2017), pp. 4573–4585. DOI: [10.5194/amt-10-4573-2017](https://doi.org/10.5194/amt-10-4573-2017). URL: <https://www.atmos-meas-tech.net/10/4573/2017>.
- [126] James M. Wallace. "Twenty years of experimental and direct numerical simulation access to the velocity gradient tensor: What have we learned about turbulence?" In: *Physics of Fluids* 21.2 (2009), p. 021301.
- [127] Lian-Ping Wang, Orlando Ayala, Yan Xue, and Wojciech W. Grabowski. "Comments on ‘‘Droplets to Drops by Turbulent Coagulation’’." In: *Journal of the Atmospheric Sciences* 63.9 (2006), pp. 2397–2401. DOI: [10.1175/JAS3750.1](https://doi.org/10.1175/JAS3750.1). eprint: <https://doi.org/10.1175/JAS3750.1>. URL: <https://doi.org/10.1175/JAS3750.1>.
- [128] Z. Warhaft. In: *Annual Review of Fluid Mechanics* 32.1 (2000), pp. 203–240.

- [129] Z. Warhaft. "Turbulence in nature and in the laboratory." In: *Proceedings of the National Academy of Sciences* 99.suppl 1 (2002), pp. 2481–2486. ISSN: 0027-8424. DOI: [10.1073/pnas.012580299](https://doi.org/10.1073/pnas.012580299). eprint: https://www.pnas.org/content/99/suppl_1/2481.full.pdf. URL: https://www.pnas.org/content/99/suppl_1/2481.
- [130] Z Warhaft. "Laboratory studies of droplets in turbulence: towards understanding the formation of clouds." In: *Fluid Dynamics Research* 41.1 (2008), p. 011201. DOI: [10.1088/0169-5983/41/1/011201](https://doi.org/10.1088/0169-5983/41/1/011201). URL: <https://doi.org/10.1088%2F0169-5983%2F41%2F1%2F011201>.
- [131] Michael Wilczek. "Statistical and Numerical Investigations of Fluid Turbulence." In: *PhD thesis* (2011).
- [132] Eric J. P. Woittiez, Harm J. J. Jonker, and Luís M. Portela. "On the Combined Effects of Turbulence and Gravity on Droplet Collisions in Clouds: A Numerical Study." In: *Journal of the Atmospheric Sciences* 66.7 (2009), pp. 1926–1943. DOI: [10.1175/2005JAS2669.1](https://doi.org/10.1175/2005JAS2669.1). eprint: <https://doi.org/10.1175/2005JAS2669.1>. URL: <https://doi.org/10.1175/2005JAS2669.1>.
- [133] John C. Wyngaard. *Turbulence in the Atmosphere*. Cambridge University Press, 2010. DOI: [10.1017/CBO9780511840524](https://doi.org/10.1017/CBO9780511840524).
- [134] H. Xu, S. Risius, H. Xi, J. Bodenschatz, S. P. Malinowski, R. A. Shaw, T. Schmeissner, H. Siebert, and E. Bodenschatz. "Turbulence induced "cloud holes" in mountain-top clouds at Schneefern-erhaus research station." In: (2012).
- [135] M. A. Yavuz, R. P. J. Kunnen, G. J. F. van Heijst, and H. J. H. Clercx. "Extreme Small-Scale Clustering of Droplets in Turbulence Driven by Hydrodynamic Interactions." In: *Phys. Rev. Lett.* 120 (24 2018), p. 244504. DOI: [10.1103/PhysRevLett.120.244504](https://doi.org/10.1103/PhysRevLett.120.244504). URL: <https://link.aps.org/doi/10.1103/PhysRevLett.120.244504>.
- [136] Yeung P K, Zhai X M, and Sreenivasan Katepalli R. "Extreme events in computational turbulence." In: *Proceedings of the National Academy of Sciences of the United States of America* 112.41 (2015), pp. 12633–12638. ISSN: 1091-6490 0027-8424. URL: <https://www.ncbi.nlm.nih.gov/pubmed/26424452>.
- [137] P. K. Yeung, D. A. Donzis, and K. R. Sreenivasan. "Dissipation, enstrophy and pressure statistics in turbulence simulations at high Reynolds numbers." In: *Journal of Fluid Mechanics* 700 (2012), pp. 5–15.
- [138] S. Zilitinkevich, O. Druzhinin, A. Glazunov, E. Kadantsev, E. Mortikov, I. Repina, and Y. Troitskaya. "Dissipation rate of turbulent kinetic energy in stably stratified sheared flows." In: *Atmospheric Chemistry and Physics* 19.4 (2019), pp. 2489–2496.

DOI: [10.5194/acp-19-2489-2019](https://doi.org/10.5194/acp-19-2489-2019). URL: <https://www.atmos-chem-phys.net/19/2489/2019>.

DECLARATION

Put your declaration here.

Warszawa, 2018

Katarzyna Karpińska

COLOPHON

This document was typeset using the typographical look-and-feel `classicthesis` developed by André Miede. The style was inspired by Robert Bringhurst's seminal book on typography "*The Elements of Typographic Style*". `classicthesis` is available for both L^AT_EX and LyX:

<https://bitbucket.org/amiede/classicthesis/>

Happy users of `classicthesis` usually send a real postcard to the author, a collection of postcards received so far is featured here:

<http://postcards.miede.de/>